The growth and optical properties of III-V nanostructures grown by Molecular Beam Epitaxy

THÈSE N^{O} 7393 (2017)

PRÉSENTÉE LE 27 JANVIER 2017

À LA FACULTÉ DES SCIENCES ET TECHNIQUES DE L'INGÉNIEUR
LABORATOIRE DES MATÉRIAUX SEMICONDUCTEURS
PROGRAMME DOCTORAL EN SCIENCE ET GÉNIE DES MATÉRIAUX

ÉCOLE POLYTECHNIQUE FÉDÉRALE DE LAUSANNE

POUR L'OBTENTION DU GRADE DE DOCTEUR ÈS SCIENCES

PAR

Gözde TÜTÜNCÜOGLU

acceptée sur proposition du jury:

Prof. P. Muralt, président du jury
Prof. A. Fontcuberta i Morral, directrice de thèse
Prof. C. Carter, rapporteur
Dr P. Plochocka, rapporteuse
Prof. F. Sorin, rapporteur

ÉCOLE POLYTECHNIQUE
FÉDÉRALE DE LAUSANNE

Suisse
2017

To my family…

Acknowledgements

Being in LMSC for more than 5 years has been a unique, enriching and a very warm experience for me. I have started my journey with a semester project during my master studies and ended it up with a Ph.D. degree, which took more than 4 years to complete!

First person that I'd like to express my gratitude for that amazing journey is of course Anna Fontcuberta i Morral. In addition to being a magnificent thesis supervisor and scientist she is also one of the most caring persons I have ever met. Without her I wouldn't be the same person I am today. She taught me a lot, guided and supported me through my whole time in LMSC. Thanks to her, at the end of my Ph.D. I feel more knowledgeable and confident. I want to pursue a career in science and follow her footsteps if I can manage.

When I started my Ph.D. LMSC consisted of 'the old team' . Anna Dalmau, Carlo Colombo, Daniel Rueffer, Martin Heiss, Bernt Ketterer, Eleonora Russo, Sonia Conesa-Boj and Yannik Fontana. I was fortunate enough to have a desk next to Anna, so that I could take advantage of her wisdom. She introduced me to the clean room and to the world of microfabrication. As a bonus she became an amazing friend who made me to feel at home in Lausanne. Carlo was always there with a kind and supportive smile and a refreshing point of view. I always felt more positive and motivated after our discussions. Daniel was one of the most helpful and sweetest colleagues one can ever have. I learned a lot from him about the MBE, electronics and maybe even a bit of coding. His enthusiasm is a great gift for people around him. Martin is one of the most 'informed' people I have ever met. He taught me a lot, not only about MBE but in general about science. I couldn't overlap much with Bernt, but we spent some quality time in the Raman Lab and at different bars of Lausanne. Eleonora and Sonia taught me a lot about growth and nourished me with their warm Mediterranean motherhood. I can still pronounce crystal facets in Catalan today thanks to Sonia. Then there was Yannik, with his sharp humor but kind heart. I very much enjoyed the time we spent together, cheesy jokes, Charlie the unicorn, loud laughter and of course high level scientific discussions. I would never think I'd feel so connected with a born and raised Vaudoise.

There were also temporary members of LMSC whom turned to be lifelong friends. Jane, Jil and Ignasi. We learned so much with Jane inside and outside of the lab. She was kind, friendly and very supportive. Ignasi impressed me by being the most organized Catalan I have ever known. I miss the days when we shared the office with him, Anna, Sonia and Yannik. And my sweet Gelato... Already the thought of you brings a smile to my face. You are the most sweet and

loving friend who extended her support from the labs of LMSC to cyber world. Although the physical distance between us seems to be increasing, I will always be there for you and I know it is likewise.

Then there was the 'new team'. Federico Matteini, Alberto Casadei, Jelena Vukajlovic, Heidi Potts, Francesca Amaduzzi, Esther Alarcon, Eleonora Frau, Dmitry Mikulik, Martin Friedl, Luca Francaviglia, Jean-Baptiste Leran, Andreana Dahlii, Simon Pablo Escobar and Pablo Romero Gomez. Federico was my Ph.D. brother. We supported each other through the sufferings of MBE, and his fellowship brought a special joy to the journey. I am glad we both made it to the end in one piece. Casadei was always there with a smile to remind me life is not that depressing in fact. I hope fortune keeps smiling on him. Another Italian beauty in the lab was Francesca. She always offered her help whether I had a problem with optics or life. I am so happy she has her little family complete now with adorable Alessandro. Then comes my favourite Croatian family, Jelena and his boys. Jelena was a great colleague and a dear friend. Always there to listen and support. I cannot thank them enough for all the help they offered me, delicious dinners and stay overs at Vukajlovic-Plestina residence. Thanks for all your love and all the hugs girls. If Fede was my Ph.D. brother Heidi was my Ph.D. sister. We spent a lot of time together going to MBE, fixing the MBE, trying to figure out intriguing growth results etc. I was very impressed by her hardworking attitude, discipline and kindness. She was an excellent colleague you can count on with any issue and she kindly offered her support whenever she felt that you needed it. Our recent MBE recruit was Martin. Martin ! you are a very smart and talented young man. (Yes I can say that now I am almost 30) I am sure you will be even more successful in the coming years. Thanks for making our life much easier with your excellent problem solving and optimization skills. Next person to thank is Luca. I first met Luca F. when he was doing his master thesis in our lab, a focused and quiet guy with his padawan braid. During years he became a full time colleague, office mate, CL co-responsible and a dear friend to me. Thanks for all the measurements and not complaining about me for constantly talking during them. Also thanks for taking care of me in Split and sacrificing part of your liver in that journey. Another member of the Italian mafia was Ele. It was a lot of fun to spend time together, running, skiing, girl nights. I must specially thank her for introducing me to the mountains and showing me that I can be stronger if I exercise. Jean-Baptiste! Already your arrival made my life so much easier. Thanks for joining LMSC, for being so eager to help and being so kind. I don't know how I will manage in a group without JB. Although she had to leave us at some point for an amazing career, an indispensable member of our lab was Esther. I learned a lot from her and always admired her for managing so many things together and still having time for friendly conversations. My sweet Greek friend, Andreana. We only spent a year together but it was an intense one. Being neighbors both in the scale of countries and in Sallaz was so much fun. You were there with me during a very difficult year. I cannot thank you enough for that. I know we have much more drinks to enjoy, series to watch together and nights to go out in our future. We will keep in touch. My newest office mate Simon Pablo Escobar Steinvall. I am so happy that we could overlap a bit so I could get to know him. Simon is a special guy. Thanks for helping me so much, already in your first months and taking care

of me at difficult times. I am sure we will meet again at different parts of the world. Our newest postdoc Pablo, thanks for your friendly attitude, spontaneous jokes and delicious hams.

There are 3 people who made my last year very beautiful and much more bearable: Mahdi, Edoardo and Lea. I was fortunate enough to help them a bit with their master thesis. Mahdi was the first one. The chosen one to discover A-wires whom I couldn't supervise much because he learned everything so fast already. Thanks a lot for being super kind to me all the time, and bearing with me during the times I was fighting with stress. Edoardo was the second one. He wasn't only dear to me but to all LMSC. He touched all of our hearts with his sweetness. Edo, you are the only one through all my life who could convince me to exercise regularly. You are a miracle. Thanks for the whole year, thanks for touching my life. You made a big change. And Lea, my dear girl. Thanks for your enormous support during the last year and your valuable friendship. I will miss your big smile and you to tell me not to worry. Being so smart and talented I am sure all of yours' future will be very bright.

During my last year there were other visitors of LMSC with whom we bonded strongly over a brief period of time. Natasa Vulic, Won Jong Kim, Pranit Iyengar, Marco Negri, Andrea Giunto and Sara Martí Sánchez. Natasa infected us with her passion of running and kindly taught us some tricks. These sessions were a lot of fun. Thanks girl ! WKim, was our dear Korean. He introduced us his amazing culture, made us laugh with his special jokes, and helped almost everybody in every way that he could. He is amazing. Pranito was the nicest, kindest colleague ever. Thanks for cheering us with your cute smile. Andrea thanks for bearing with my annoying jokes and nice conversations. Marco was so polite, so sweet and caring. It was unbelievable. Marco, thanks for taking care of not only me but all LMSC and organizing so many activities and trips.

There was also my non-LMSC entourage from EPFL. THEOS guys; James, Gian Luca, Martin, Leo and Nico, cute physicists Ghil and Riccardo. Brian from downstairs. My Turkish friends during my time in Lausanne: Ozgun, Mete, Mahmut, Gorkem and Sercan. My other friends from Lausanne: Despoina, Chiara, Jessica and Naima. Here, special thanks go to James, Gian Luca, Ghil, Riccardo and Andreana for creating such a warm circle where I felt loved and supported deeply during the most difficult times. I will miss you so much.

My lifelong friends from Turkey: Ipek for being always there for 10 years, day and night. Thanks for your endless support and love. My spiritual sister. Gokce for sticking with me since high school. Thanks for your endless compassion and love. I am looking forward to aging with you. Ulas Abi thanks for all the laughters, your great friendship and that long phone conversations.

Most of the experimental work would not have been possible without the support of CIME and CMI. I also want to acknowledge the valuable collaborations I was very fortunate to be involved in. Jordi Arbiol, Maria de la Mata and Sara Martí Sánchez from ICN Barcelona, Paulina Plochocka and Zhuo Yang from CNRS Toulouse , Romain Quidant and Esteban Bermudez from ICFO Barcelona, Martino Poggio with Davide Cadeddu, Floris Braakman and Nicola

Rossi from Basel.

I also would like to thank my jury members; Paul Muralt, Fabien Sorin, Craig Carter and Paulina Plochocka who kindly accepted to be in the committee and dedicated time to correct my thesis in their very busy schedule.

Last but not least I'd like to express my gratitude to the Tütüncüoglu family who supported me at each step of my life. Annecim, babacigim ve canim kardesim Canberk, iyi ki varsiniz !

Lausanne, 11 November 2016 G. T.

Abstract

This thesis is dedicated to the growth and characterization of the optoelectronic properties of III-V semiconductor nanostructures namely nanowires and nanoscale membranes. III-V semiconductors possess promising intrinsic properties like direct band gap, high electron/-hole mobility and spin-orbit interaction which makes them interesting for a wide range of applications such as high speed electronics, optoelectronics and photovoltaics. Nanostructures enable the exploitation and further functionalization of the inherent semiconductor properties. The nanostructures we study in the scope of this thesis are grown with molecular beam epitaxy which enables us to obtain ultra-pure nanostructures with high crystalline quality.

In the first part of this thesis we investigate and optimize the growth of GaAs nanowires both on silicon and GaAs substrates. We employ the self-catalyzed growth technique in order to avoid the risk of foreign metal contamination. Growth on Si substrates is interesting in views of enabling the integration of existing Si microtechnology and III-V technology. GaAs nanowire growth on (111) Si substrates is achieved with self-assisted and position controlled nanowire growth techniques. In both techniques, the effects of the silicon oxide thickness and composition along with the nature of the openings are investigated. GaAs nanowires grown on (111)B GaAs substrates are employed in optomechanical and optoelectronics applications. Pristine GaAs nanowires grown on (111)B GaAs substrates are employed in scanning force microscopy thanks to asymmetric orthogonal modes they exhibit. Furthermore, GaAs/AlGaAs heterostructure nanowires demonstrate lasing when their dimensions and AlGaAs capping are optimized.

The rest of this thesis is dedicated to the growth of defect-free structures. Two methods are presented to create defect-free pure zinc-blende GaAs nanostructures. The first one is to modify the polarity of GaAs nanowires. We optimize the growth parameters to obtain a high yield of (111)A nanowires on (100) GaAs. GaAs nanowires grown in (111)A direction exhibited a defect-free structure in contrast to the nanowires grown in (111)B direction. Our second approach is to grow elongated nanostructures and control their orientation to 'lock out' the defects. When these nanostructures, GaAs nanoscale membranes, are oriented in <11-2> direction on a (111)B GaAs substrate they exhibit pure zinc-blende crystalline structure. Their superior crystalline quality is confirmed with transmission electron microscopy and optical characterization techniques, i.e. photoluminescence and cathodoluminescence. Their growth mechanism and parameter window is investigated in detail. Next, GaAs nanoscale membranes are used as templates for quantum heterostructures. GaAs quantum wells are embedded in an

AlGaAs shell around the nanoscale membranes. They are found to exhibit bright luminescence with narrow linewidth. Additionally, local alloy fluctuations in the AlGaAs shell are investigated. They exhibited sharp and localized luminescence characteristics like self-assembled quantum dots.

Key words: III-V semiconductors, nanowire, nanombembrane, nanoscale membrane, nanoscale heterostructures, molecular beam epitaxy, optoelectronics

Résumé

Cette thèse est consacrée à la croissance et à la caractérisation des propriétés opto-électroniques de nanostructures semi-conductrices III-V, notamment les nanofils et les nanomembranes. Les semi-conducteurs III-V possèdent des propriétés intrinsèques prometteuses, comme une structure de bandes directe, une haute mobilité électronique où l'interaction spin-orbite, qui ouvrent un large éventail d'applications dans les domaines de l'électronique à haute vitesse, de l'opto-électronique et du photovoltaïque. Les nanostructures permettent l'exploitation et la fonctionnalisation de ces propriétés inhérentes aux semi-conducteurs. Les nanostructures que nous étudions dans le cadre de cette thèse ont été crûes par épitaxie par jets moléculaires (MBE), une technique qui nous permet d'obtenir des nanostructures ultra pures avec une haute qualité cristalline. Dans la première partie de la thèse, nous explorons et optimisons la croissance de nanofils de GaAs sur des substrats de silicium et GaAs. Nous utilisons la technique de croissance auto-catalytique afin d'éviter le risque de contamination par un métal étranger. La croissance sur des substrats de silicium est intéressante en vue de l'intégration de la micro-technologie du silicium existante avec la technologie III-V. La croissance de nanofils de GaAs sur des substrats de Si d'orientation cristallographique (111) est obtenue par les techniques de croissance auto-assistée et auto-organisée. L'effet de l'épaisseur et la composition de la couche d'oxyde de silicium et la nature des ouvertures sur cette couche sont analysés pour les deux techniques de croissance. Les nanofils de GaAs crûs sur des substrats de GaAs d'orientation (111)B sont utilisés pour des applications opto-mécaniques et opto-électroniques. Des nanofils de GaAs purs crûs sur des substrats de GaAs d'orientation (111)B sont utilisés en microscopie à force atomique grâce aux modes orthogonaux asymétriques qu'ils présentent. De plus, les nanofils à structure hétérogène de GaAs/AlGaAs montrent un effet laser quand ces dimensions et la couche de recouvrement d'AlGaAs sont optimisées. Le reste de la thèse est dédié à la croissance de structures exemptes de défauts. Deux méthodes sont présentées pour créer des nanostructures de GaAs de type zinc-blende pure sans défauts. La première méthode consiste à modifier la polarisation des nanofils de GaAs. En optimisant les paramètres de croissance nous avons réussi à obtenir un pourcentage élevé de nanofils orientés (111)A sur des substrats de GaAs orientés (100). Les nanofils crûs orientés suivant la direction (111)A montrent une structure exempte de défauts contrairement aux nanofils orientés suivant la direction (111B). La deuxième approche adoptée consiste à croître des nanostructures allongées (nanomembranes) en contrôlant leur orientation afin d'empêcher la création de défauts. Quand ces structures sont orientées suivant la direction <11-2> sur un substrat d'orientation (111)B, elles présentent une structure cristalline purement zinc-blende. Ce

haut niveau de cristallinité est confirmé par des observations au microscope électronique en transmission et des techniques de caractérisation optique, notamment la photoluminescence et la cathodoluminescence. Le mécanisme de croissance et la gamme de paramètres sont analysés en détail. En outre, les membranes à l'échelle nanoscopique sont utilisées comme patron pour la formation d'hétérostructures quantiques. Des puis quantique de GaAs sont encastrés dans une coquille d'AlGaAs tout autour des nanomembranes. Ils présentent une luminescence intense dans une largeur spectrale très étroite. En plus, les fluctuations de la composition de la coquille d'AlGaAs au niveau local ont été investiguées : ils montrent une luminescence intense et localisée similaire à celle caractéristique des boîtes quantiques auto-organisées.

Mots clefs : nanostructure III-V, nanofils, nanomembranes, membrane d'échelle nanoscopique, hétéroépitaxie des nanostructures, épitaxie par jets moléculaires, optoélectronique

Riassunto

Questa tesi tratta della crescita e caratterizzazione delle proprietà optoelettroniche di nanostrutture di semiconduttori III-V, in particolare nanofili e nanomembrane. I semiconduttori III-V possiedono promettenti proprietà intrinseche come il bandgap diretto, un'alta mobilità degli elettroni/lacune e un'interazione spin-orbita che li rende interessanti per una vasta gamma di applicazioni quali l'elettronica alle alte frequenze, l'optoelettronica e il fotovoltaico. Le nanostrutture consentono lo sfruttamento delle proprietà intrinseche del semiconduttore e ulteriori sviluppi funzionali. Le nanostrutture studiate nel presente lavoro di tesi sono state cresciute con epitassia da fasci molecolari, che ha permesso di ottenere nanostrutture ultra pure e con elevata qualità cristallina. Nella prima parte di questa tesi è stata studiata e ottimizzata la crescita di nanofili di GaAs sia su substrati di silicio che di GaAs. Abbiamo sfruttato un meccanismo di crescita auto-catalizzato per evitare il rischio di contaminazione da metalli estranei. La crescita su substrati di Si è interessante nella prospettiva dell'integrazione tra la microtecnologia al silicio esistente e la tecnologia III-V. La crescita dei nanofili su Si (111) è stata ottenuta con meccanismi di crescita auto-catalizzata e con controllo della posizione. In entrambe le tecniche, gli effetti dello spessore e composizione dell'ossido di silicio e la natura dei fori all'interno di esso sono stati analizzati in profondità. Nanofili di GaAs cresciuti su GaAs (111)B sono stati impiegati in applicazioni optomeccaniche e optoelettroniche. Nanofili di GaAs cresciuti su substrati di GaAs (111)B sono stati invece utilizzati per microscopia a forza atomica grazie ai modi asimmetrici ortogonali che presentano. Inoltre, nanofili con eterostrutture GaAs/AlGaAs hanno mostrato fenomeni laser quando le loro dimensioni e la copertura di AlGaAs è stata ottimizzata Il resto di questa tesi è dedicata alla crescita di strutture esenti da difetti. Vengono presentati due metodi per creare nanostrutture di puro GaAs zincoblenda esente da difetti. Il primo consiste nel modificare la polarità dei nanofili di GaAs. Sono stati ottimizzati i parametri di crescita in modo da ottenere nanofili (111)A con un'alta resa su (100) GaAs. Nanofili di GaAs cresciuti nella direzione (111)A mostrano una struttura esente da difetti in contrasto con quelli cresciuti lungo la direzione (111)B. Il secondo approccio consiste nel crescere strutture elongate e controllare la loro orientazione per segregare al di fuori i difetti. Quando queste nanostrutture, nanomembrane di GaAs, sono orientate lungo la direzione <11-2> su un substrato di GaAs (111)B, esse mostrano una struttura cristallina puramente zincoblenda. La qualità cristallina superiore è suffragata dalla microscopia elettronica a trasmissione e da tecniche di caratterizzazione ottica, nella fattispecie fotoluminescenza e catodoluminescenza. Il meccanismo e i parametri di crescita sono stati investigati nel dettaglio. Successivamente, nanomembrane di GaAs sono state

utilizzate come supporto per eterostrutture quantiche. Pozzi quantici di GaAs incorporati in uno strato di AlGaAs che ricopre la nanomembrana presentano una forte luminescenza con ridotta larghezza di banda. Per finire, fluttuazioni locali nella lega AlGaAs dello strato esterno sono state analizzate in dettaglio. Esse mostrano una stretta e localizzata luminescenza caratteristica dei punti quantici auto-assemblati.

Parole chiave: nanostrutture III-V, nanofili, nanomembrane, eterostruttura nano , epitassia a fascio molecolare, optoelettronica,

Contents

Acknowledgements **i**

Abstract (English/Français/Italiano) **v**

List of figures **xiii**

List of tables **xvii**

Introduction **1**

1 Epitaxial Growth of Thin Films and Nanostructures **15**
1.1 Epitaxial Growth of Nanostructures 21
1.1.1 Nanowires 21
1.1.2 Selective Area Epitaxy of nanostructures 28
1.1.3 GaAs nanoscale membranes 29

2 New Aspects in the Growth of Nanowires **31**
2.1 Self-catalyzed GaAs nanowire growth on (111)B GaAs substrates 32
2.2 Self-assisted nanowire growth on (111) Silicon 40
2.3 Position controlled nanowire growth on (111) Silicon 44
2.4 Self-assisted GaAs nanowire growth on (100) GaAs substrates: The role of polarity on the crystal phase 49

3 The Growth of GaAs Nanoscale Membranes **53**
3.1 Substrate Preparation 56
3.1.1 The effect of the roughness 57
3.1.2 Dielectric Layer Optimization 57
3.2 Growth Condition Optimization 59
3.2.1 Growth temperature 59
3.2.2 V/III Dependency 60
3.3 Growth Dynamics 64
3.3.1 Pitch Dependency 64
3.4 Growth mechanism 66

4 Optical Properties of Nanoscale Membranes & Related Heterostructures **71**
4.1 Growth of GaAs/AlGaAs heterostructure nanomembranes 71
4.2 Optical Characterization of the core/shell GaAs/AlGaAs nanomembranes . . . 76
4.3 Quantum heterostructures 82

5 Conclusion & Outlook **93**

6 Publication List **95**

Bibliography **111**

Curriculum Vitae **113**

List of Figures

1 Novel transistor architectures 2
2 Various examples of nanoscale heterostructures 4
3 Illustration of a RHEED system 8
4 Technical drawing of our MBE system 10
5 Illustration of our MBE system 10
6 Illustration of the direct and indirect band-gap semiconductors 11
7 Band-gap diagram of GaAs 12
8 Illustrations of PL and CL systems 12
9 Illustration of the CL hyperspectral maps 13

1.1 Epitaxial growth mechanisms 17
1.2 Wulff Plot of the interfacial free energy per unit area 18
1.3 Growth dynamics on the surface 19
1.4 VLS mechanism illustration by Wagner et al. 21
1.5 Binary phase diagram of the Au-Si system 22
1.6 Phase diagram of the GaAs system 24
1.7 The illustration of the VLS mechanism for GaAs nanowires 25
1.8 Phase diagram of the GaAs system 26
1.9 Nucleation points at different locations of the liquid solid interface 26
1.10 SAE mechanism illustration 28
1.11 Wulff Sahpe of GaAs 29
1.12 GaAs nanoscale membrane array and the faceting of an individual nanostructure 30

2.1 The growth mechanism of GaAs NWs on HSQ covered GaAs (111)B substrates . 34
2.2 Parameter window for GaAs NWs grown on HSQ covered GaAs (111)B substrates 34
2.3 TEM analysis of a GaAs nanowire grown on (111)B GaAs 35
2.4 Demonstration of the setup to characterize optomechanical properties of GaAs nanowires 37
2.5 Core/shell GaAs/AlGaAs nanowire growth mechanism 38
2.6 SEM images of GaAs/AlGaAs nanowires that exhibit lasing 39
2.7 The demonstration of the lasing and coupling to VG grooves 40
2.8 GaAs nanowires grown under identical conditions on different substrate batches 41
2.9 GaAs nanowires growths realized on Si(111) substrates with different thicknesses of oxides 43

2.10 The contact angle measurements and XPS analysis of substrates with different native oxide thicknesses . . . 44
2.11 Pattern preparation steps for Si(111) substrates . . . 46
2.12 The effect of the oxide thickness on the yield of GaAs nanowire arrays . . . 47
2.13 The effect of the Gallium predeposition on the yield of GaAs nanowire arrays . 48
2.14 Initial stages of the growth to pin Ga droplets . . . 48
2.15 CL HYP of GaAs nanowires grown on a (100) GaAs substrate . . . 50
2.16 <111> directions available on (100) GaAs surface . . . 50
2.17 Growth parameters to increase the ratio of A wires . . . 51
2.18 Detailed TEM analysis of (111)A GaAs nanowires . . . 52

3.1 SEM image and the illustration of a standard GaAs nanomembrane and faceting 55
3.2 TEM analysis of nanoscale membrane . . . 55
3.3 Substrate preparation steps of GaAs nanomembrane substrates . . . 56
3.4 The effect of roughness on the growth of the nanomembranes . . . 57
3.5 Nanomembranes obtained with different GaAs growth rates with fixed Arsenic pressure . . . 58
3.6 Temperature series to achieve selective area growth of the membranes . . . 60
3.7 Defects formed at the side facets of the nanomembranes at elevated temperatures . . . 60
3.8 Pitch Dependency of the GaAs nanomembrane height on Arsenic Flux for low growth rate . . . 61
3.9 Time series to achieve high aspect-ratio nanoscale membranes . . . 62
3.10 The Wulff shape of GaAs constructed by only {110} facets and nanomembrane geometry . . . 62
3.11 Nanomembranes obtained with different GaAs growth rates with fixed Arsenic pressure . . . 63
3.12 Nanomembranes obtained with different Arsenic fluxes at fixed GaAs growth rate 64
3.13 Pitch dependency of the membrane height . . . 66
3.14 GaAs nanoscrystals grown in hole and hexagon shaped openings . . . 67
3.15 AFM analysis of the membranes grown in different lengths of openings . . . 68
3.16 The effect of the length of the opening on the morphology of the nanomembranes 69
3.17 Early time series on different substrates . . . 69
3.18 Time series of the growth for 1 Å/s growth rate . . . 70

4.1 The growth of AlGaAs shell layer to create GaAs/AlGaAs nanomembrane based heterostructures . . . 72
4.2 The model and SEM image of a GaAs/AlGaAs nanomembrane based heterostructure . . . 73
4.3 The model and SEM image of a GaAs/AlGaAs nanomembrane based heterostructure . . . 73
4.4 HAADF image and EELS mapping of a vertical GaAs/AlGaAs membrane cross-section . . . 75

4.5 HAADF image of the membrane apex and EDX maps for As, Ga and Al 75
4.6 PL spectrum of GaAs/AlGaAs core/shell nanomembrane array 76
4.7 The comparison of temperature dependent PL and CL measurements 77
4.8 The comparison of temperature dependent capped and uncapped sample's PL spectra 79
4.9 PL spectra of capped and uncapped GaAs nanomembranes 80
4.10 Nextnano simulations to solve the band alignment of GaAs/AlGaAs interface for different concentrations of Aluminum 80
4.11 Power dependent PL measurements on $Al_{0.3}Ga_{0.7}As$/GaAs/$Al_{0.3}Ga_{0.7}As$ 20/5/20 nm nanomembranes 81
4.12 HAADF/TEM imaging of the QW embedded nanomembrane heterostructures 82
4.13 The illustration to demonstrate the directionality of Ga flux 83
4.14 Plot of the scalar products of the facet normal and flux vector from 0 to 2Pi for different facets 84
4.15 Lateral and vertical cross-section representations of QW heterostructures . . . 85
4.16 CL HYP of the membrane array and extracted spectra from pointed regions . . 86
4.17 PL spectrum of the 8 nm QW sample 87
4.18 CL mapping of the GaAs/AlGaAs core/shell nanomembrane array 88
4.19 CL mapping of the localized emissions in the different parts of the individual membranes 89
4.20 Average CL spectra collected from the different regions of the nanomembranes 89
4.21 Histograms of the emission centers in high energy range for different concentrations of Aluminum 91
4.22 PL spectra of excitonic features and their power dependence 92

List of Tables

1.1 Péclet numbers and corresponding growth regimes 20

4.1 Varshni parameters from the literature in comparison with our experimental data 77
4.2 Calculated relative deposition rates for different facets 85

Introduction

In 1965, Gordon Moore, the co-founder of Intel, predicted that the number of transistors on a chip would double in every 18 months.[1] Today, this prediction is known worldwide as Moore's law. Even if Moore's law is not a physical law, it determined the roadmap not only for Intel but also for the whole CMOS technology during the following years. It was valid for 50 years while semiconductor industry continuously developed from around $1 billion in 1964 to over $400 billion in 2015.[2] In the meantime, the dimensions of the transistors decreased, and this resulted with an increase in the number of transistors per chip, as well as the energy reduction and higher switching speeds. These two factors helped the device performance to ameliorate year by year. Such downscaling is achieved as a result of continuous research efforts to improve lithography and deposition techniques along with an effort to precisely control the doping profiles in nanoscale. Intel's recent 14 nm technology announcement embodies the use of FinFETS as 2nd generation tri-gate transistors and it is the state of the art in CMOS technology. [1] [3] This downward scaling is seriously challanged by high power consumption below a certain limit. The largest problem of the existing CMOS technology is the high power consumption caused by increasing leakage currents and the saturation of supply voltage scaling at around 0.8–0.9 V. In order to overcome the issue it should be possible to further reduce the operation voltage without causing a loss in the device performance. Such a practice would require novel device architectures, new physical mechanisms i.e. tunneling or alternative materials to Silicon (Si). [4]

Novel device architectures proposed include FinFETs and NanowireFETs which require switching from a planar channel to a 3D geometry.[5] [4] Their structures are illustrated in Figure 1 along with conventional planar MOSFETs. These transistors benefit from the improved electrostatic gates that encapsulate the carrier channel while maintaining the short channel length to have fast on/off ratios. III-V semiconductors are one of the strong candidates for such device architectures since they have the potential to inject more carriers in a faster manner compared to Si. The performance of InGaAs FinFETS was already shown to be superior to Si.[5]

Tunnel-FETs (TFETs) are another promising device system which employs an alternative operation mechanism rather than standard thermal injection of the carriers. [6] In TFETs charge carriers tunnel from one energy band to another energy band. Such a configuration can be achieved in a heavily doped p+ – n+ junction or heterostructures with a broken band

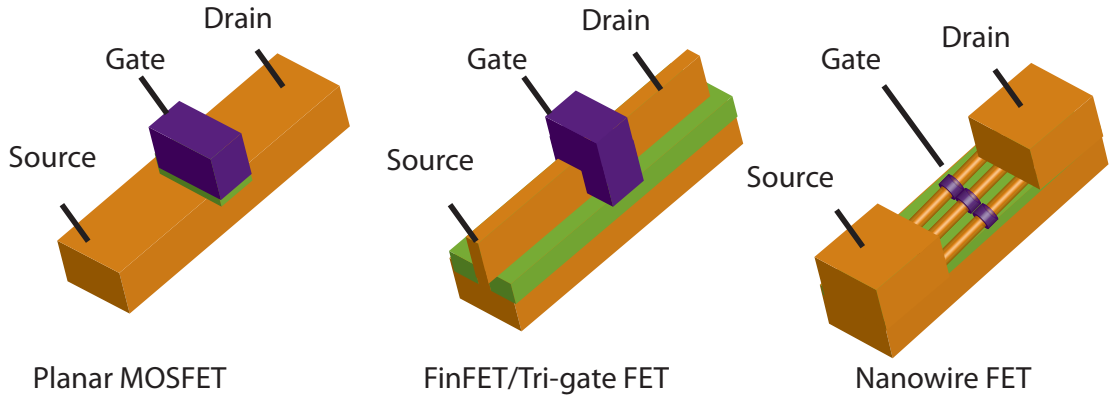

Figure 1 – Conventional planar MOSFET design along with novel transistor architectures of FINFET and NW-FET

alignment like InAs/GaSb. The improvement in the growth of III-V semiconductors and their heterostructures would be crucial for this technology as well.[7] In both cases functionalizing the inherent material properties for specific applications will come along with advantages such as material and cost reduction, thanks to the tools of advanced nanotechnology.

From another perspective, unlike Si, some of III-V semiconductors possess direct band-gap and thus a transition from Si technology to III-V semiconductors brings along the possibility to integrate efficient optoelectronic devices. Possible applications include tandem or stacked solar cells, detectors and integrated lasers. III-V nanostructures have enhanced absorption properties with the possibility to combine different material systems which make them promising candidates for PV applications.[8][9][10][11][12][13] Si and III-V nanostructures can be combined in mechanically stacked or tandem solar cell configurations to implement their attractive properties with the existing Si technology.[11][14] Another attractive optoelectronic application is lasing. Nanostructures, mostly nanowires, are shown to be versatile nanoscale light sources since they can provide both the gain and the medium thanks to their small geometry. Depending on the mode of lasing, their composition and dimensions can be varied to cover a wide range of the spectrum which is challenging to achieve in bulk. Additionally they can be integrated with purposely designed photonic circuitry to supply 'light' for integrated photonics applications.[15][16][17][18][19][20][21][22]
Lastly, employing III-V semiconductors in nanoscale, III-V nanostructures, enable us to benefit from quantum effects that appear in low dimensions, and to tune such effects by modifying the structure, morphology and composition. Products taking advantage of quantum effects, such as quantum cascade lasers, are already on the market. Thanks to the ongoing advanced research on fundamental properties of III-V nanostructures, it will be possible to build more sophisticated devices for applications of quantum information and technology or to study fundamental quantum mechanics related phenomena. In order to achieve all the aforementioned advantages, one needs to master to create efficient, reproducible, and defect-free III-V

nanostructures. A reliable method for this purpose is the bottom-up synthesis.

The bottom-up synthesis of III-V nanostructures

The bottom-up synthesis of III-V nanostructures could constitute an important step towards next generation electronics. Bottom-up considers building structures in a sophisticated manner from the smallest possible building blocks, in our case atoms or molecules. This method enables us to overcome the limitations of top down fabrication methods such as resolution limit of the lithographic process or surface defects induced during etching. Along the same line, the ability to design new material systems and combine different materials in sophisticated forms enable us to exploit and functionalize the properties of III-V semiconductors. Within this scope Molecular Beam Epitaxy (MBE) remains as a promising approach to grow high-quality semiconductor nanostructures in a reproducible way. During recent years it has been shown several times that epitaxially grown III-V nanostructures can be used for innovative applications such as solar cells that can exceed Shockley Queisser Limit[10] , detection of Majorana Fermions[23], and vertical high performance transistors.[24]

In the bottom up synthesis of nanostructures either a catalyst nanoparticle or sticking coefficient difference of growth precursors on different surfaces are employed. Two well-established catalyst induced nanowire growth modes are called Vapour Liquid Solid and Vapor Solid techniques. They will be explained in detail in the next chapter. The growth of other nanostructures like nanoflags, nanosheets, nanomembranes can be realized with or without using a catalyst particle. For the realization of such complex geometries either modification of the growth parameters, morphological features on the growth substrate or openings of desired shape and dimensions on a dielectric mask (in the case of selective area epitaxy) can be used.

Nanoscale Heterostructures with III-V Semiconductors

Heterostructures are material combinations where two or more layers of different semiconductor materials are grown on top of each other. The motivations of creating heterostructures could be various such as surface passivation, band gap engineering or observation of quantum effects. Although it is possible to realize heterostructures in bulk, nanoscale heterostructures enable us to design more sophisticated structures through geometrical variations. Upon achieving the growth of nanostructures, it is possible to create heterostructures axially or radially by changing the growth conditions. In Figure 2, selected examples of nanoscale heterostructures are demonstrated. Figure 2a) shows a radial heterostructure example of a core/shell GaAs/AlGaAs nanowire where quantum dots can be embedded within AlGaAs shells. Figure 2b presents the corner of a GaAs/AlGaAs nanoscale membrane where a GaAs quantum well is sandwiched between two AlGaAs layers. Figure 2c is a fine example of Si and III-V heterostructures, where an axial heterojunction is formed along a Si/GaP nanowire. Figure 2d differs from the other 3 examples because in that case heterostructure is formed without changing the material system through crystal phase engineering within the same GaAs nanowire. It is known that GaAs can exist both in wurtzite and zinc blende phases in nanoscale. Thanks to the type-II band alignment between wurtzite and zinc blende GaAs it is

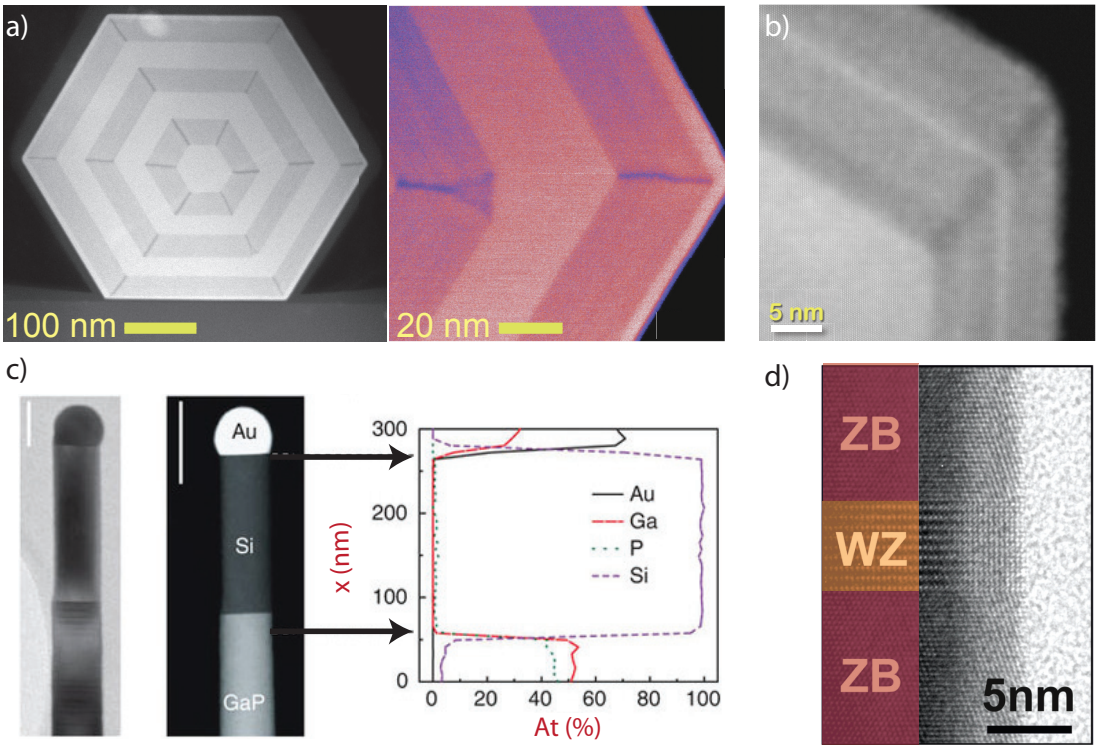

Figure 2 – Various examples of nanoscale heterostructures a) Core/shell GaAs/AlGaAs nanowires with self-assembled quantum dots (adapted from [25]) b) Corner of a GaAs/AlGaAs nanoscale membrane with GaAs quantum well (adapted from [26]) c) GaP/Si axial heterostructure along a nanowire (printed with permission © Nature Publications [27]) d) Thin section of wurtzite layer sandwiched between two zinc blende segments along a GaAs nanowire(printed with permission © ACS Publications [28])

possible to form homostructured quantum wells/dots along the axis of GaAs nanowires.

Nanostructures are excellent platforms to create quantum heterostructures thanks to their confined geometry. QDs within the axial heterostructure geometry, decorated at the side facets of the nanowires or embedded in the outer shells are demonstrated.[25] Several groups presented QW tubes around the nanowires and other nanostructures like nanofins and nanomembranes.[29][30][31][32][33][26] The inherent dimensions of the nanowires are reduced to below <20 nm to create quantum wires.[28][34] [35] Additionally, through doping of the radial heterostructures, two-dimensional (2D) carriers can be localized at the core/shell interface, or 1D channels can be formed at the apexes like quantum wires. [36][37][38]

In order to be able to build devices for future electronics and optoelectronics applications we need to be able to grow aforementioned nanostructures in an ordered manner. Although self-organization is appealing for being convenient and low-cost, the most reliable and reproducible options still include lithography. Some examples include photo- or e-beam lithography, nanosphere lithography, nanoimprint lithography etc. In this thesis we have realized both self-organized and position controlled growth of nanostructures. We tried to control

the density and the dimensions of the nanowires by only changing the surface properties without introducing a lithography step but when we wanted to strictly control the position of the nanostructures we still have used e-beam lithography since it is the most common and reliable technique up to now and our group already has the necessary know-how.

In this thesis the growth and optical properties of the ordered III-V nanostructures grown by MBE will be investigated. Those nanostructures are GaAs nanowires and GaAs nanoscale membranes along with based heterostructures. The outline is the following:

Introduction

Experimental Techniques: In this chapter an overview of the main experimental techniques will be presented. Overviews will include physical mechanisms beyond the techniques and technical details. We will start with the growth technique Molecular Beam Epitaxy and continue with optical characterization methods of photoluminescence, cathodololuminescence.

Chapter I: Epitaxial Growth of Thin Films and Nanostructures In this chapter the concept of epitaxial growth will be mentioned and well-known mechanisms of thin film epitaxial growth; Volmer-Weber Mechanism, Frank-van der Merwe Mechanism and Stranski-Kraskonow Mechanism will be introduced. Afterwards Vapour Liquid Solid, Vapor Solid and Selective Area Epitaxy which are known nanostructure growth methods will be detailed.

Chapter II: New Aspects in Nanowire Growth and Specific Applications In this chapter nanowires that are grown with the previously mentioned methods will be demonstrated. Afterwards their potential in different applications will be discussed. Such applications include scanning force microscopy, room temperature lasers, terahertz sources or detectors.

Chapter III: GaAs Nanoscale Membranes and Their Growth Mechanism After mentioning the epitaxial growth and certain applications of nanowires, an alternative geometry, GaAs nanoscale membranes are covered. GaAs nanomembranes have shown to bear potential to be used in future optoelectronic applications since they are defect-free when grown under optimized growth conditions and in specific directions.

Chapter IV: Heterostructures Based on GaAs Nanoscale Membranes and Their Optical Properties Upon achievement of defect-free nanomembrane growth, the structures are further functionalized with quantum wells and quantum dots. Optical properties of such heterostructures will be investigated by means of photoluminescence and cathodoluminescence.

Chapter V: Conclusion and Outlook

Experimental Details

Molecular Beam Epitaxy

"Epitaxy is the process of growing a crystal of a particular orientation on top of another crystal, where the orientation is determined by the underlying crystal." [39] This technique bears great importance for electronics and optoelectronics applications due to the high crystalline quality of the grown layer. There are well established epitaxial growth techniques such as Molecular Beam Epitaxy (MBE) Vapour-Phase Epitaxy (VPE), and metalorganic VPE (MOVPE) however within the scope of this thesis only the MBE technique will be explored.

An MBE chamber is an ultrahigh vacuum (UHV) system which enables the epitaxial growth of various materials varying from oxides to semiconductors.[40][41] Its main advantages are high quality, ultra-pure material growth, low growth rate (1-2 A/s) which enables abrupt junction interfaces and doping profiles, in situ characterization techniques and low growth temperatures (500-600 °C for GaAs).

MBE systems consist of stainless steel chambers equipped with high operation performance ion gauge pumps or cryopumps in addition to the cryopanels surrounding the walls of the chamber with flowing liquid nitrogen. The background pressure must be as low as 10^{-12} torr for the growth of high purity semiconductors. Growth material is supplied from effusion cells, which are directed towards the substrate holder at the bottom of the manipulator. Although the design of the cells can be different depending on the material to be evaporated and the needed temperature, the general scheme includes a pyrolytic boron nitride (PBN) crucible loaded with the growth material, which is surrounded with a heating system. There is an outer shell including several layers of Tantalum shield to prevent the loss of heat by radiation, as well as to reduce the waste of liquid nitrogen due to local heating. The temperature of the cell is measured with a thermocouple and regulated very precisely using the (Proportional-Integral-Derivative (PID) systems. Shutters in front of the effusion cells permit monolayer sharp interfaces since their switching speed can be faster than the growth of one monolayer. Shutters can be pneumatically driven or magnetically coupled.

The substrate is heated to elevated temperatures in order to ease the dissociation and diffusion of the incoming atoms on the surface and to allow for high crystalline quality epitaxial growth. Homogeneous growth over the whole sample surface is achieved through the rotation of the

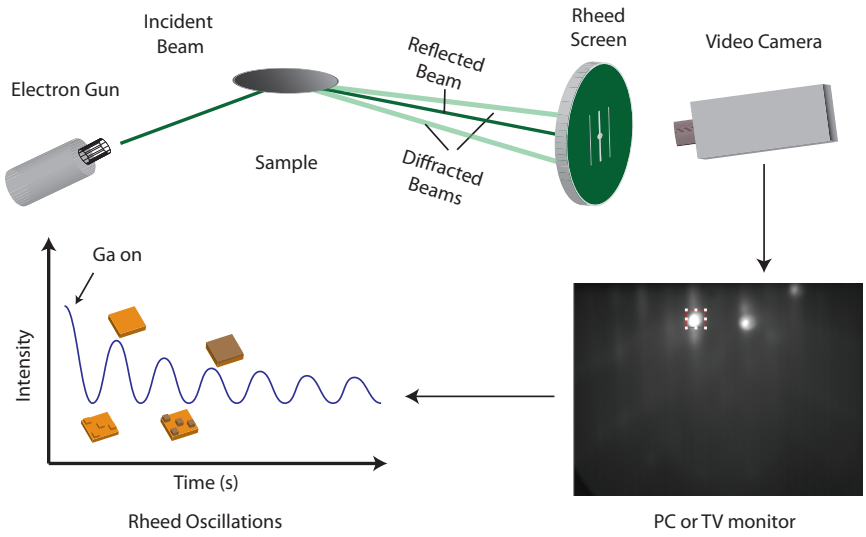

Figure 3 – Representation of a RHEED system

manipulator. Furthermore it is currently possible to grow on 8 inch wafers which is important for industrial applications.

Due to the UHV environment in MBE systems various in situ characterization methods can be implemented such as Reflective High Energy Electron Diffraction (RHEED), in situ X-ray diffraction (XRD), Beam Flux Monitor (BFM), Residual Gas Analyser (RGA) etc. In 1969 Cho et al. demonstrated the in situ observation of the MBE growth by Reflective High Energy Electron Diffraction (RHEED) which opened up the possibilities of high quality crystal growth by MBE and is followed by other innovations such as heterojunctions, quantum cascade lasers, superlattices etc. [42][40] In Figure 3, a RHEED system is depicted. Electrons emitted from an electron gun are scattered from the sample surface and impinge on a phosphorous screen. Due to the crystalline nature of the substrate, a diffraction pattern can be observed on the phosphorus screen, the diffraction pattern depends on the surface orientation and the reconstruction of the surface. Moreover it can enable us to distinguish 2D and 3D growth. In the case of 2D, layer by layer growth, by observing the changes in the intensity of the diffraction spots one can measure the monolayer growth rate. It is possible to convert monolayer growth rate to to the nominal growth rate of the specific crystal by scaling it to the lattice constant of the crystal.

In our group we use a DCA P600 MBE system. A technical drawing provided by the DCA is shown in Figure 4. This system includes a load-lock, a central distribution chamber (CDC) with a robot handler, a storage chamber, a degassing chamber, a hydrogen cleaning chamber and two deposition chambers. The load-lock, hydrogen chamber and two deposition chambers each have their own pumping systems and are isolated from the rest of the machine by UHV gate valves. Load-lock and storage parts can accommodate up to 8 substrates which can be

transferred among chambers with the robot handler.

The deposition chamber is equipped with two cryopumps made by CTI Cryogenics, CTI-8 and CTI-10 in addition to two liquid nitrogen flowing cryopanels at the top and bottom of the chamber. The minimum obtainable background pressure is 10^{-12} torr. Growth rate calibrations are performed bimonthly with RHEED system and flux measurements are performed with BFM, through automatized Python scripts. The chamber is constantly monitored with an RGA system to ensure that non-growth species are leveled below 10^{-11} torr in the system.

There are 11 cell ports at the bottom of the chamber as can be seen in Figure 5. Among the 11 ports, 3 of them are standard effusion cells: Gallium, Indium and Aluminum, 2 are valve cracked effusion cells: Arsenic and Antimony, and last 2 are sublimation sources whose purpose are doping: Silicon and Carbon. Additionally we have 1 blank port and 1 view port. There is a pneumatic shutter at the front of each cell to permit the creation of monolayer sharp interfaces.

The cells are positioned at 45 degrees with the substrate surface normal. Substrates are placed facing down in the fork of the manipulator. There is a thermocouple at the back of the substrate to measure its temperature and a pyrometer at the bottom of the chamber to measure the temperature on the sample surface.

In our growth experiments mentioned in this thesis, we have specified the growth rate, temperature, group III, group V fluxes and their relative ratios namely V/III ratio. Growth rate is deduced from RHEED measurements in the units of Å/s. Temperature is deduced from the readings of pyrometer. Group III and group V fluxes are deduced from the readings of beam flux monitor, which is a pressure gauge that can be positioned below the manipulator that holds the growth substrate.Therefore the units of measures are torr and they correspond to beam equivalent pressure.

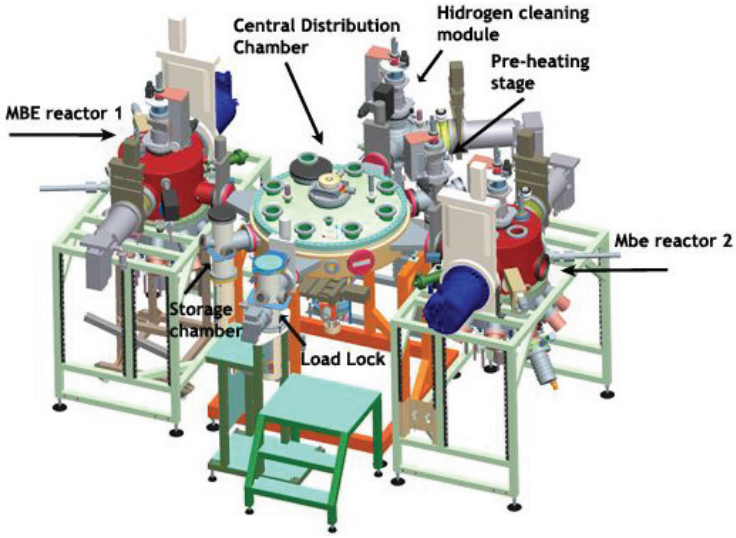

Figure 4 – Technical drawing showing the different components of the system. It is a P600 Dual chamber from DCA Instruments. Reprinted with permission from DCA Instruments Oy (http://www.dca.fi)

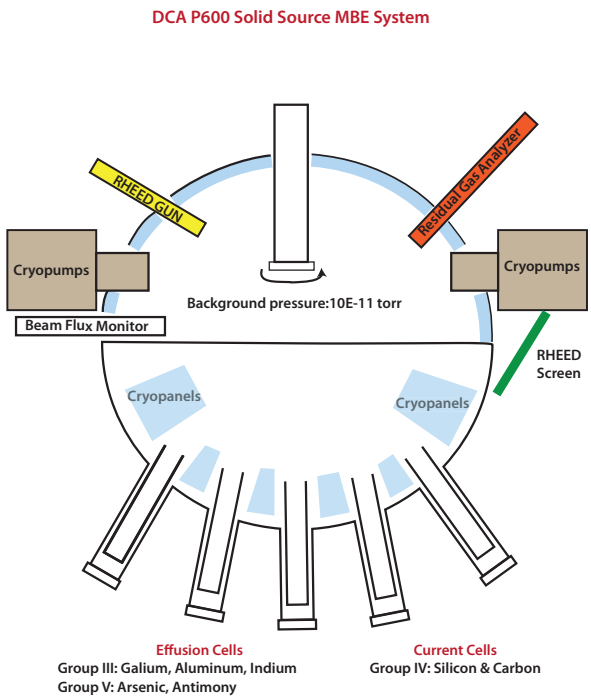

Figure 5 – The illustration of our MBE system

Optical Characterization Techniques

Luminescence typically originates from spontaneous recombination of electrons in the conduction band minimum with the holes in the valence band maximum, upon an electrical or optical excitation. The nature of the luminescence can be further classified as photoluminescence, electroluminescence or cathodoluminescence depending on the source of the excitation. In the scope of this thesis we have used photoluminescence and cathodoluminescence optical characterization techniques.

Photoluminescence

Bands in a semiconductor depend on the crystal structure of the material. Therefore luminescence characteristics will be determined by the crystal structure. Photoluminescence illustrations of band to band transitions for direct and indirect band gap semiconductors are presented in Figure 6.

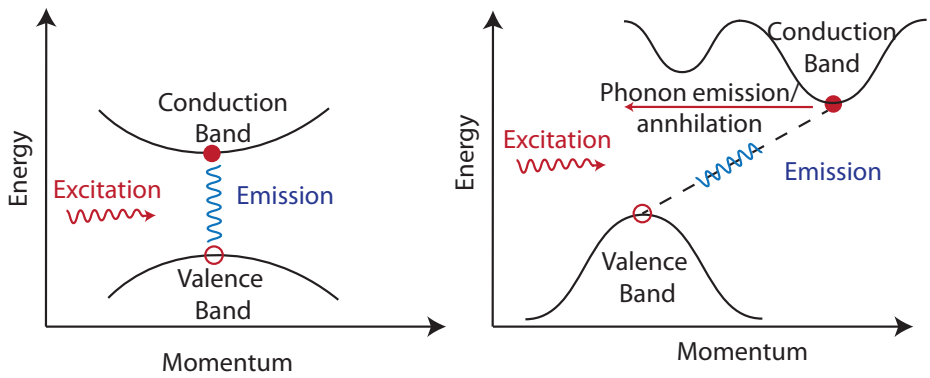

Figure 6 – a) Illustration of the excitation and emission in the direct band gap b) Illustration of the excitation and phonon assisted recombination in the indirect band-gap

If the valence band (VB) maximum and the conduction band (CB) minimum do not have the same momentum, luminescence is difficult to observe because electron-hole recombination has to be phonon assisted to conserve the momentum. This is the case when the minimum of conduction band and maximum of valence band are located at different points of the Brillouine zone, hence they are called indirect band-gap semiconductors. For the case of direct band-gap semiconductors electron-hole recombination is much more straightforward as no simultaneous phonon contribution is required. Consequently, an intense luminescence can be observed and it carries important information on the band gap type, energy, the exciton binding energy, impurities and possible defects in the crystal. In Figure 7 a simplified flat band band gap diagram of GaAs is presented. More realistic exciton levels would be represented by parabolic energy bands. [43]

Energy levels of the conduction and valence bands are presented together with the free exciton

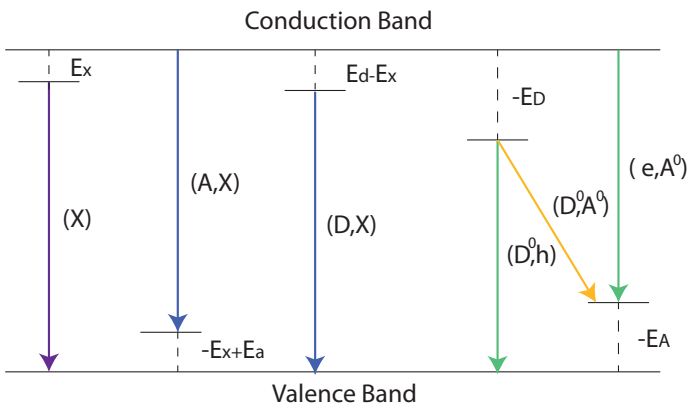

Figure 7 – Band-gap diagram of GaAs exhibiting donor and acceptor levels adapted from [44]

transition, donor and acceptor levels. If a high crystalline GaAs substrate is excited with enough energy and power, such transitions are observed in the PL spectrum.

A simplistic illustration of our PL setup is depicted in the Figure 8. The light source used was a He-Ne laser at 632.8 nm is partially reflected on a beamsplitter with reflection:transmission ratio of 1:9. The intensity of the transmitted light then can be monitored on the power meter and the reflected light is focused on the sample to be analyzed through an objective. The numerical aperture of the objective is 0.85 which leads to a laser spot of $\sim 1\ \mu m$. The sample is kept in a closed loop liquid helium cryostat with a base temperature of 3.85 K (Attocube 700). At the base temperature a vacuum level of $4 * 10^{-7}$ bar can be reached. The light emitted by the sample is redirected towards the spectrometer. A 500 mm focal length spectrometer is used with available gratings of 300,600 and 1200 l/mm. The detector is a Si charge-coupled device cooled down by liquid nitrogen.

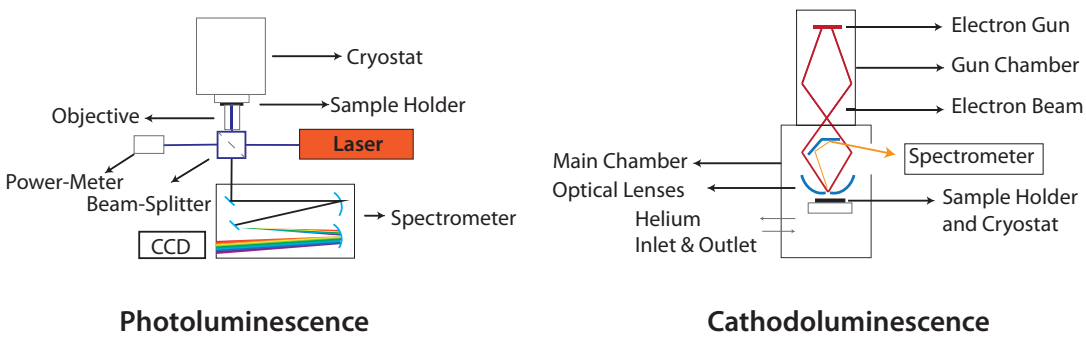

Figure 8 – Closed-loop cryostat PL system from Attocube and CL system from Attolight

Cathodoluminescence

The second optical characterization technique we used was cathodoluminesce (CL). In this technique the excitation source is the electron beam of an electron microscope. In our case we have used a CL system produced by 'Atttolight' which combines a scanning electron microscope (SEM) with an integrated light microscope, as shown in Figure 8.

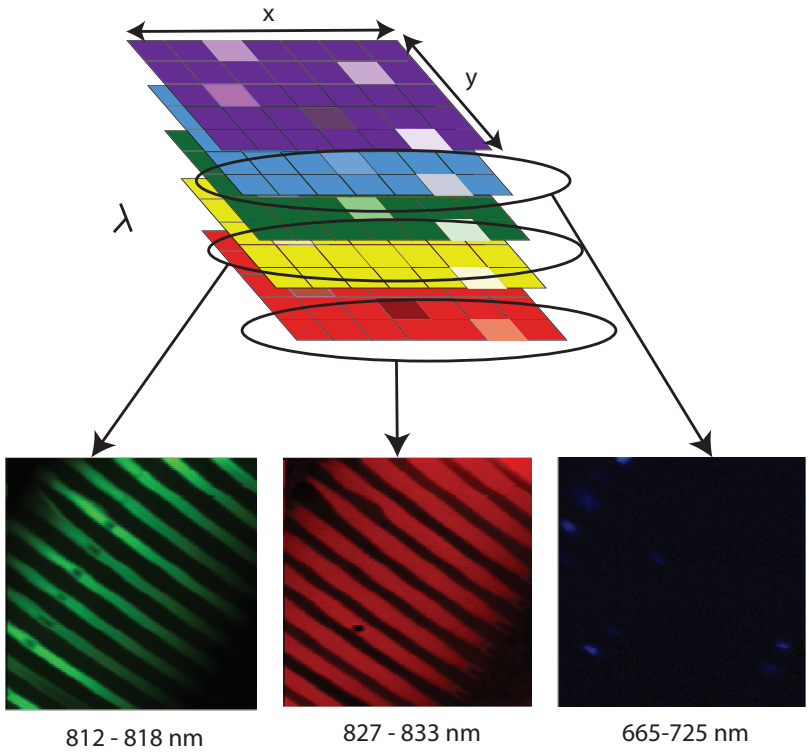

Figure 9 – Hyperspectral maps that we can obtain from CL analysis: Data is collected pixel by pixel from the user defined area for each wavelength. Monochromatic CL maps can be formed for Blue, Green and Red at desired ranges

The electron gun provides an electron beam with accelerating voltage between 1 and 10 kV. The generated current can be changed between 30 pA to 20 nA. The electron beam is focused on the sample by the gun's lens and objective lenses in the column. The emitted light from the sample is collected by the optical lenses and guided towards the spectrometer. This setup utilizes two detectors, Si and InGaAs, for different emission ranges of UV-Vis and Near-IR. Three gratings are available for 150 /500, 600/300, 600/750 lines/mm in addition to a blazed grating.

When the region of interest is characterized by CL a secondary electron image and hyperspectral maps (HYP) are obtained. The structure of a demonstrative HYP is shown in Figure 9. The region of interest is divided into pixels according to the given settings. A range between 16x16

and 128x128 is available. From each pixel full spectrum is collected for the desired range of wavelengths. From the resulting HYP monochromatic CL maps can be formed by assigning the each colour to a specific wavelength range. In Figure 9 wavelengths assigned to Blue, Red and Green are stated below Monochromatic CL maps. Spatial resolution of this technique enable us to distinguish different emissions originated from different parts of the sample.

1 Epitaxial Growth of Thin Films and Nanostructures

Crystals can be grown out of liquid or vapour phases depending on the growth technique and/or material. Understanding the driving forces behind crystal growth has been an intriguing discussion topic for the materials science and engineering community, since the microstructure of a crystalline material is crucial for several applications. Following the work of Gibbs where he defined "the formation of a new phase requires as a necessary prerequisite the appearance of a small number of building blocks (atoms or molecules)" it was hypothesized that supersaturation was the prerequisite of the crystal growth. [45]

Epitaxial growth is a special way of growing crystals in an ordered manner through which grown layers follow the crystal orientation of the host substrate. In the initial years of epitaxial growth, classical nucleation theory was applied to understand the underlying mechanisms. The initial calculations indicated that energy barrier was relatively high to form a 2D nuclei on a perfectly smooth 3D crystalline surface.[46] One would then need around 50% supersaturation for the precipitaton of nuclei. However, experiments indicated concentrations below 0.1% were sufficient. Pioneering work of Burton et al. shed light on the discrepancy. They pointed out that dislocations can trigger nucleation of 2D islands at much lower supersaturation (0.1%) and the distance between screw dislocations would correspond to the calculated critical sizes of 2D nuclei under given conditions. In their paper they also mention a transition temperature above which surface will be rough enough to provide nucleation sites for the growth.[46] Today we know that dislocations are not necessarily obligatory to initiate the growth of a new crystalline layer, but we do need atomic steps to offer energetically favorable adsorption sites to the incoming atoms to initiate heterogeneous nucleation.

Epitaxial growth performed in MBE has been of great experimental support through the development of the crystal growth theories. In an MBE chamber, crystal growth occurs at the surface of the substrate upon arrival and condensation of atoms and atoms do not interact on the way thanks to long mean free path of the atoms under UHV conditions. However, the growth process occurs under non-equilibrium conditions at elevated temperatures at UHV conditions. Therefore theoretical understanding of the crystal growth should be approached from both thermodynamic and kinetic point of view.

One general classification that can be made before moving onto thermodynamic and kinetic aspects of the epitaxial growth is the nature of the substrate and the deposit. The substrate on which epitaxial growth is ordered can be energetically (chemical potential) and geometrically (lattice constants) different from the deposited layer. In general the mechanism is called **homoepitaxy** if two crystals do not differ energetically (they are the same material). In homoepitaxy usually the purpose is to create a purer layer than the host material or to include/introduce doping. Homoepitaxial growth on different crystal orientations significantly differ in terms of growth conditions. [47] In homoepitaxy orientation dependence of the surface energy plays an important role as well. Hence, when the surface is not energetically stable microfaceting into lowest energy surfaces can be observed such as the cases of high-index substrates.[47][48][49] The other case where two crystals differ in composition or phase is called **heteroepitaxy**, i.e. the growth of AlGaAs on GaAs, Ge on Si etc.[50] If the lattice constants of two layers are different, grown layer can be strained or the strain can be released via interfacial or bulk dislocations. This kind of defect is detrimental for electrical and optical properties. From a thermodynamic and macroscopic point of view, homoepitaxy should be more straightforward since the chemical potential of the grown layer is identical with the host crystal. As a consequence, the Gibbs free energy of the system should not change under constant pressure and temperature. In the case of heteroepitaxy, interfacial bonding and strain play important roles on the overall Gibbs free energy of the system. Since the epitaxy of a new layer is also a process of wetting we can observe the change in the Gibbs free energy of the system per surface area through the change in the surface energy.[48] So the change of the surface energy can be written as:

$$\Delta\sigma = \sigma + \sigma_i - \sigma_s \tag{1.1}$$

Where σ is the binding energy of two surfaces, σ_i is specific interfacial energy and σ_s surface energy. Depending on the change in the surface energy Bauer et al. proposed 3 main growth modes which are Frank-van der Merwe, Volmer-Weber and Stranski Krastanov modes in 1958. [51]

Figure 1.1 depicts the characteristics of the three growth modes. In the case of Frank-van der Merwe, growth progresses layer-by-layer. It is energetically more favorable to form new layers:

$$\sigma_s > \sigma + \sigma_i \tag{1.2}$$

In the case of Volmer-Weber mechanism the films grows in 3D islands, since complete wetting is energetically not favorable:

$$\sigma_s < \sigma + \sigma_i \tag{1.3}$$

In Stranski-Krastonov (SK), layer by layer growth is followed by 3D island formation. This is because significant lattice mismatch strain energy is built in the initial layer(s) and after a

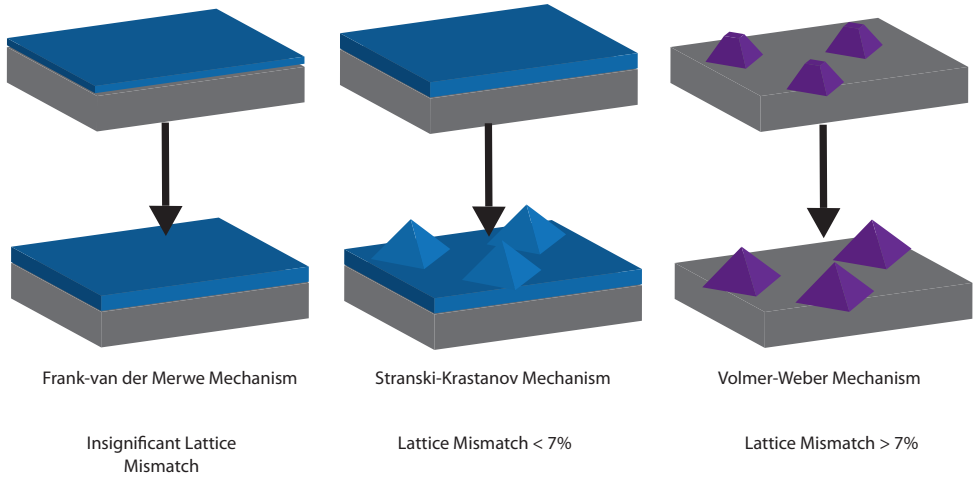

Figure 1.1 – Epitaxial growth mechanisms

critical thickness the system relaxes elastically forming nanoscale 3D islands upon deposition of few nanometers. The process is a combination of strain and surface/interface energy. A thin film remains below the islands, known as wetting layer. SK process might conclude coherently if system does not form a misfit dislocation. II-VI and III-V SK growth to form quantum dots are reported in the literature.[**?**] Coherent InAs SK islands on GaAs substrates are widely studied as they exhibit the band structure and properties of quantum dots whose physical properties can be tuned with growth parameters. .[52][53][54] They have been used in many applications like single-photon emission[55], light-emitting diodes [56], memories[57], and multicarrier solar cells [58].

SK growth of InAs on GaAs does not work well on every kind of surface. It has been shown that on (110) and (111)A surfaces InAs growth proceeds layer-by-layer with formation of misfit dislocations while on (111)B, growth proceeds in Volmer-Weber mechanism by forming discrete islands. Even on (100) GaAs substrates where formation of Qdots is more straightforward, the surface reconstruction becomes crucial for the growth of InAs SK Qdots.[29] For SK growth besides the quantities of surface energies of InAs and GaAs interfaces and the elastic relaxation energy of the islands, the absolute InAs surface energies of the involved facets should be also considered to predict the shape and size of the islands. In general for the cases of 3D growth, crystals take the most energetically favorable configuration which will be formed by lowest surface energy facets in that particular condition. This configuration is called Equilibrium Crystal Shape (ECS) which can be also defined as the shape in which crystal has the minimum free energy in the limit of infinitely large volume. The most well-known theory to calculate ECS is the Wulff theory which has been already proposed in 1901.[59] In Figure [**?**] a 2D Wulff plot is shown. It's a polar diagram of the interfacial free energy per unit area and its dependence on the orientation relative to crystal axes. We can try to understand the construction of a Wulff diagram by looking into the Helmholtz free energy change during crystallization.[60]

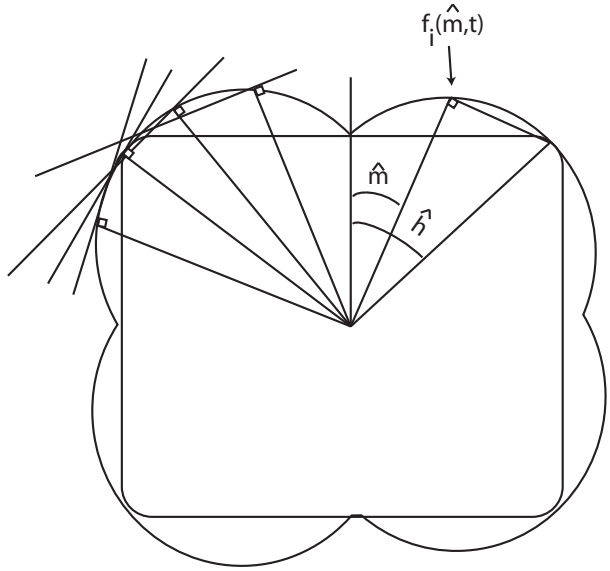

Figure 1.2 – Wulff Plot of the interfacial free energy per unit area and its dependence on the orientation relative to crystal axes $f_i(\hat{m}, T)$ is the interfacial free energy per unit interfacial area, $\hat{m}$ and $\hat{h}$ are orientations of the surfaces relative to crystal axis [60]

Helmholtz free energy of a crystallization from liquid can be written as following:

$$F(N, \Omega, T) = f_b(n_s, T)V(w) + f_b(n_f, T)(V(\Omega) - V(w)) + F_i(T, w) \tag{1.4}$$

where $f_b(n_s, T)$ and $f_b(n_f, T)$ are the bulk Helmholtz free energies per unit volume of the coexisting solid and liquid phases while $F_i(T, w)$ represents the contribution to the overall free energy arising from the inhomogeneous, interfacial regions which separate the homogeneous parts. N is the number of particles in a fixed volume of Ω and w is the solid macroscopic formations. Naturally we are interested in the term $F_i(T, w)$ when we are looking into crystallization and the crystal shape so we can write its dependence on the change in the surface of the crystal as:

$$F_i(T, w) = \int_{\delta w} dS f_i(\hat{m}, T) \tag{1.5}$$

$f_i(\hat{m}, T)$ is the interfacial free energy per unit interfacial area and depends on the orientation $\hat{m}$ of the surface relative to crystal axis. Wulff solves that constrained energy minimization problem by considering the assumption of having a fixed number of atoms in the system. Result is demonstrated in a straightforward way in a Wulff diagram that is shown in Figure 1.2. So in order to solve the ECS at a particular temperature one needs to ;

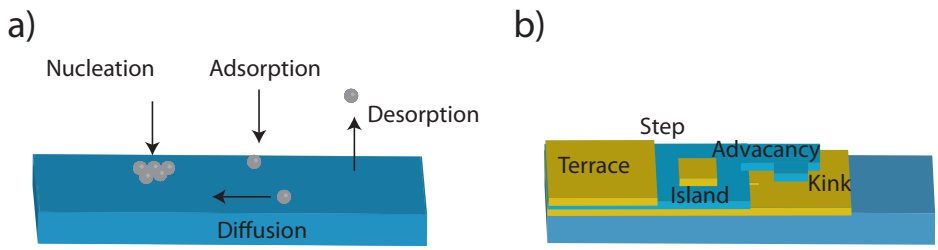

Figure 1.3 – a) Dynamics of the adatoms arriving to the surface b) Available attachment sites for the adatoms adapted from [60]

i) make a polar graph of $f_i(\hat{m}, T)$ as a function of $\hat{m}$
ii) draw the radius starting from the origin in the direction of $\hat{m}$
iii)draw a tangent line to the plot periphery at the intersection of the radius with the plot
iv) repeat it for all possible $\hat{m}$ directions
v) Resulting convex shape within the plot is the ECS of the material at given temperature [60]

According to Wulff's solution to ECS, the distance of the facets to the center of the crystal is proportional to their free energies and it is possible to construct the Wulff shape of a crystal when surface energies of facets are known. In his seminal paper, Herring shows that only surfaces which appear in the ECS are thermodynamically stable. Any surface that is not presented in ECS would lower its energy by breaking into "hills and valleys" of the surfaces which are present in ECS. This work is also considered as the completion of Wulff's initial theory. [61]

Wulff construction determines the equilibrium shape of the crystal in an homogeneous environment when the only contribution to excess free energy is interfacial energy and the volume is fixed.[62] However, the application of this theory to experimental data has proven to be challenging because it is highly limited by the requirement of equilibrium, while most crystal growth processes take place in conditions far from equilibrium. It is therefore relevant to also add kinetic considerations. In Figure 1.3a, a schematic drawing of the atomistic model of a surface in epitaxy with possible pathways of the atoms that arrive to the growth surface (adatoms) are shown. Since all growth reported in this thesis is performed with MBE, dissociation processes on the surface are not considered.

In addition to surface and interface energies, the surface morphology is determined by the dynamics of motion and interactions of the steps/terraces, 2D islands and adatoms. The possible attachment sites are demonstrated in Figure 1.3b. Different growth regimes can be classified using the parameters of the average spacing between the steps L, deposition rate j and adatom diffusivity D as presented in Table 1.1. In that case, the average velocity of step advancement rate would be $v_s = jL$ and adatom velocity is $v_{ad} = D/L$. The ratio of step advancement rate and adatom velocity can be used to classify and to indicate the relative

Péclet Number	Growth Regime
$L^2 j/D << 1$	Diffusional Step Flow
$L^2 j/D \approx 1$	Convective Step Flow
$L^2 j/D > 1$	2D Nucleation and Growth
$L^2 j/D >> 1$	Statistical Growth

Table 1.1 – Péclet numbers and corresponding growth regimes

importance of convective and diffusional growth rates. This ratio is called Péclet number as $L^2 j/D$. For $L^2 j/D$ much smaller than 1, the adatom diffusivity is higher compared to deposition rate and average step spacing. In that case, adatom diffusion to nearby steps would determine the growth rate of the steps which would correspond to diffusional step flow. When both velocities are comparable and Péclet number is close to unity, growth occurs through convective step flow where both adatom diffusion to the steps and step flow through adatoms contribute to the growth. When adatom diffusivity is slower than the deposition rate and terraces are large enough 2D nucleation becomes dominant since adatoms start to nucleate before they reach to nearby steps. Finally if the deposition rate is very high compared to diffusivity, atoms will stick wherever they are deposited and growth will be guided by statistics.

The 2D nucleation mode is more probable to occur on singular facets while step flow is more likely to happen on vicinal surfaces. There is another effect that we need to consider which makes sticking process of an adatom 'step asymmetric.'[63] This effect is called Ehrlich-Schowebel (ES) effect which is the existence of additional barriers to ad-atom hopping at step edges. In other words, atoms deposited on terraces of different heights tend to attach to the step edge of upper terrace. Hopping down to the lower terrace would bring additional barrier of passing through a section with low number of nearest neighbors. It was first discovered by Ehrlich and Hudda in 1966 and Schwoebel and Shipsey showed that the ES effect has stabilizing effects on the planar growth of vicinal surfaces. [64][65] However on high index surfaces the ES effect would have a destabilizing effect. For example, for {110} GaAs surfaces Tejedor et al reported that a high degree of step bunching is observed when grown under the same conditions as smooth {100} GaAs epitaxial growth. [66] The density and size of those steps are shown to be changing in a function of V/III ratio and growth temperature. Under low V/III ratios or high temperatures the ES effect is observed to lead to fewer larger sized terraces as growth continues. Under high V/III ratio or lower temperatures negative ES effect is observed which is caused by the high incorporation energy of Ga adatoms to existing upper terraces since they had {112} type step edges.

In conclusion, it is necessary to consider both thermodynamics and kinetics approaches when trying to understand and optimize epitaxial growth of thin films. They are equally important to achieve defect-free epitaxial layers or to predict equilibrium shapes of the crystals in case of 3D growth under the non-equilibrium growth conditions of MBE.

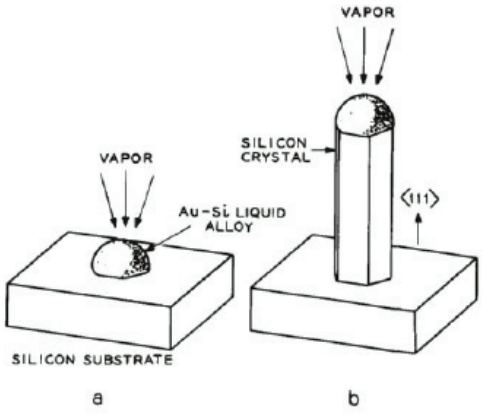

Figure 1.4 – The Wagner-Ellis illustration showing the growth of a silicon whisker by VLS: a)liquid droplet on the substrate at the initial stages of growth; b) growth of the crystal under the droplet. Reprinted with permission from [67]. © Applied Physics Letters 1964, AIP Publishing LLC.

1.1 Epitaxial Growth of Nanostructures

In this part, the growth mechanisms of nanostructures, including nanowires, will be covered. The growth of nanostructures requires a slightly different approach than the thin film growth due to geometrical constraints and larger effect of surfaces. We will start with the vapor-liquid-solid growth mechanism of nanowires and follow with the selective area epitaxy growth mechanism for both nanowires and other nanostructures.

1.1.1 Nanowires

Vapor-Liquid-Solid (VLS)

VLS is a well-established and commonly used nanowire growth mechanism. In VLS growth, the phases of vapour (growth precursors), solid (substrate) and liquid (the nanowire droplet) coexist during the growth. It was proposed in 1964 by Wagner and Ellis for the growth of Si whiskers, the name used in that time for high-aspect ratio crystals.[67] The original sketch of their proposed mechanism is shown in Figure 1.4. In reference [67], gold is used as the liquid catalyst, and the vapor precursors of $SiCl_4$ and H_2 for the silicon growth. The function of the droplet is to decompose and collect growth precursors. It also facilitates nucleation at the boundary between liquid and solid phases when supersaturation is reached. The epitaxial relation with the substrate determines the orientation of the growth. The droplet can be formed by a foreign material like gold or by one of the growth precursors like gallium in the case of GaAs growth.

The phase diagram of the materials involved in the VLS process helps us to understand the

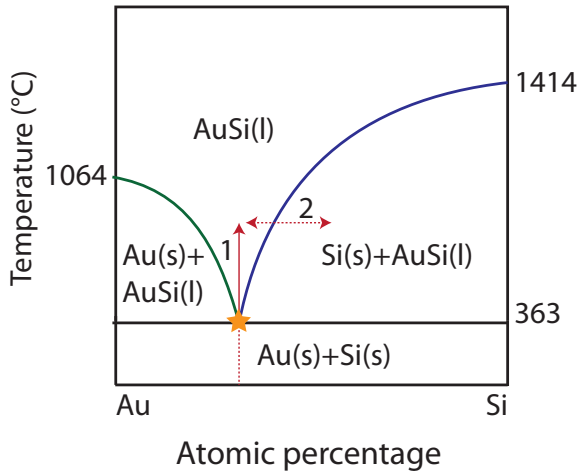

Figure 1.5 – Binary phase diagram of the Au-Si system for constant pressure of $10^{-5} bar$ adapted from [75]

physics behind VLS growth better. In Figure 1.5, the binary phase diagram of Au and Si is given which shows the stable forms of Au and Si at constant pressure of 10^{-5} bar for a range of temperature and relative concentration. Blue and green lines represent the liquidus lines (solid/liquid interfaces) of Au and Si along which they can exist in both solid and liquid forms. For the given conditions, the eutectic temperature of the system is 363°C with 19% Au. This value is the minimum temperature where the alloy can exist in the liquid form and it is lower than both individual melting points of Au and Si. The VLS process is illustrated with red arrows in the phase diagram for an arbitrary temperature value above the eutectic point. Usually the metal nanoparticles are first heated up above the eutectic temperature for the target metal–semiconductor system to create a liquid metal–semiconductor eutectic alloy. (Step 1) As the liquid droplet is continuously fed by growth substances during growth, it reaches supersaturation. Since this condition is not thermodynamically at equilibrium and non-stable, system is driven to the right of the phase diagram (Step 2) and precipitation occurs at the liquid solid interface which is the top facet of the nanowire. Consequently the concentration of Si in the liquid droplet drops and system returns to the previous state. It has been shown that the growth is driven by those discrete nucleation steps, also called anti-bunching nucleation events.[68][69] An in depth view of nanowire growth theory and nucleation is beyond the scope of thesis. For extensive reviews on the theory of nanowire growth and on nucleation dynamics, we refer to references[70][69][71][72][73][74]. It is important to note that catalyst droplets are reported to exist in liquid form below eutectic temperature as well. This behavior is attributed to nanoscale size effects in particular Gibbs-Thomson effect. [76] However, Kodambaka et al. reported that nanowire growth realized below the eutectic temperature is related to the kinetic enrichment of the eutectic alloy composition in Ge/Au system through in situ TEM observations. Growth pressure and thermal history of the catalyst droplet determine

its physical state. They also confirmed that growth continues regardless of the state of the catalyst.[77]

The first step towards achieving the VLS growth on a substrate is the dewetting of the droplet. For droplet formation one can use a metal catalyst which dewets and forms the optimum contact angle with a specific substrate or modify the substrate surface in a way to facilitate droplet material to dewet. Both methods are used for foreign metal catalyst induced and self-catalyzed growths.

Foreign Metal Catalyzed VLS, review of metals used

The most common metal used for particle assisted VLS growth mechanism of nanowires is still Au for various reasons such as;

i) Detailed knowledge about nanoparticle formation and dewetting mechanism of gold layers, [78]
ii) Its inertness to oxygen,
iii) Gold's ability to form alloys with different growth precursors,
iv) High diffusivity of growth elements through gold,
v) Providing a relatively more straightforward technique for phase engineering.[79][28]

Other metals have also been reported to be used as catalysts for III-V nanowire growths such as Mn, Al, Ti, Sn,Si.[80][81][82][83][84] If gold or any other foreign metal is used to initiate the VLS growth, the need for oxide layer on the substrate might be avoided since gold does not wet well most common growth substrates like Si, GaAs etc. Over the recent decades a detailed knowledge has been developed to use gold droplets as growth catalysts for VLS. Gold droplets can be drop-casted, manipulated by atomic force microscopy, created by heating to induce dewetting of a thin gold layer before growth or can be positioned through photo/e-beam/nanoimprint lithography. [85]

Despite all present experience and aforementioned advantages, it is desirable to eliminate Au from the process sequence in order to enable future integration of III-V semiconductors with Si. The reason for elimination is that Au created deep level impurity states in Si [86], and its incorporation in nanowires during growth, although still controversial, has been reported.[87][88][89][90]

Self-catalyzed VLS

In order to avoid the contamination issues linked with the use of Au, Fontcuberta et al. proposed to use one of the growth precursors as growth catalyst in 2008 for GaAs nanowire growth. [91] Figure 1.6 shows the phase diagram of GaAs at constant pressures of 10^{-5} and 10^{-9} torr. The stability of the different phases of GaAs compound is demonstrated in a range of temperature and composition. Below the phase diagrams molar gibbs free energies of specific phases are also plotted. This diagram shows that it is possible to condense stoichiometric

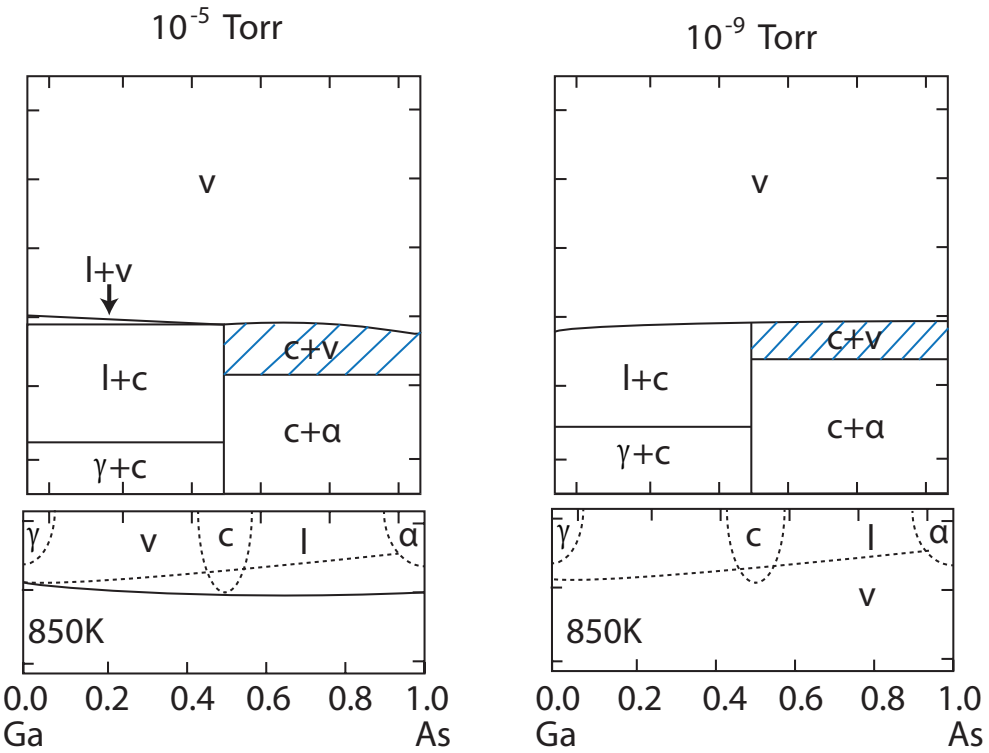

Figure 1.6 – Binary phase diagram of the GaAs system for constant pressures of 10^{-5} torr and $10^{-9}\,torr$ adapted from [49]

GaAs both from vapor phase or liquid phase at a broad range of temperatures. This generally makes epitaxial GaAs growth more forgiving. It also renders self-catalyzed GaAs nanowire growth possible. The shaded area shown in the phase diagram corresponds the growth window of GaAs thin film growth from vapor phase. For nanowires we need to be in the regime where Ga(l) should coexist with GaAs(s) and vapour phases but as it is shown in top right of Figure 1.6, the crystal phase should still be energetically more favorable than the liquid form. This point is called congruent evaporation temperature since it is also the point where GaAs evaporates stoichiometrically without forming Ga droplets on (100) surfaces.[92] Another requirement for Ga-assisted growth of GaAs nanowires is the dewetting of Ga from the surface. In order to achieve the dewetting, a thin layer of oxide is deposited or grown on the growth substrates. It has been shown that the thickness and the composition of the oxide strongly affect the nanowire formation, density and dimensions. [93] A schematic of self-catalyzed GaAs nanowire growth is shown in Figure 1.7. Our results on VLS grown GaAs nanowires will be given in the next chapter.

Self catalyzed technique offers the possibility to avoid Au for the VLS growth of GaAs nanowires in order rule out Au related defects. Moreover, the use of Ga droplet enables the full consumption of the droplet upon interruption of Ga flux and makes further functionalization of the

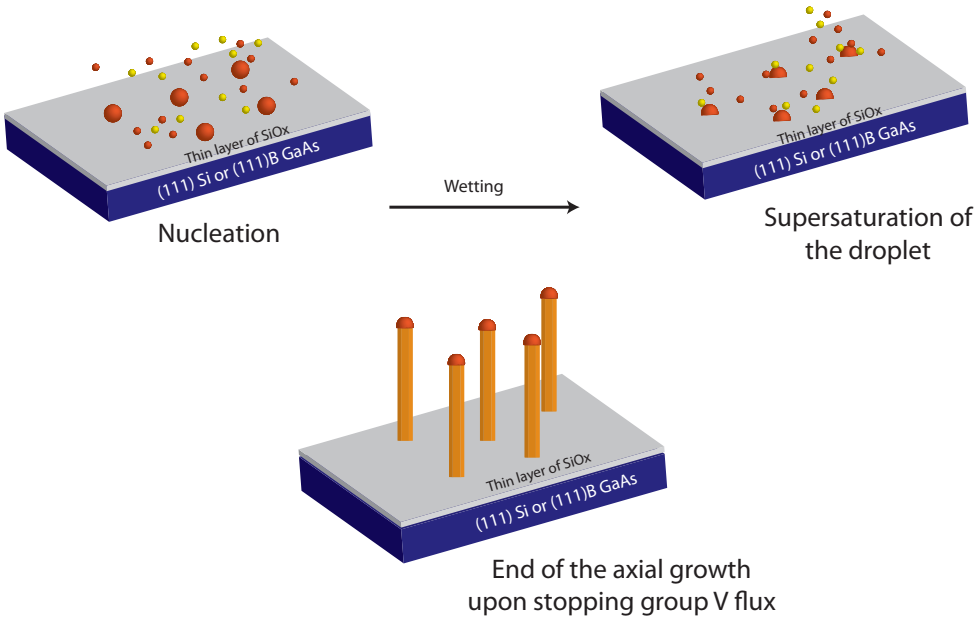

Figure 1.7 – The illustration of the VLS mechanism for GaAs nanowires

nanowire tip possible.

Polytypism in GaAs nanowires

Most III-V semiconductor compounds adopt a zinc-blende structure in the bulk form. However at the nanoscale, they are found to adopt both zinc-blende (ZB) and wurtzite (WZ) structures. Coexistence of both phases through the formation stacking faults or twins is commonly observed in GaAs nanowires. In Figure 1.8 atomic structures of both ZB and WZ phases in <111> and <0001> growth axes are shown. The zone axis in (110) for ZB and (1120) for WZ. A,B and C notations are used for Ga-As dimers (bilayers). ZB phase is following the stacking order of ABCABC while WZ phase is following the stacking order of ABABA. The cohesive energy difference between GaAs ZB and WZ phases is reported to be 24 meV per III-V pair. [94]

WZ and ZB bandgaps essentially have almost the same band gap energy, but there is a 100 meV offset between the band edges which creates a type II band alignment. Due to this discontinuity a spatial separation of the charge carriers occurs which leads electrons to be confined in ZB part and holes in WZ. This can be detrimental for optical and electronic properties since it will cause a power dependent emission behavior and longer lifetimes. At low power, the transition occurs between the conduction band of ZB and valence band of WZ. As power increases more states are filled at the interface between ZB and WZ, and finally only recombination at the ZB band is observed. [96][97] [98] [99] Several theories have been proposed to explain the formation mechanism of WZ in nanowires. Due to lower energies

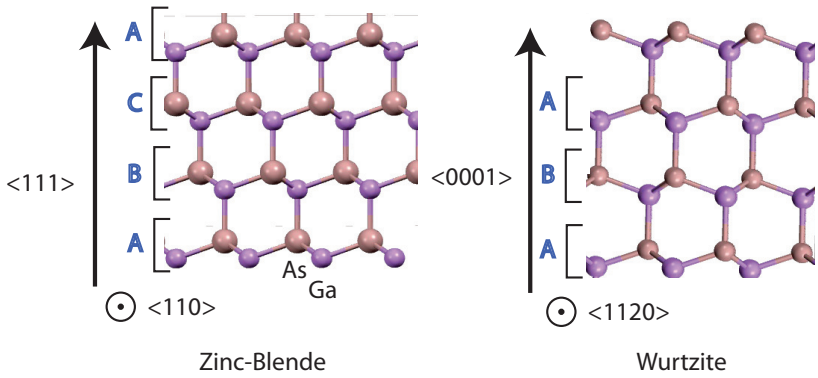

Figure 1.8 – Atomic structures for a) ZB crystal phase b) for WZ crystal phase (adapted from [95]

of the lateral facets of the hexagonal wurtzite nanowires growing in <0001> direction, it has been suggested that as the radius of the nanowire is getting smaller more contribution from the facets (higher surface-to-volume ratio) would stimulate the crystal to adopt WZ shape. [100]However this theory would imply stable GaAs WZ nanowires for diameters below 10-11 nm which does not agree with the experimental results.

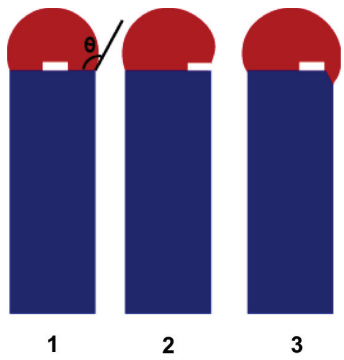

Figure 1.9 – Nucleation points at different locations of the liquid solid interface [101][74]

More elaborate theories that followed were based on the nucleation mechanism and the position of the nucleation event within the droplet. In Figure 1.9 3 possible nucleation locations are depicted at the interface between liquid droplet and solid nanowire. Glas et al. showed that it is energetically more favorable to form ZB phases when nucleation occurs within the droplet, far from the interface of vapor, liquid and solid phases, position 1 in figure 1.9. The intersection point where the solid nucleus shares an interface both with the liquid and vapor phase is called triple phase line (TPL), position 2 in Figure 1.9 . Most of the time the TPL is energetically the most favorable location for nucleation event to take place. In that case the effect of solid vapor interface on the nucleus supersaturation in the droplet and the surface energy of the droplet determines if WZ or ZB phase is more stable.[74]

This theory holds with respective experimental results of Au assisted GaAs NW growth where the WZ phase is observed under higher supersaturation conditions. However Krogstrup et al. later reports that they observe the formation of ZB phase under high V/III ratio (supposedly high supersaturation), and Yu et al. confirms their theory with their experimental data demonstrating that polytypism of their NWs can be mainly explained by the shift of TPL location in a function of V/III ratio.[102][103]

Recently, Jacobbson et al performed detailed in situ TEM measurements to investigate the phase switch during GaAs NW growth for Au-assisted MOVPE system. They found that the WZ phase preferentially forms at high V/III and ZB at lower ratios in contradiction to the earlier findings mentioned above. They have analyzed the nucleation events which lead to formation of WZ or ZB layers and reported that while WZ layer growth proceeds with a slow step-flow regime, the ZB layer growth occurs too fast to investigate the flow behavior. Additionally, droplet morphology is found to oscillate during growth through the formation of truncated facets at the TPL. The existence of the truncated facets was critical for the formation of the ZB phases. They claim that solid-vapor interface energy is lower for WZ case which makes the nucleation of WZ more favorable at TPL line in the absence of the truncated facets. However when the truncated edge facets are present the nucleation event occurs not at the TPL but at the corner of the facet within the droplet, position 3 in Figure 1.9. In that case the energy of the liquid vapor interface plays no part in the nucleation dynamics and ZB phase is formed. They concluded that growth conditions, in particular V/III ratio, "determine the volume of the droplet and, hence, its aspect ratio h/d and contact angle. The value of the contact angle determines whether an edge facet will be present. The presence or absence of the edge facet determines the nucleation site for a new layer, and the nucleation site determines which phase, WZ or ZB, is most likely to nucleate." It should be noted that in situ TEM experiments are conducted at very low V/III ratios in order to ensure the level of vacuum hence such growth conditions are different than the conventional ones. [101]

Within our experimental parameters for self-catalyzed mechanism, we mostly observe GaAs nanowires with a ZB stem, regions of ZB starts with stacking faults and occasionally a section of WZ before the end when we stop group III flow (under high supersaturation). Realization of WZ nanowires is more challenging with Ga-catalyzed growth method. Earlier we have reported phase switching through the change of th V/III ratio and realization of long WZ segments (up to 1 μm)by abrupt changes of Arsenic flux. [97][104]

Since we do not have the means to measure the supersaturation within the droplet during growth it is not possible to produce quantitative procedures for different growth systems but it is safe to propose that phase engineering can be achieved by controlling the droplet shape/wetting of the droplet, surface energy and the supersaturation. These parameters can be controlled by changing the growth conditions, principally the V/III ratio. It has been demonstrated that it is possible to obtain pure ZB and WZ nanowires by controlling the growth conditions and recently the optical properties of WZ or ZB QDs embedded in pure phase nanowires were investigated. [95][79][105][28]

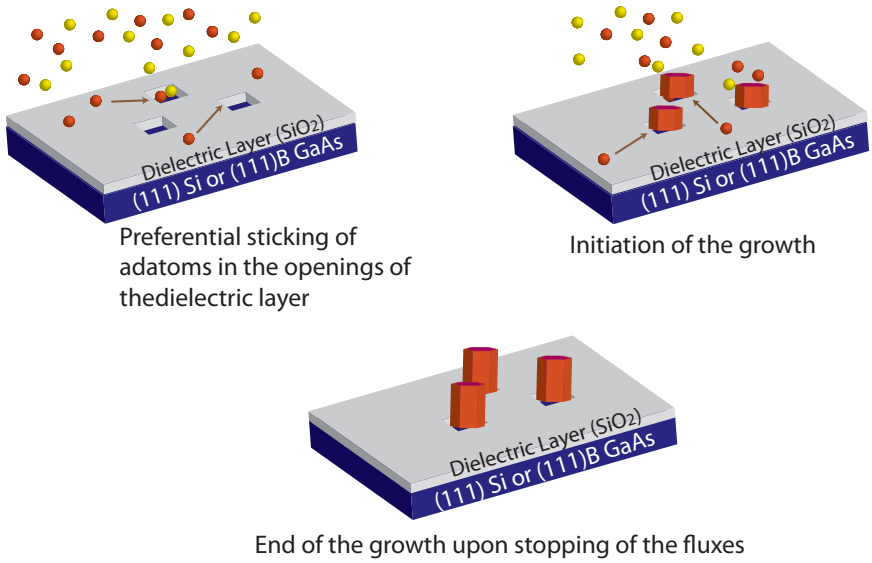

Figure 1.10 – The illustration of the growth of GaAs nanowires on (111) Silicon or GaAs substrates with SAE technique

1.1.2 Selective Area Epitaxy of nanostructures

Selective Area Epitaxy (SAE) is based on preferential sticking of growth precursors on predefined locations of the substrate. Unlike VLS, it does not require a growth catalyst, it consists of purely a vapor-solid (VS) growth. In this sense it corresponds to conventional vapor phase epitaxial growth at a restricted area. To achieve such position controlled growth usually a dielectric layer such as SiO_2 is used as a mask and patterned through a combination of lithography and etching techniques. Growth conditions are adjusted in a way that the sticking coefficient of growth precursors are minimized on the dielectric layer but maximized in the openings.[106][107] A demonstration of the growth mechanism is given in Figure 1.10. Due to the fact that the geometry is predefined through a mask, size of the openings bear utmost importance to determine the final shape of the nanostructure. It has been found that under identical growth conditions it is possible to realize both GaAs tetrahedral crystals and nanowires by only changing the size of the openings on the oxide. [108] However such geometrical features limit the facets that crystal system can adopt hence might make twin formation energetically more favorable. In that technique, phase engineering is shown to be more challenging than VLS because of the lack of droplet. In fact up to date defect-free GaAs or InAs nanowires have not been achieved with vapor solid selective area epitaxy. However, the effect of mask geometry, growth temperature and V/III ratio on the twin density have been determined. [109]

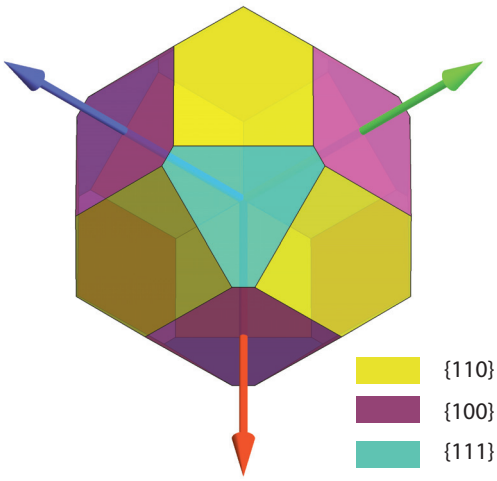

Figure 1.11 – ECS of GaAs pointing out the (111)B direction. Plotted with the Mathematica visualizer for CDF documents prepared by Zucker et al.[62]

Selective area epitaxy of various III-V nanowires have already been realized and seems to be very promising for applications like solar cells and transistors.[10][24] Although from growth point of view selective area epitaxy seems to be more straightforward and compatible with large scale production; the crystalline quality hinders its progress. With this as motivation we have focused on another nanostructure group, namely GaAs nanoscale membranes.

1.1.3 GaAs nanoscale membranes

GaAs Nanoscale membranes are elongated trapezoid crystals bounded by {110} facets. Their growth conditions are similar to the selective area epitaxy of the GaAs nanowires. However there are striking differences like morphology dependence on the growth rate and absence of competitive and independent growth regimes, which will be covered in detail in the next chapter. The main difference from the nanowires is that their mask openings are rectangles with 1:50 ratio oriented in <11-2> or <2-1-1> directions. The orientation is the most important parameter in the growth of nanomembranes because it is forcing the nanostructures to form large {110} facets which have the lowest energy and eliminate the need to form twins in order to lower the free energy of the system.[110][26] This configuration can be better understood by looking at the ECS of GaAs under similar growth conditions of nanomembrane growth that is shown in Figure 1.12. GaAs ECS consists of {100}, {111} and {110} surfaces since they have the lowest surface free energies. According to the calculations of Moll. et al. in As-rich environment, like GaAs nanoscale membrane growth conditions, all four orientations (they consider (111)A and (111)B separately) exist in thermodynamic equilibrium. [111] [26] Sibirev et al. calculates the surface energies of GaAs whisker surfaces based on nearest-neighbor atoms and reports $1.543 J/m^2$ surface energy for (110) which is among the lowest ones with (111). However (111)A and (111)B facets are distinguished.[112] Their surface energy will

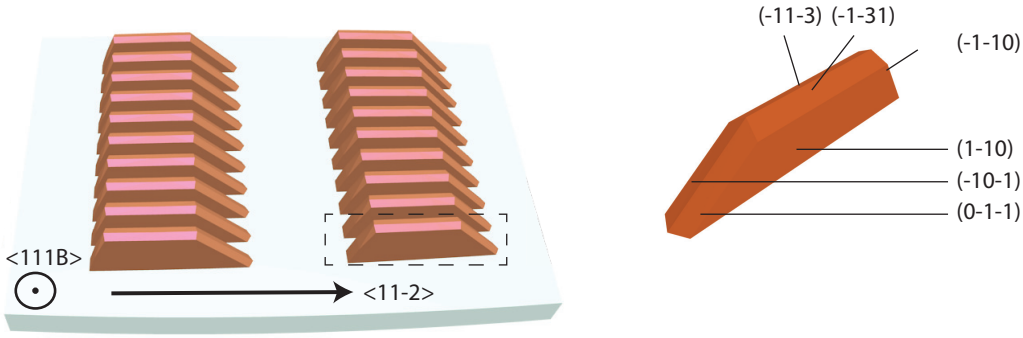

Figure 1.12 – GaAs nanoscale membrane array and the faceting of an individual nanostructure

change in a great extent depending on the growth conditions. When ECS crystal is sliced in the direction of <11-2> by taking two parallel {110} surfaces as boundaries it is possible to obtain a very similar shape to GaAs nanomembranes. When we compare this shape with the real geometry of GaAs nanomembranes, as shown in Figure 1.12 we can see that there are two facets which were not included in the calculations of the ECS, since higher index surfaces are expected to be less stable. They are the (113)A top facets. The formation of these facets shows that the growth is not only guided by thermodynamics. Therefore we also need to consider growth kinetics which would be affected by growth conditions, the shape of the openings and the distribution of the membranes in the array. The detailed investigation of the growth mechanism of the nanomembranes will be covered in Chapter 5.

2 New Aspects in the Growth of Nanowires

This chapter focuses on the growth of GaAs nanowires realized on different substrates. At the beginning of my PhD studies, our group already had a vast experience on the growth of GaAs nanowires. We have applied and further improved that knowledge in order to tackle intriguing research questions and meet different application requirements.

GaAs nanowires are obtained with Ga assisted vapour liquid solid (VLS) method. The growth substrate has been chosen to be Si or GaAs depending on the desired final application. Substrate preparation and growth conditions are varied to change the nanowire density and dimensions according to the application as well.

This chapter is divided into three different sections:

- **Self-assisted GaAs nanowire growth on (111)B GaAs substrates**
- **Self-assisted GaAs nanowire growth on (111) Si substrates**
- **Self-assisted GaAs nanowire growth on (100) GaAs substrates: A polarity study**

We start with GaAs nanowires grown on (111)B GaAs substrates. These nanowires are obtained in the frame of lasing and nanomechanical applications. For lasing, nanowire diameters had to be carefully adjusted and tapering had to be reduced as much as possible. This required careful optimization of the nanowire density since for the cases of high nanowire density shadowing of the incoming fluxes would cause tapering. Switching from axial to radial growth through adjustment of the growth conditions is used when further increase of the nanowire diameter was needed. Another parameter we wanted to control was the yield of vertical nanowires since we wanted to avoid the tilted nanowires which would have asymmetric shell growth. We found it more straightforward to control such parameters on GaAs substrates coated with Hydrogen Silsesquioxane (HSQ) converted silicon oxide. The same parameters were crucial for nanomechanical applications as well, though we did not neccessarily cap the GaAs nanowires. In that case another motivation to choose GaAs substrate has been to increase the mechanical quality of the interface between the nanowire and the substrate. For that section, I designed

the growth experiments and performed them. I have engineered the properties of nanowire samples according to the desired applications. The lasing and optomechanics measurements are performed by our collaborators.

Second section is on GaAs nanowire growth on (111) Silicon substrates. This topic is motivated in the perspective of combining existing silicon technology with III-V semiconductors. We have studied both self-assisted and position controlled nanowire growth with different motivations. In addition, self-assisted nanowire growth on (111) Si substrates could be the first step towards realization of low-cost tandem solar cells with existing Si technology. We have specifically looked into the initial phases of the nanowire growth and the role of the oxide layer. We then applied our findings to the position controlled nanowire growth and increased the yield and reproducibility of the nanowire arrays. Position controlled growth is also interesting for PV applications because the arrangement of the nanowires have been shown to be very important for optimizing the efficiency of nanowire based solar cells due to self-concentration and anti-reflection characteristics of the nanowires.[13][10] For that section, I helped Federico Matteini to design and perform the self-assisted nanowire growth experiments. Interested readers may refer to his thesis. [113] The work on position controlled growth was initiated by Eleonora Russo. During the second year of my thesis and we designed the experiments together and I performed the growths.

The last section concentrates on polarity engineering, reversing the polarity of GaAs nanowires from (111)B to (111)A, performed on GaAs nanowires grown on (100) GaAs substrates. We have used (100) substrates as a platform to modify the polarity of the grown nanowires. We have started their investigation following an initial observation of wires grown on (100) GaAs substrates of different orientations exhibiting different luminescence characteristics. In depth characterization revealed that we had both (111)A and (111)B wires on (100) substrates and nanowires growing in (111)A direction were pure zinc-blende while the nanowires growing in (111)B direction presented stacking faults and twin defects. We have engineered the growth parameters to maximize the number of nanowires grown in (111)A direction. For (111)A nanowires I wrote: For that section, I have initiated the work on polarity engineering after realizing that it is possible to obtain nanowires of different polarity. By performing the growths on (100) GaAs substrates and analyzing their optical properties with PL and CL I understood that the properties and nanowire quality were very different. I supervised M. Zamani in his master thesis for the engineering towards the maximization of A-wires. We have designed the experiments together and I performed the TEM studies to clarify the crystal structure of the nanowires. Polarity determination of the nanowires was performed by Jordi Arbiol in Barcelona and David Deiana in Cime, EPFL.

2.1 Self-catalyzed GaAs nanowire growth on (111)B GaAs substrates

As it has been mentioned in the previous chapter Ga-catalyzed VLS mechanism has been first reported in 2008. The growth was realized on (100) and (111)B GaAs substrates covered

with a sputtered $SiO_x (0 < x < 1)$ layer. Since GaAs does not have a stable oxide at VLS growth temperature window, an alternative dielectric layer should be used to initiate gallium droplet formation on the surface. The epitaxial relation of the nanowires with the substrate at the pinholes in the oxide is demonstrated through the growth direction of the nanowires and cross-section TEM studies. In order to ensure such a relation oxide thickness had to be below 30 nm. [114][91] In addition to SiO_x the use of alumina oxide has been reported in the literature. [115]

We have used a SiO_x layer of few nanometers as the dielectric layer for our growth experiments performed on GaAs substrates. The SiO_x layer was obtained by thermal treatment of spin-coated HSQ diluted with methylisobutylketone (MIBK). It is known that HSQ converted SiO_x layer exhibit a porous nature that would facilitate the pinning and nucleation of Ga droplets on the substrate. The duration and the temperature of the thermal treatment helps to control the density and the size of those pores. [116][117]The thickness of the oxide has been shown to be a crucial parameter for the growth of nanowires as well. Several groups among ours reported different optimum thicknesses for each specific oxide type. Matteini et al. and Rieger et al. were the first to demonstrate the nanowire growth using HSQ converted SiO_x on Si(111) and GaAs (111)B substrates. The main advantage of HSQ is the possibility to change the thickness of the SiO_x layer in a straightforward manner by changing the spin-coating rate or concentration of HSQ solution. [93] [118] Substrate preparation starts with etching of GaAs wafers in a 7:1 buffered HF solution in order to remove the native oxide. Afterwards 10 times diluted 2% HSQ:MIBK solution is spincoated on GaAs wafers with 6000 RPM spincoating rate. Annealing is conducted in two steps. The first step is 5 min at 180 °C in order to evaporate the MIBK solvent and last step is 10 min at 300 °C to transform cage structure of HSQ to network type while burning away the carbon and hydrogen in the structure to achieve conversion of SiO_x. We found out that annealing at higher temperatures led to a denser layer and an additional etching step is required to create pinholes on the oxide to realize nanowire growth. When SiO_x layer is prepared with optimized conditions, the thickness is 3.5 nm (±0.5nm) and following the thermal cycle of the growth it is possible to observe the pinholes/pores on the SiO_x layer as is shown in Figure 2.1a. On Figure 2.1b GaAs nanowires grown on HSQ converted SiO_x coated GaAs (111)B substrates have been demonstrated. A considerable amount of parasitic growth can be also observed in the SEM image of Figure 2.1b.

In order to control the nanowire density we have modified GaAs nominal growth rate and growth temperature. A summary of the results is presented in Figure 2.2. X-axis shows the growth temperature and y-axis represents the varying GaAs rate that we deduced from RHEED calibrations. Representative SEM images demonstrate the effect of growth rate and temperature on the density and dimensions of the nanowires. Increasing GaAs growth rate results in an increase of the nanowire density, nanowire radius and parasitic growth. The effect of increasing growth temperature is reversed. We found that the parameters of sample 4 is optimum to grow nanowires with medium density, and less parasitic growth. In fact although we see a clear trend for increasing growth rate and growth temperature, we can still observe some discrepancies. For instance there is a significant difference between the parasitic growth of sample 4 and 5 which is not expected. This situation may arise from the

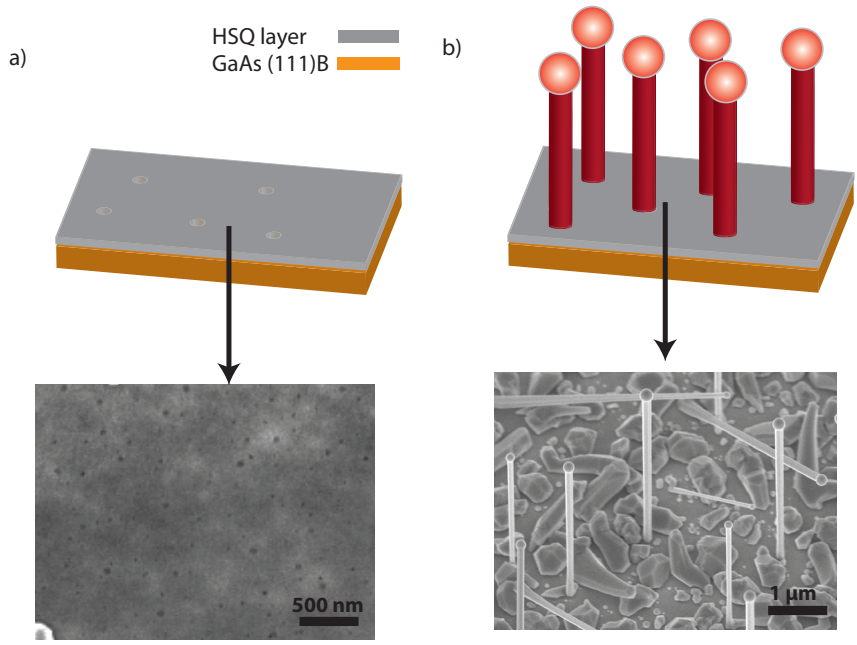

Figure 2.1 – a) Pinholes observed on the HSQ converted SiO_x covered (111)B GaAs substrate after thermal cycle of the growth b) VLS GaAs nanowire growth on such substrates

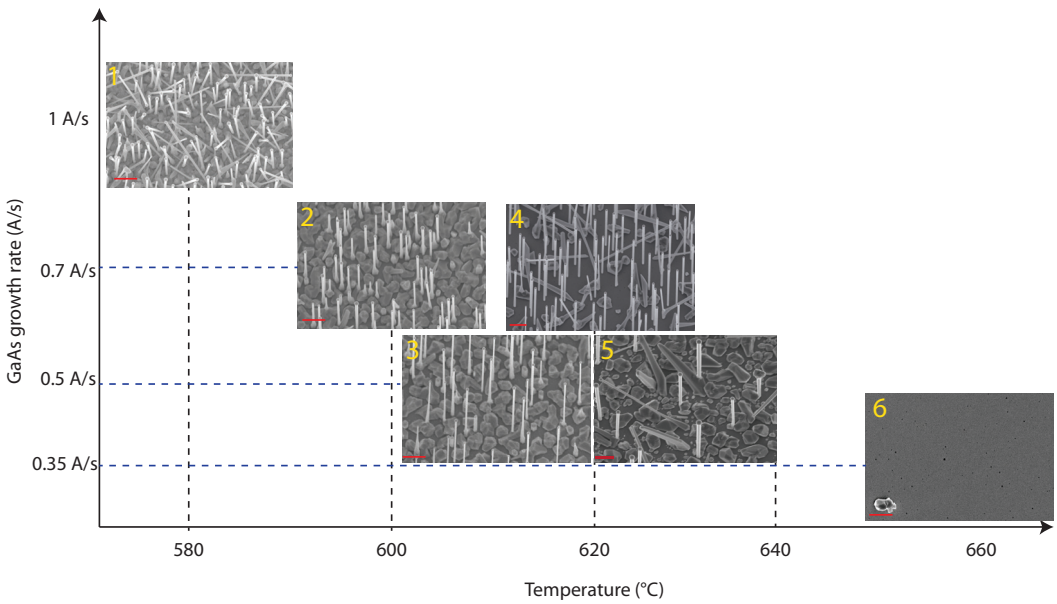

Figure 2.2 – Parameter window for GaAs NWs grown on HSQ covered GaAs (111)B substrates (Scale bar is for 1 1μ)

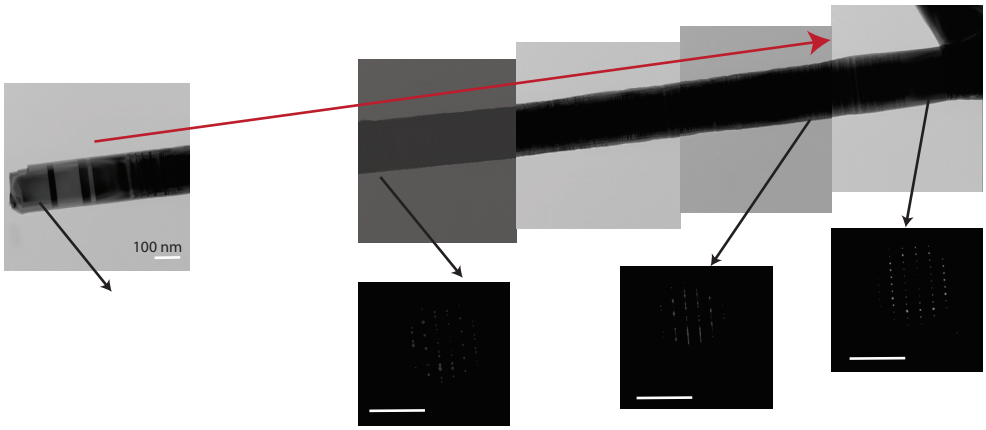

Figure 2.3 – TEM analysis of a GaAs nanowire grown on (111)B GaAs with standard conditions to yield medium nanowire density (0.48 Å at 630 °C and V/III ratio of 24). Red arrow points to growth direction. The root of the nanowire presents ZB structure while the tip is WZ.

substrate preparation. Some batches are found to be more prone to host more parasitic growth. Sample 6 represents the condition where nanowire growth is not possible because Ga adatoms evaporate from the surface before they can nucleate due to low growth rate and high growth temperature.

In conclusion, the substrate temperature should be high enough to minimize the parasitic growth & low enough to avoid complete desorption of the incoming flux. In the optimum range 620-630 °C, Ga rate can be used to control the nanowire density. For next mentioned optomechanics and optoelectronics applications the growth conditions that lead to a medium nanowire density and non-tapered nanowires are used. Figure 2.3 shows the HRTEM and diffraction pattern of a typical nanowire. The crystalline structure of these nanowires were mainly zinc-blende with stacking faults followed by a section of wurtzite close to tip. The change in the crystal structure close to the tip is due to the variation of the conditions when Ga flux is stopped and Ga droplet is being consumed. One could think that during the consumption of the Ga droplet, contact angle varies hence the crystal structure as reported by Jacobsson et al. and Glas et al. [74][101] Growth direction is represented with dark red arrow. Low-magnification TEM images taken from different parts of the nanowire is merged and diffraction patterns taken from the characteristic regions are pointed with arrows. The zinc-blende nature of the base and the wurtzite section at the nanowire tip can be deduced from the diffraction patterns. Rest of the nanowire is dominated by stacking faults as it also shown in the diffraction patterns. Ga-catalysed GaAs nanowires are often reported to exhibit zinc-blende phase with stacking faults. [119]

Nanomechanics:

Mechanical oscillation of self-assisted GaAs nanowires grown on GaAs (111)B substrates are

investigated by our collaborator group in University of Basel with potential applications as scanning probe microscopy probes. We have grown pristine GaAs nanowires with a medium nanowire density with parameters described in the previous section. The length of the nanowires are controlled by the growth time and we avoided any post processing on the wires to avoid deteriorating the Q-factor. In order to ensure the excellent mechanical properties we have grown the GaAs nanowires on GaAs substrates and did not attach them to foreign substrates. The measurement setup is depicted in Figure 2.4. As-grown nanowires are loaded into a setup consisting of a positioning stage for three-axis translation control and adjusted for the chosen nanowire to face a single-mode fiber. The nanowire facets constitute one reflecting interface of a low-finesse Fabry Perot interferometer, while the surface of a cleaved single-mode fiber forms the other interface. A fiber coupler is used to couple light from a laser with a wavelength of 1550 nm into the interferometer. The light reflected by the interferometer is collected by a photodiode. Voltage-controlled piezoelectric transducer (PZT) attached to the sample holder is used to drive oscillatory bending motion of the nanowires along the optical axis of the interferometer. Two perpendicularly placed, voltage-controlled piezoelectric transducers (PZTs) attached to the sample holder are used when it is desired to drive oscillatory motion of the nanowires in two orthogonal directions. In that case two oscillators of a lock-in amplifier independently actuate two PZTs, and the same lock-in amplifier demodulates the response of the photodiode. The oscillator of a lock-in amplifier actuates the PZT and the same lock-in amplifier demodulates the response of the photodiode. A typical nanowire response is shown in Figure 2.4b where the oscillation frequency of the nanowire is plotted against the amplitude. In the inset a nanowire sketch is presented with an SEM image of a vertical nanowire. As it is clearly observed nanowires demonstrate two flexural oscillation modes at 1.194 MHz and 1.2 MHz. These orthogonal modes shown in the inset of Figure 2.4b originate from a slight asymmetry in the nanowire geometry. These modes are shown to couple with each other nonlinearly which makes new applications possible in mechanical logic circuits or in atomic force microscopy. In fact in a follow-up work these nanowires are employed as scanning vectorial force sensors. It is shown that it was possible to map the electostatical forces and force derivatives in 2D by monitoring two orthogonal flexural modes of a GaAs nanowire while scanning over a sample surface. [120][121]

This works shows that nanowires can be used effectively as sensitive scanning vectorial force sensors. Their two orthogonal flexural modes enable us to map the forces and force derivatives in 2D when nanowires are scanned over a surface.

Nanowire lasers

Semiconductor nanowires are known to be promising for lasers since they provide both the cavity and the gain medium required thanks to their elongated geometry. There are several works in the literature demonstrating room temperature lasing of both lying and standing GaAs nanowires with continuous wave or pulsed excitation. [20][21][18] GaAs is an adequate material for lasing due to its bandgap at near-infrared range. However unpassivated GaAs nanowires are known to exhibit very low radiative efficiency due to their high surface

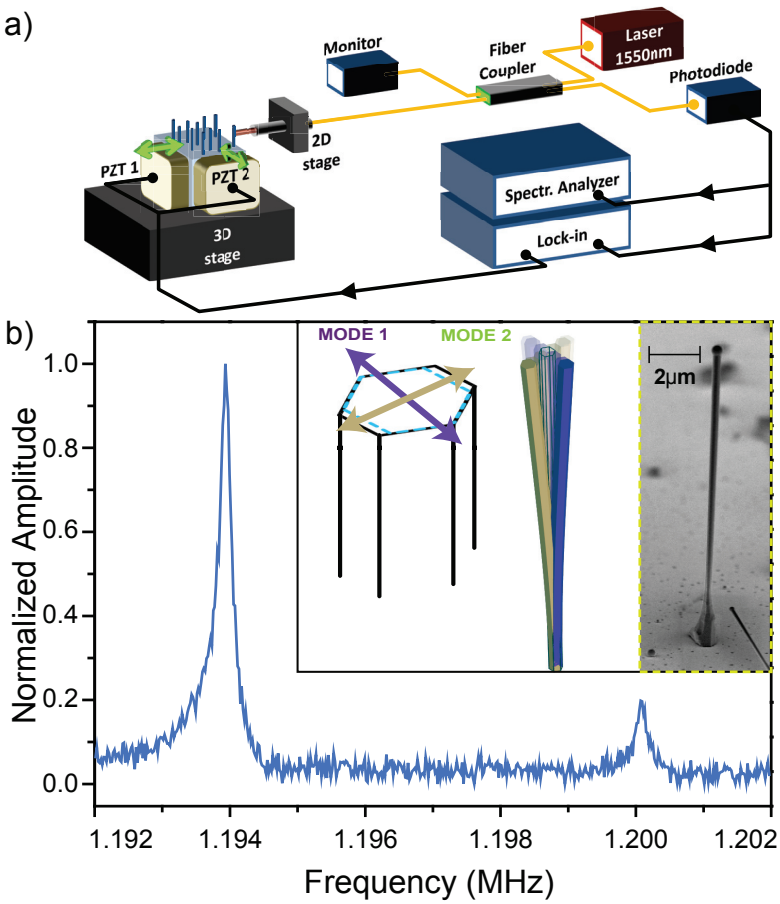

Figure 2.4 – a) Demonstration of the setup for optomechanic properties of nanowires b) The amplitude of the oscillation of the nanowire vs frequency (adapted from [122])

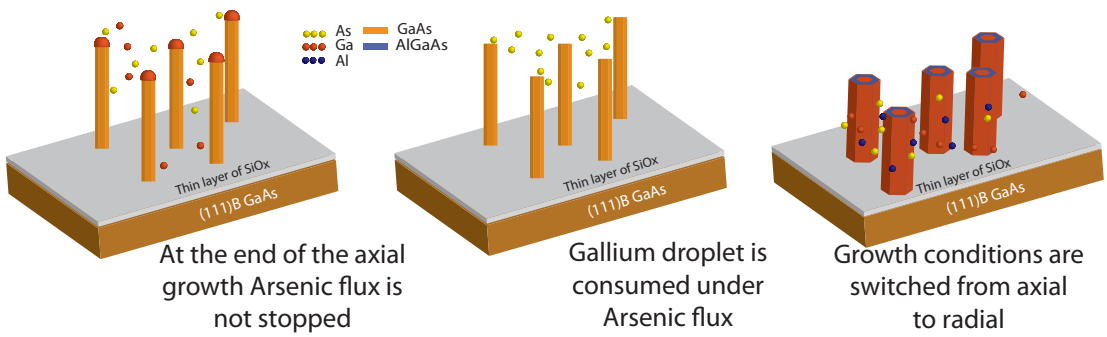

Figure 2.5 – Illustration of the core/shell GaAs/AlGaAs nanowire growth mechanism and the parameters

recombination rate. [123] GaAs nanowires reported in lasing applications are generally surface passivated with a layer of AlGaAs to reduce the rate of surface recombination rates. Recently, Burgess et al. demonstrated lasing with highly doped GaAs nanowires by reducing the rate of radiative recombination as an alternative strategy. [15]

The final aim is the coupling of lithographically designed V-groove plasmonic waveguides to the AlGaAs passivated GaAs nanowire lasers. This is done with the prospect of creating on-chip nanolasers compatible with room temperature operation. We have grown core/shell GaAs/AlGaAs nanowires on HSQ coated GaAs (111)B substrates as described above. In order to reduce tapering and obtain uniform nanowires we have adjusted the nanowire density by adjusting the Ga rate and temperature. For nanowires to lase, round trip gain inside the nanowire must equal the round-trip losses. These two parameters are strong function of nanowire length and the nanowire diameter. Additionally, depending on the nanowire diameter, different modes would be hosted in the nanowire. [17][124] Through diameter engineering nanowire lasers can be designed to lase from a particular guided mode. Tapering would cause nanowires to host different modes at the two ends of the nanowire which would increase the losses. Therefore we have produced samples with a range of diameter while reducing the tapering. VLS growth alone was not sufficient to grow sprarse nanowire arrays with a diameter larger than 150 nm therefore we have proceeded a 2-step growth mechanism as described in Figure 2.5. Upon completion of the core growth, the Gallium droplet is consumed under As flux to achieve a flat (111) top facet. Following that, growth conditions are switched from VLS growth to 2D by reducing the temperature to 460 °C and increasing the V/III ratio. Adjusting the time of the shell growth has enabled us to precisely engineer the overall diameter of the nanowire. A series of samples with a diameter range from 300 nm to 550 nm has been grown with that method. All samples are coated with 20 nm of $Al_{0.25}Ga_{0.75}As$ to passivate the surface and 10 nm of GaAs to avoid oxidization of the AlGaAs layer.

In Figure 2.6, top view and tilted SEM images of GaAs/AlGaAs nanowires of 350 nm diameter are shown. Among all samples produced for lasing, while the average diameter span from 300 nm to 550 nm, the average length is kept constant around 6 μm. Tapering was below 20% and

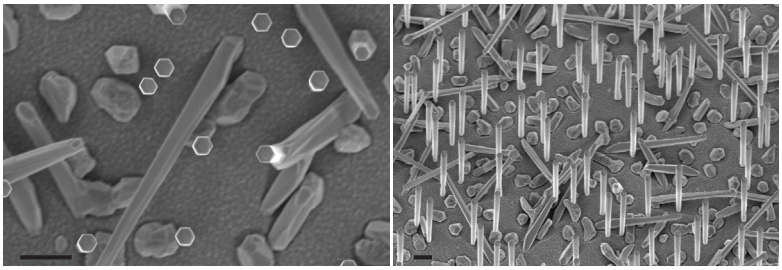

Figure 2.6 – Top view and 20° tilted views of GaAs/AlGaAs core/shell nanowires (The scale bar represents 1 μm)

nanowire density was in the range of $10^{18} cm^{-2}$.

Lasing experiments were performed at ICFO, Spain in the group of Prof. Romain Quidant by Esteban Bermudez. We have observed nanowire lasing and coupling to the V-groove for nanowires thicker than 250 nm in agreement with the threshold diameter reported by Saxena et al for GaAs/AlGaAs nanowires positioned on dielectric layer. [18] In Figure 2.7a, schematic illustration of a nanowire positioned at the bottom of a gold coated V-groove is presented. The nanowire is excited with pulsed illumination and it couples its lasing emission to V-groove, subsequently to free space from the ends of the groove. The SEM image of a real structure is shown in Figure 2.7c. The GaAs/AlGaAs/GaAs nanowire is positioned in a 30μm long V-groove. The inset depicts an enhanced view to one of the end facets of the nanowire. In Figure 2.7b, the intensity of emission with increasing pump fluence is shown. Nonlinear response of the emission intensity and the kink between the spontaneous and lasing emission ranges are presented. In the inset Electron Multiplying CCD Camera image of the nanowire is shown. The fringes of the lasing nanowire and two bright spots at the sides of the V-groove can be noted. The bright spots correspond the coupling of the nanowire lasing to the ends of the V-groove. The spectrum is collected from the right end of the V-groove in that example.

EM simulations show that the lasing is originated by hybrid modes between plasmonic modes of the gold layer on the V-grooves and the nanowires. Different lasing emission wavelengths are observed for wires with different diameters since hosted modes will change in a function of the diameter.[17] This work paves the way for on-chip optical communicators based on nanolasers.

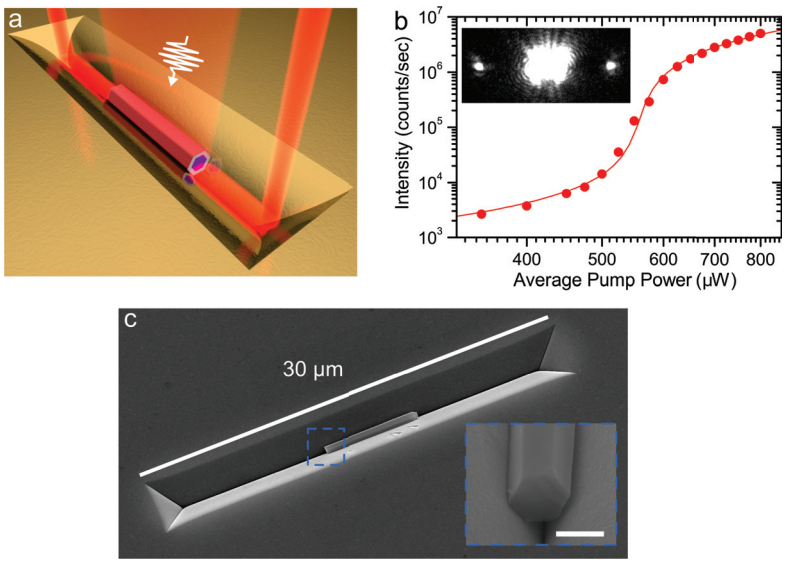

Figure 2.7 – Core/shell nanowires used in lasing application (adapted from Bermudez et al.) (The scale bar represents 1 μm)

2.2 Self-assisted nanowire growth on (111) Silicon

The integration of GaAs to the Si technology is shown to be challenging due to lattice mismatch, difference in crystal structure (polarity) and a large difference in thermal expansion coefficients. GaAs nanowire growth seems to be a feasible method to realize such integration. Reduced contact area and large surface of the nanowires help the relaxation of the strain and the single nucleation event at the interface reduces the possibility of antiphase boundary formation. [70][91][68]

Self-assisted GaAs nanowire growth on the (111) Si substrates could be the first step towards the realization of low-cost tandem solar cells by integration of a NW device on existing Si solar cells. In order to achieve that, one needs to realize the growth of vertical nanowires on Si with high yield. However, it has been shown that vertical GaAs nanowire growth on (111) Si might not be very straightforward since (111) Si surface is nonpolar while GaAs nanowires prefer to grow in (111)B direction under standard growth conditions. Only NWs nucleating with (111)B polarity have the chance of growing perpendicular to the substrate. Three dimensional twinning might cause the growth of non-vertical nanowires. [125] Non-vertical nanowires can be also originated from 2D crystals on the surface, parasitic growth. Apart from that, other parameters that need to be engineered to maximize the light absorption of the nanowire solar cells are nanowire density and dimensions. [126][9]

There are several reports self-catalyzed growth of GaAs nanowires on Si. [127][128][129][102][130][131] Most of them use the native oxide of Si to induce Ga droplet formation but few report the use of thermal SiO_2. [132] We decided to use native oxide due to its simplicity but have experienced reproducibility issues with different batches of (111) Si wafers. In Figure

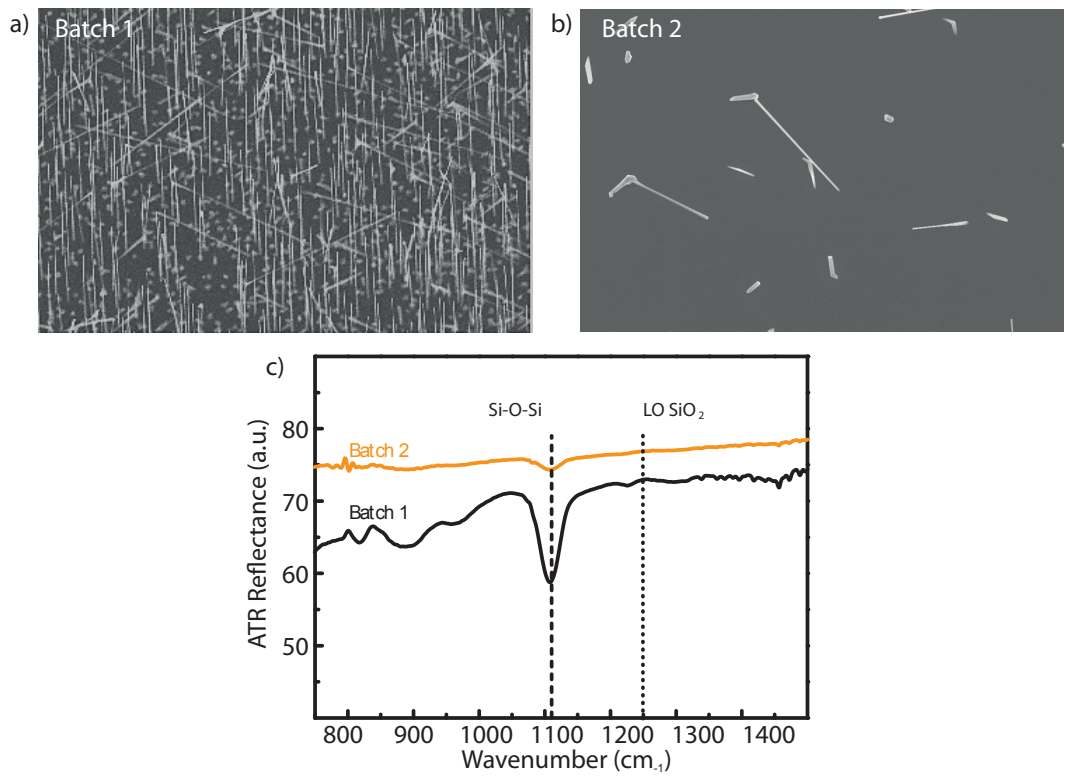

Figure 2.8 – a) GaAs nanowires grown on Batch 2 at 630 °C and V/III of 60 b) GaAs nanowires grown under identical conditions on Batch 1 c) ATR spectra of wafers of Batch 1 and 2 (adapted from [93])

2.8a and Figure 2.8b two growths realized at identical conditions are presented. As it can be clearly observed, in the first image vertical nanowire growth is achieved with high yield while this is not the case for the second one. Those two substrates belonged to different batches supplied by different companies. In order to understand the reason of such striking difference we analyzed two substrates with Attenuated Total Reflectance (ATR) and found out that the phonon mode of interstitial oxide Si-O-Si is more pronounced in the batch which yielded better results. ATR spectra of two substrates are presented in Figure 2.8c.

These findings led us to investigate the effect of the native SiO_x layer more in detail. We have etched Si (111) wafers in HF in order to remove the native oxide layer and let the oxide regrow in constant humidity and temperature. We measured the thickness of the oxide with elipsometry in a regular basis and performed growth under identical conditions on substrates with different oxide layers. The results are shown in Figure 2.9. In Figure 2.9a, time dependent native oxide growth curve is demonstrated. The oxide starts growing with a sharp slope and reaches to a saturation after ≈ 50 days. In Figure 2.9b-f growths performed on different thicknesses of the native oxide layer are shown. It can be seen that the oxide thickness is changing the nanowire morphology and density significantly. We observe only 2D growth below 0.5 nm and the most suitable regime to get vertical nanowires is 0.9-1.1nm range.

We have observed that gallium droplets exhibit different contact angles on oxide layers of different thicknesses. Since wetting is linked to the interfacial energies, we attribute this to the change of the surface energy as a function of the oxide thickness. Measured contact angles are plotted in Figure 2.10a. Colored regions show the growth morphologies obtained on respective range of oxide thicknesses. We have conducted XPS on the substrates as well to characterize the surface composition. Results are presented in Figure 2.10b. It can be seen that Si evolve from SiO to SiO_2 as oxide layer grows towards the saturation thickness of 1.5 nm. Stoichiometric evolution of SiO_x as the oxide layer grows explains the change in the surface energy. We have found that the nature of the oxide layer is a key factor to effect the morphology of the wires. 100% yield vertical nanowires are obtained in conditions when the contact angle of Ga droplets are in the range of 90°. Nanowire arrays optimized with those parameters can be employed in tandem or mechanically stacked solar cells.

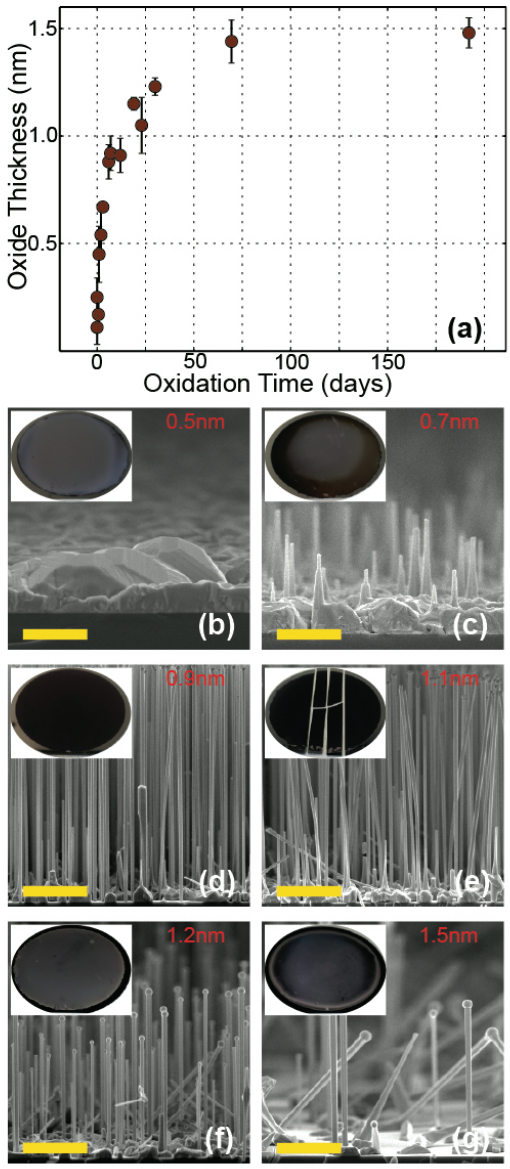

Figure 2.9 – a) Evolution of the thickness of native oxide as a function of time, as measured by ellipsometry. b) Optical images of the wafers after GaAs nanowire growth and corresponding SEM micrographs of the growth performed at 0.5 nm, 0.7 nm, 0.9 nm, 1.1 nm, 1.2 nm and 1.5 nm (Scale bar is 1 μm) (adapted from [133])

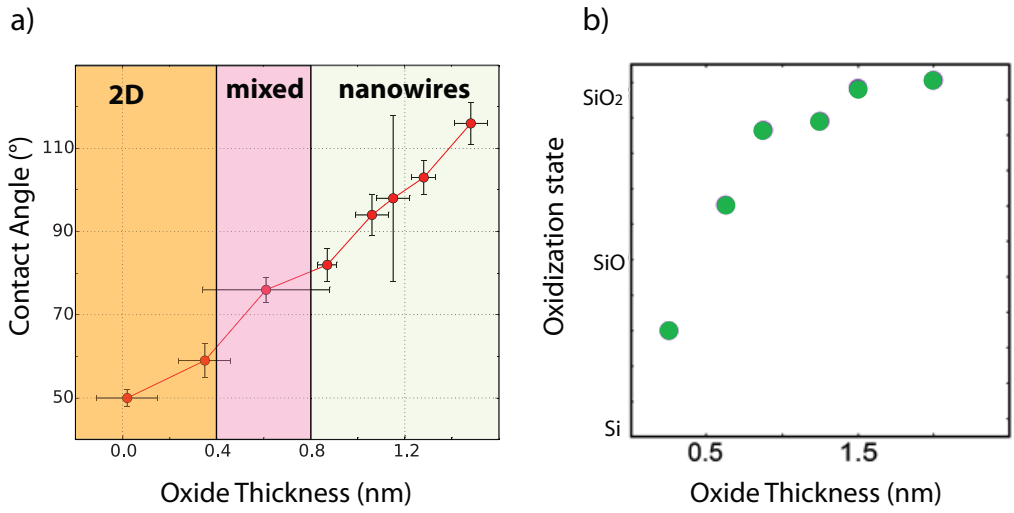

Figure 2.10 – a) The change in contact angle in a function of the oxide thickness b) XPS results reporting the oxidization state of SiO_x vs Oxide thickness (adapted from [134][133])

2.3 Position controlled nanowire growth on (111) Silicon

For some specific applications like vertical transistor arrays or high efficient nanowire array solar cells, it is necessary to precisely control the nanowire dimensions and spatial distribution. Position controlled growth of nanowires is achieved thanks to the available lithography techniques. For instance, the record breaking InP nanowire solar cells have been fabricated by combining nanoimprint lithography and gold layer deposition.[10][1] Several researchers have also used position controlled nanowire arrays to study the growth dynamics of nanowires. They have found that the pitch, the distance between two neighboring nanowires, is very important in the growth process of nanowires. In fact different growth regimes are shown to be dominant depending on the size of the pitch. Nanowires receive adatom fluxes in a variety of ways: direct impingement, diffusion along the sidewalls, diffusion from the substrate and reemission from the neighboring nanowires. Placing the nanowires with a distance smaller than the diffusion length of adatoms on the dielectric layer would cause overlapping of collection areas of neighboring nanowires, competitive regime. In that case nanowires have to compete for incoming group III adatoms. Hence their growth rate increases as they are further separated up to the diffusion length limit. Afterwards, the growth rate remains constant since collection areas of neighboring nanowires become decoupled. This regime of the growth is referred as independent growth regime. [135] Borgstrom et al. reported a regime called synergetic regime for GaP nanowire growth in MOVPE in which nanowires interact with each other to provide more decomposed group III molecules up to a certain distance.[136] In

[1]Current record of the efficiency is 17.8 % held by Technical University of Eindhoven https://steemit.com/science/@whitemike313/efficiency-solar-cells-with-nano-wire-raised-to-17-8

addition to changes in growth dynamics, the pitch also has an effect on the crytal phase. Pitch alters the adatom flux and thus the local value of the V/III ratio.[137]

In order to achieve position controlled GaAs nanowire growth on (111)Si, there are many parameters that need to be controlled spanning from growth conditions to the substrate preparation, the definition of the openings with lithography and etching, cleaning and annealing of the substrates, the thickness of the oxide layer. The highest yield (95%) for GaAs nanowires grown on (111) Silicon substrates has been achieved by Plissard et al. with combination of e-beam lithography and wet etching using SiO_2 as the dielectric layer.[138] By using Gallium pre-deposition technique and optimizing the oxide thickness, researchers managed to position the gallium droplets in the oxide openings before nanowire growth and obtained high yield. We have also confirmed that oxide thickness and pre-deposition are crucial parameters to obtain high yield on GaAs nanowire arrays however there seems to be some reproducibility issues with these experiments which led us to make an in depth analysis of the process.

We have chosen e-beam lithography for our experiments since for us it is the most available technique for defining nanostructures. Since lithography masks are designed with a visual software, it is fast to fabricate new patterns and change lithography parameters in a straightforward manner. Once the conditions are optimized for high yield GaAs nanowire array growths the pattern fabrication method can be changed into a large-scale technique i.e. nanoimprint lithography.

Although we have explored both dry etching and wet etching techniques to transfer e-beam lithography defined openings to the dielectric layer, we have only reported the wet etching results so far. We have prioritized HF wet etching due to its high order selectivity of SiO_2 over Si. The substrate preparation steps are depicted in Figure 2.11. Following e-beam lithography a short O_2 plasma -descum- (10 or 20 seconds of 200 w O_2 plasma) applied on the substrates to remove remaining resists on the developed regions to better define the openings. Afterwards, 12s of wet etching is performed followed by a last O_2 plasma step to remove the resist. Prior to loading the substrates to MBE a last HF dip is performed to clean the native oxide of the openings.

The last HF dip does not only remove the native oxide layer but also determines the final oxide thickness of the SiO_2 layer. We have realized growth on the substrates with 13 nm, 18 nm and 21 nm under identical growth conditions and we have obtained the best results for 18nm of SiO_2 . As it is depicted in Figure 2.12, the oxide thickness has a significant effect on the growth yield of GaAs nanowires. It is important to mention that those results are all obtained on substrates that have been annealed in the growth chamber before growth. 15 min annealing at 770 °C prior to growth is found to be crucial to increase the yield.

After confirming the effect of substrate preparation and pre-growth annealing conditions, we moved on to understand Gallium predeposition parameter as it is reported to be important for high yield nanowire arrays as well.[138] We have performed growth on substrates from different batches labeled as Wafer 1 and Wafer 2. The SEM images of the growths are depicted

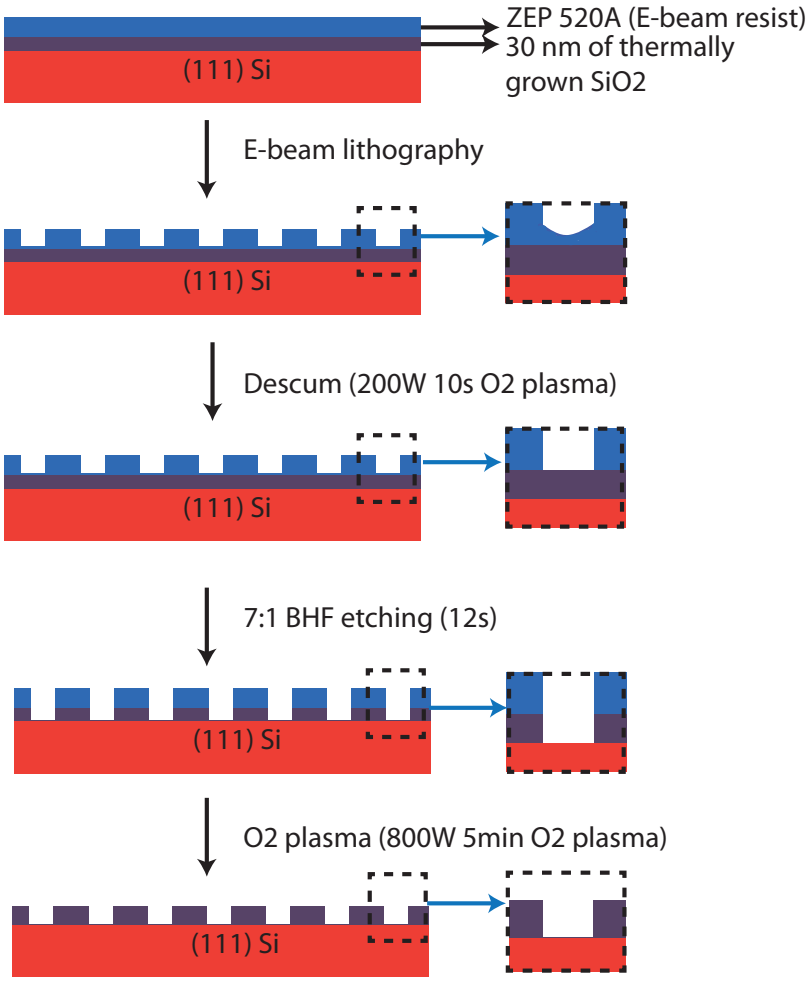

Figure 2.11 – Pattern preparation steps for position controlled growth on thermally oxidized Si(111) substrates

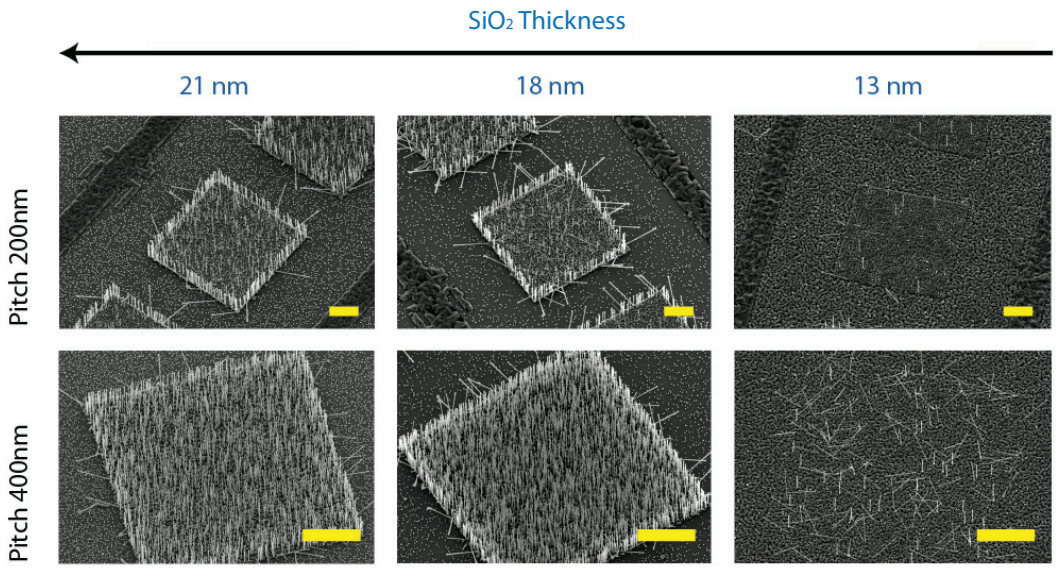

Figure 2.12 – The effect of the oxide thickness on the yield of GaAs nanowire arrays (Scale bar represents 5 μm) (adapted from [126])

in Figure 2.13a. On the left the results with Ga predeposition are shown and on the right the results without Ga predeposition. We found out that for Wafer 1 the step of Ga predeposition was crucial to obtain high yield while this was not the case for Wafer 2. However, for the latter we did not see a reproducible trend and the yield of nanowire array seems to oscillate in a function of unknown parameters. Therefore we prepared FIB lamella from these two substrates and analyzed them with TEM. The results are presented in Figure 2.13b. It can be noticed that Wafer 1 for which deposition of Gallium is necessary to obtain high yield has a layer of a-Si between the crystalline Si layer and SiO_2. This layer disappears after growth. Wafer 2 does not present such an a-Si layer. In the literature a-Si is reported to crystallize at temperature above 500 °C which is lower than our growth temperature of 630 °C. [139][140] So it is reasonable to assume that a-Si crystallizes with an epitaxial relation with the rest of the substrate during the thermal cycle of the growth.

A sketch of the proposed mechanism to obtain high yield in the arrays is shown in Figure 2.14. Substrates have a layer of a-Si at the beginning as we observed in the TEM analysis of Wafer 1. (Step 1) We think Gallium is reacting with a-Si during the thermal treatment and that reaction is pinning Ga droplets to the surface with optimum contact angle. (Step 2-3) As annealing continues a-Si recrystallizes and the nucleation starts, this is why we do not observe any a-Si on the samples after the growth. (Step 4) When we etch away Gallium after a predeposition step and analyze the openings, we observe that Gallium alloys with silicon. Remaining surface is not the smooth and flat Silicon surface, and often we observe a root like feature at the corner, though the distortion in the sketch is exaggarated.

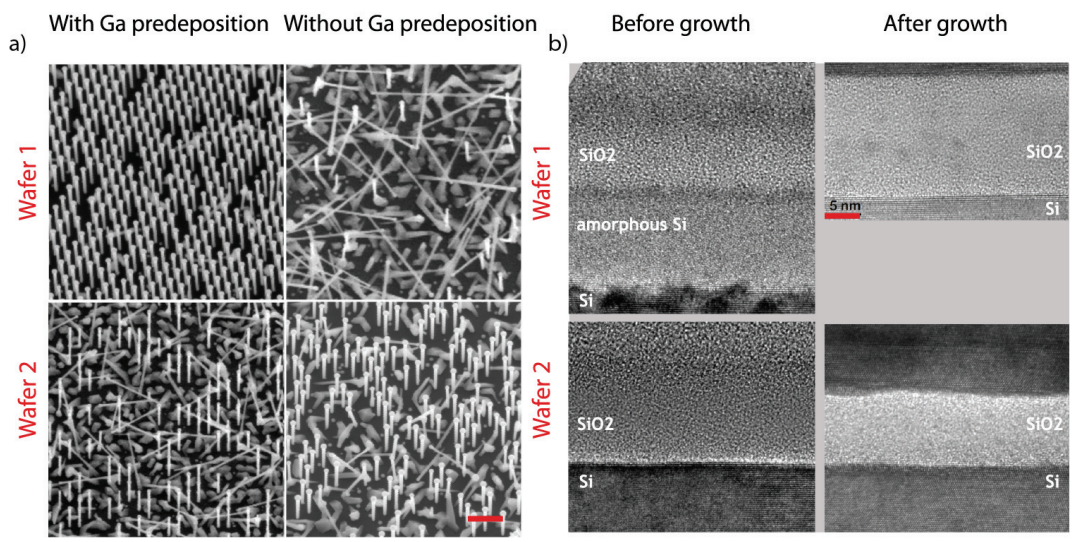

Figure 2.13 – a) The effect of Gallium predeposition (Scale bar represents 1 μm) a) Cross-section TEM analysis of the respective substrates (Scale bar represents 5 nm) (adapted from [141])

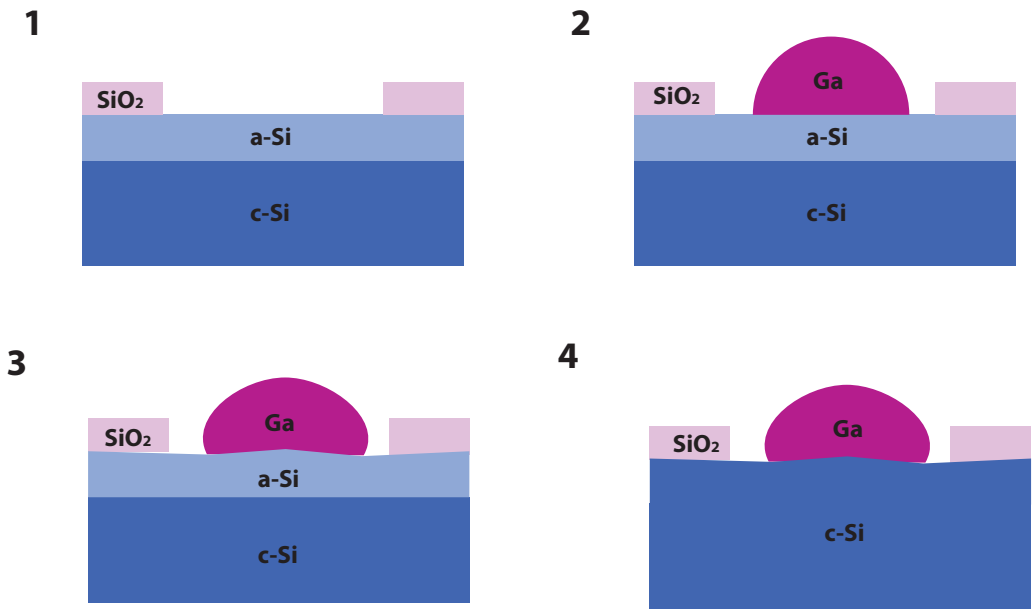

Figure 2.14 – The interaction of Ga droplet with a-Si layer during the initial stages of growth (adapted from [141])

One should note here that, the presence of a-Si layer was not intentional but rather a fabrication error. The company attributed it to a defect in the polishing process. We could not obtain an identical batch anymore. Therefore we looked into alternative ways to pin gallium droplets on the surface with the optimum contact angle to grow vertical nanowires. One strategy we proposed was to re-grow native oxide of 0.9 nm in the openings as mentioned in the self-assembly growth section. This method is shown to be promising as we reported in our publication. [141] The other method is to engineer the aspect ratio of the openings and the size of gallium droplets through predeposition time. In a recent work from our group we showed that one can modify the equilibrium shape of gallium droplets in the openings by engineering the size of the openings and adjusting the volume of the droplet. Although this work targeted the pores in the native oxide of Silicon, it can be extended to lithography defined openings.[134] Reproducible high yield GaAs NW arrays have been obtained with that method.

2.4 Self-assisted GaAs nanowire growth on (100) GaAs substrates: The role of polarity on the crystal phase

GaAs nanowires grown on (111)B GaAs substrates are vertical when they grow in <111> direction and have the B polarity. When growth conditions are not specifically engineered for the sake of phase engineering they usually exhibit polytypism as it has been exemplified in Figure 2.3. Recently A-polar GaAs nanowires grown on (111)A GaAs substrates are demonstrated to be defect-free.[142] In order to create single phase nanowires, we have also decided to take the polarity tuning as a strategy. Our preliminary results had shown that GaAs nanowires we grow on (100) GaAs substrates grow in different directions and exhibit different optical properties. In Figure 2.15 CL characterization of a nanowire assembly on a (100) GaAs substrate and the corresponding secondary electron image are demonstrated. Figure 2.15a depicts the HYP map with assigned wavelengths of 837 nm, 820 nm and 690 nm to red, green and blue. Individual spectra extracted from specific pixels are marked with white squares. Nanowires that emit strongest in the red-labeled range are the majority. We attribute their direction to <111>B. The other group of nanowires look orthogonal to the <111>B wires and demonstrate different emission characteristics. Green labeled ones exhibit very bright free exciton emission while blue labeled ones exhibit strong emission in both free exciton energy and at higher energy range. These findings led us to investigate further the nanowires grow in different orientations or polarities on (100) substrates.

We assumed that different polarities of <111> directions can be distinguished by top-view SEM analysis. In Figure 2.16 we present available <111> directions along which GaAs nanowires can grow on (100) GaAs substrates. When their side view and top-view projections are compared, it becomes clear that they should look orthogonal to each other in top-view SEM images.

We tailored the growth conditions to change the ratio of A/B nanowires. Our results are summarized in Figure 2.17. In Figure 2.17a, the ratio of A nanowires to A+B nanowires is

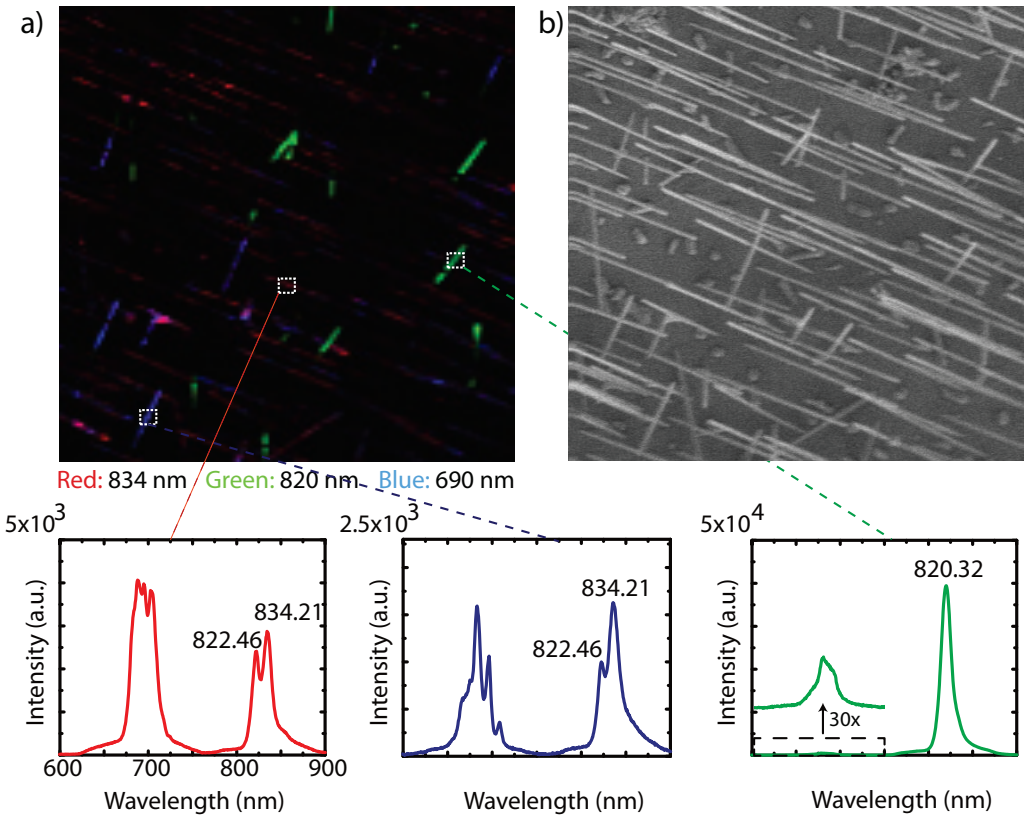

Figure 2.15 – a) CL HYP of GaAs nanowires grown on a (100) GaAs substrate b) Secondary electrom SEM image of the characterized nanowire assemble

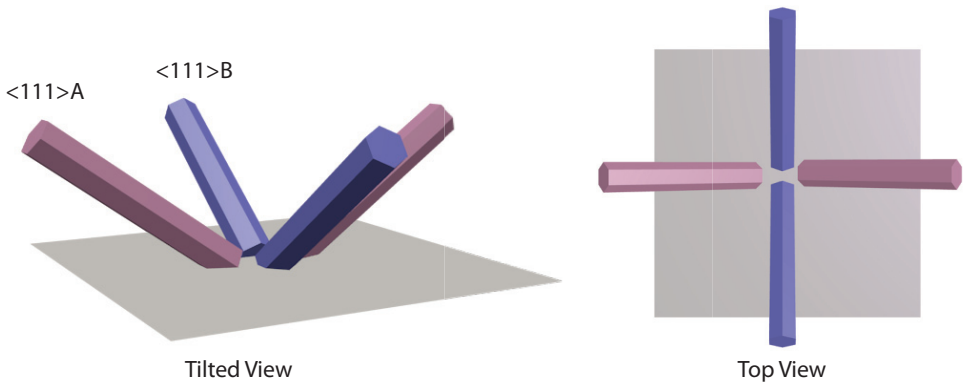

Figure 2.16 – GaAs nanowires in available <111>A and <111>B directions on a (100) GaAs substrate

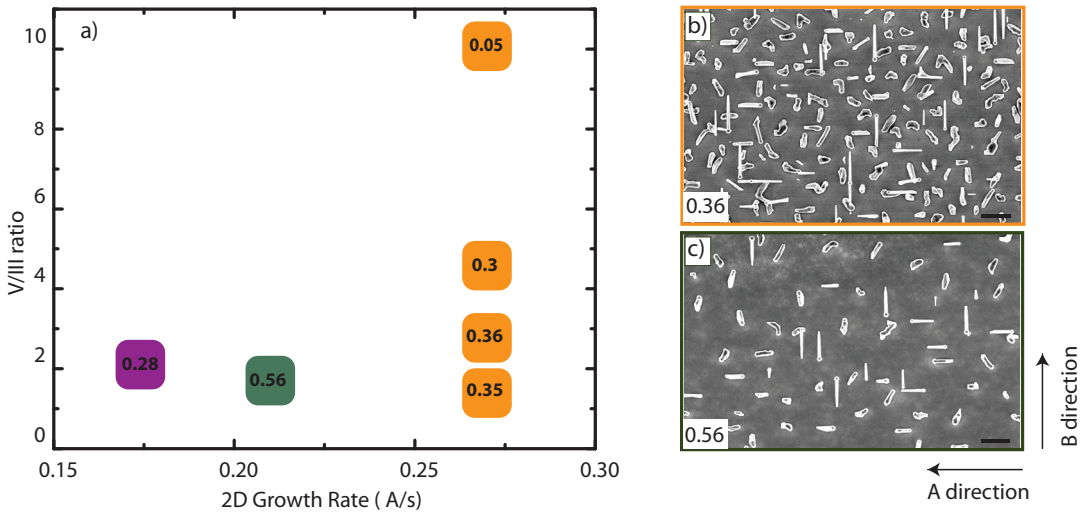

Figure 2.17 – Growth parameters to increase the ratio of A wires. Data points show (A/A+B) ratio b) SEM image the sample growth with 2.5 V/III ratio c) SEM image of the sample with 1.7 V/III ratio which resulted with the highest ratio of A wires (adapted from Zamani et al.)

presented in a function of V/III and growth rate. In Figure 2.17b and c the specific samples with V/III ratios of 0.36 and 0.56 are presented. We have started our analysis by assuming that the majority of the nanowires grown under standard conditions are in B direction since we grow in Arsenic rich conditions. So we defined their direction as B as depicted in the corner of Figure 2.17. Tuning the V/III ratio resulted with a change in the relative ratio of those wires. We have observed that as we decrease the V/III ratio together with the growth rate the number of 'A' wires were increasing. Finally at 1.7 of V/III ratio we found that the number of A wires are higher than the B wires and A/A+B ratio is 0.53. It is depicted that if the growth rate is kept constant as V/III ratio is decreased the number of A-wires increases. The number of A-wires is shown to be increasing as growth conditions diverge from Arsenic rich conditions. We attribute this behavior to the change in the contact angle of the Gallium droplet as a result of the changing V/III ratio. However, a deeper understanding of the initial growth steps is needed.

A closer analysis on the grown samples revealed that A wires have a distinctive morphology which made it easier to distinguish them for TEM analysis. As it is shown in Figure 2.18a and Figure 2.18b-c, their root is wider compared to the rest of the wire. In fact the wires start growing in B direction but change their direction to A after a few monolayers. We are investigating the motivation behind that transition. The diffraction pattern shown in the inset is that from the marked region of the wire and it demonstrates the zinc-blende diffraction pattern taken in (110) zone axis. The entire nanowire is zinc-blende except the base which consists few stacking faults. In Figure 2.18, an atomic resolution HAADF STEM image of the blue framed region is shown and growth direction is pointed with an arrow. HAADF intensity plotted in that direction is plotted in Figure 2.18e and it proves that nanowire analyzed is

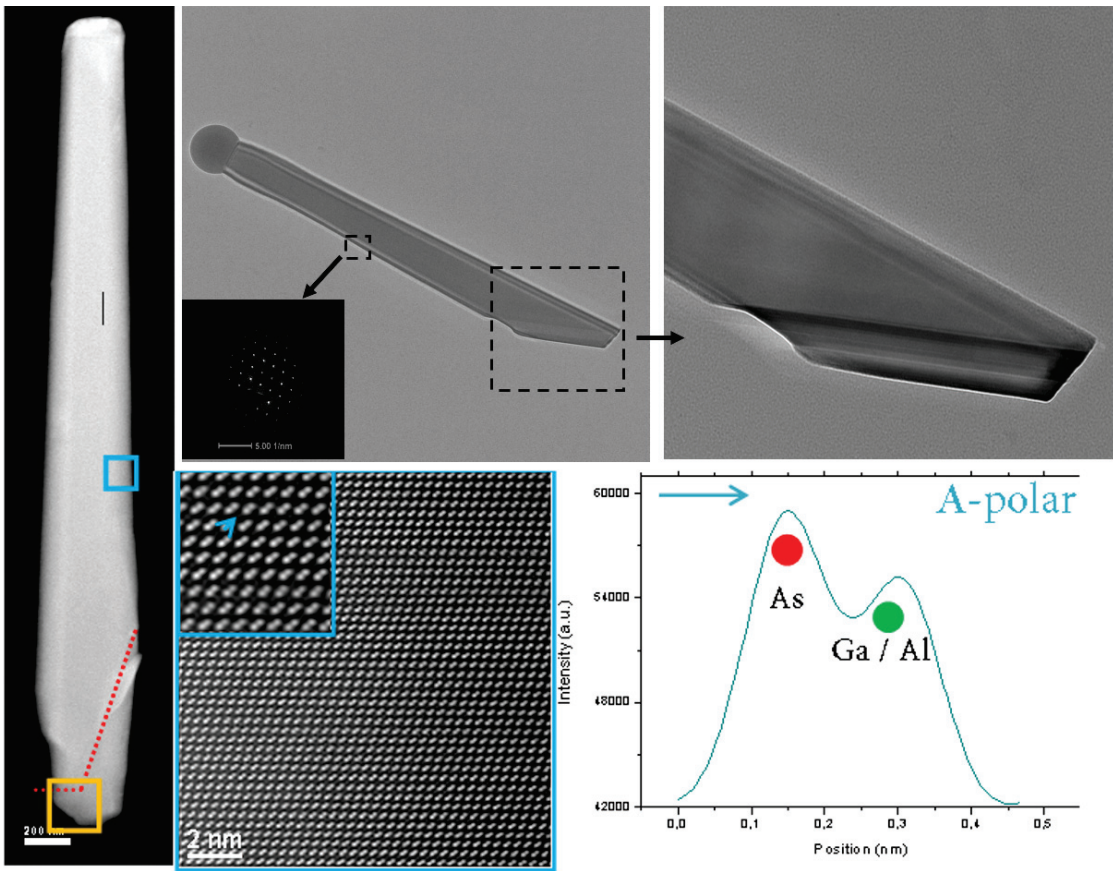

Figure 2.18 – a) HAADF TEM analysis of an A-polarity GaAs nanowire b) Low-magnification BF-TEM micrograph c) Magnification of the root section d) An atomic resolution HAADF STEM image of the blue framed region e) HAADF intensity demonstrating A-polarity (adapted from Zamani et al.)

A-polar.

3 The Growth of GaAs Nanoscale Membranes

In this chapter, a new class of nanostructures, GaAs nanoscale membranes will be introduced. For this, we studied the growth of GaAs on nanoscale longitudinal openings under conditions similar to SAE and optimized them in order to obtain high aspect-ratio structures. Our motivation to study GaAs nanoscale membranes was to 'lock out' the stacking defects by growing elongated nanostructures along certain directions in the form of nanoscale membranes. SAE corresponds to achieving selective epitaxy in localized parts of a wafer. This is usually performed with a mask, the adatoms only adsorbing on the non-masked regions. During 1990s first GaAs SAE growths with MBE are reported by Okamuto et al. and Allegretti et al. [106][143] The process is shown to be challenging with MBE since it is more difficult to evaporate group III atoms from the mask surface. However initial studies point out that by controlling the growth temperature, growth rate and As_4 flux selective growth conditions can be obtained. Additionally, cleanliness of the surface prior to introduction to MBE chamber is always of great importance. High growth temperature is crucial to reduce the sticking coefficient of Ga, hence to prevent deposition on the dielectric layer. But the growth temperature window is not very large because it also decreases the growth rate due to increasing material re-evaporation. The maximum growth temperature reported for SAE on (111)B GaAs substrates is 660 °C.[107] Above that limit surface roughening is observed and high quality epitaxy cannot be obtained. The next parameter to control is the diffusion length of Ga adatoms by GaAs growth rate and As_4 flux. Typical growth rates of SAE are in the order of 0.1-0.15 ML/sec which is lower compared to typical 2D growth rates. As_4 flux is also effective in controlling the diffusion length of Ga since the probability of nucleation events is correlated with the number of available As atoms. Additionally, the As_4 flux is must be high enough to avoid the formation of liquid Ga on the surface. Initial SAE masks consisted of micrometer scaled lines due to the availability of photolithography techniques. Allegretti et al. reported that the grown structures exhibited different faceting depending on the orientation of the substrate and the direction of the line openings.[144] As lithography techniques advanced and the higher resolutions became available, nanoscale SAE growths could be achieved. [145] SAE can also be used to grow localized heterostructures as was shown by Heiss et al. As a consequence, functionality can be obtained in a distributed and organized manner on the growth substrate.[107] Following these

works SAE NW growth attracted attention from both MOCVD and MBE community thanks to the possibility to precisely define the position of the nanostructures with reproducible high yield without requiring a droplet.[132][137] Moreover such a technique would enable us to create axial heterostructures with sharp interfaces through avoiding the limitations of different solubility of the precursors or 'reservoir effect' which is the acting of the liquid droplet as a reservoir of material upon interruption of the fluxes. The main disadvantage of using SAE for the growth of nanowires is the inherent occurrence of stacking defects. Only recently, Yao et al. reported 80 nm of defect-free segments by controlling the growth temperature and the size of the openings by MOCVD. [146] It is considered as a significant improvement compared to the previous work in the field but still more research is needed to enable the synthesis of defect-free SAE GaAs nanowires. Polytypism and stacking faults are an inherent phenomenon in the growth of nanostructures, including nanoparticles, nanowires and nanoscale membranes. The mastering of polytypism, named crystal-phase engineering, has emerged as a way to change the crystal phase in order to modify the functional properties. In the presence of a catalyst droplet, changes in the droplet geometry bear the utmost importance to modify the crystal phase of the nanowire as already mentioned in Chapter 1 . This is because the thermodynamics at the triple-phase line is governing the defect formation such as twin planes and stacking faults. For nanostructures that grow in the absence of the catalyst droplet alternative strategies are needed to realize crystal-phase engineering. As it will be shown in the following, it is possible to avoid stacking defects and polytypism in III-Vs by orienting the SAE openings along an in plane direction.

Orienting nanostructures in specific directions to lock out the defects is a very promising strategy for crystal phase engineering. Orientation dependency of the selective area growth has been already reported by Allegretti et al. in 1995.[106] It has been found out that GaAs lines oriented in <110> and <11-2> directions exhibited different faceting under identical growth conditions, but the crystal structures of the growths have not been reported. Afterwards, Ikejiri et al. and Yoshida et al. found out when GaAs selective area growth is realized in round shaped openings, GaAs crystals adopt the shape of tetrahedra and those tetrahedral GaAs crystals seemed to orient themselves either in <11-2> or <2-1-1> directions. The ones in <11-2> directions are shown to be defect-free for GaAs. [108][109] Recently, Chi et al. reported pure zinc-blende GaAs nanosheets in <11-2> direction grown by MOCVD.[110] This work has inspired us to achieve similar structures with MBE. We have found out that it is possible to obtain the nanomembranes in both <11-2> or <2-1-1> directions. In other directions they exhibit various crystal defects. These nanostructures are attractive due to their interesting growth mechanism that might rule out polytypism and lead to pure zinc blende crystal structure under optimized growth conditions and orientation.

Figure 3.1a shows the SEM image of a typical membrane array obtained under 1Å/s gallium rate in the openings of 10 μm length, 100 nm width and 500 nm pitch. In Figure 3.1b and c, orientation and the arrangement of the array along with the corresponding 3D model of the morphology and faceting are shown. The lateral flat facets correspond to planes of the {110} family, respectively (1-10) and (-110). There are two inclined side facets. The shorter facet is

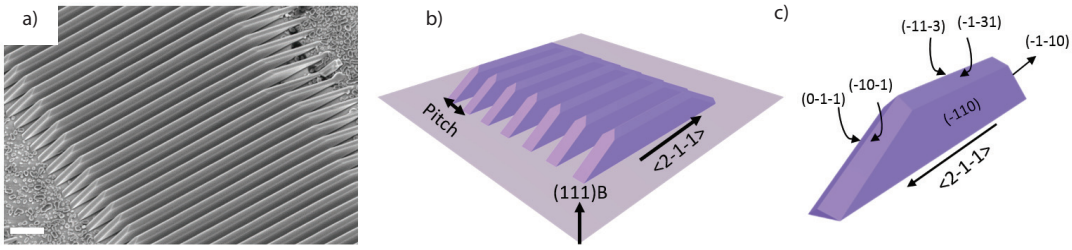

Figure 3.1 – a) an SEM image of the GaAs nanomembrane array b) Array configuration and orientation c) Faceting of a standard nanomembrane grown under 1 Å/s growth rate and V/III ratio of 10 (scale bar is 1 μm)

inclined 35° with respect to the substrate surface. It presents a flat surface corresponding to a (-1-1-0) plane. The longest side facet is inclined 19.5° with respect to the substrate. In this case, this elongated facet is formed by two {110} planes corresponding to (0-11) and (-101) surfaces. Finally, top facets are determined to be (-11-3) and (-1-31) high index facets. The structure evolves into a full triangle and (131) facets diminish if growth is continued. Time evolution is demonstrated in the next sections.

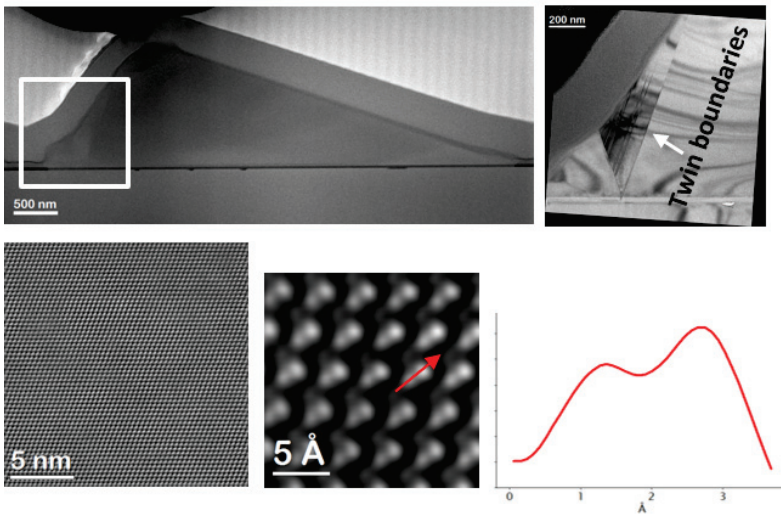

Figure 3.2 – TEM analysis of the membrane. Low magnification micrograph of the membrane cross-section and the magnified region of the defects originated from the substrate. HAADF-STEM image with atomic resolution showing the (111)B polarity of the growth direction

We start by explaining the substrate preparation as well as the optimization of the growth conditions for the growth of GaAs nanomembranes. Afterwards we will provide elements to explain the growth mechanism of such nanostructures through growth time series, pattern modification and annealing experiments.

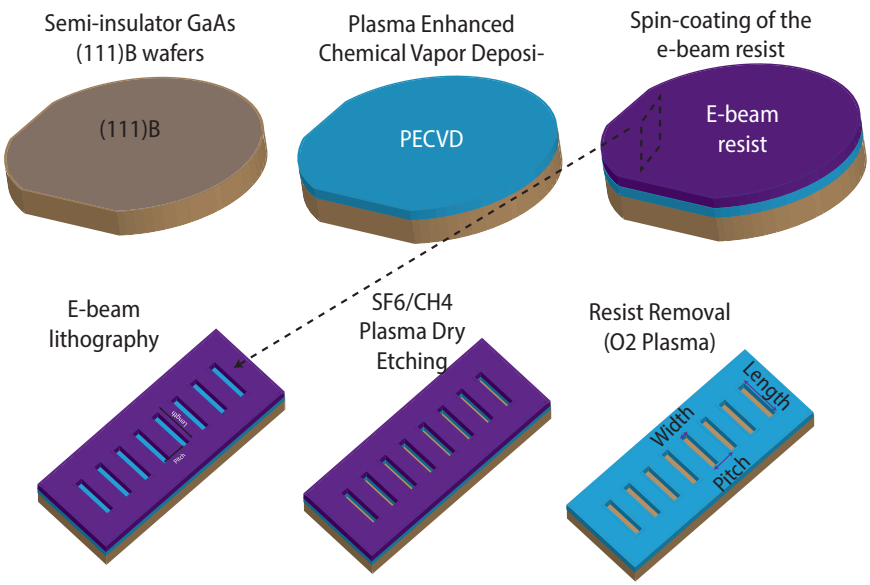

Figure 3.3 – Substrate preparation steps of GaAs nanomembrane substrates

3.1 Substrate Preparation

The first step towards the growth of the GaAs nanomembranes is the substrate preparation. They are schematically shown in Figure 3.3. (111)B GaAs wafers are chosen as the growth substrates. SiO_2 is used as a dielectric mask and it is deposited on (111)B GaAs wafers with Plasma Enhanced Chemical Vapor Deposition (PECVD). The thickness of the oxide was 30(±2) nm as measured by elipsometry. E-beam lithography is used in order to define the growth mask. Longitudunal openings of various sizes (width), pitches, the distance between two openings, and lengths are created on the e-beam mask. After exposure, wafers are developed in metyl isobutyl ketone (MIBK) and rinsed with a solution of MIBK and IPA. After development, the mask on the resist is transferred to the dielectric layer with fluorine based reactive ion etching. A duration of 12-15s with SF_6/CH_4 mixture and 400 W plasma is used. Etched substrates are dipped into a diluted HF solution (10%) depending on the roughness of the slit bottoms. Optimum roughness for good quality membrane growth has found to be around 0.3 nm. The final step of the substrate preparation is the removal of the resist with 5-10 min O_2 plasma of 800 W and cleaning with IPA and acetone.

We have found that the RIE step is key for reproducible substrate preparation. Small fluctuations in the etching rate or the amount of carbon contamination of the chamber changed the roughness significantly. Therefore depending on such parameters, we had to include additional descum steps before and after the step of RIE. To be on the safe side we have not etched the oxide layer completely with RIE but introduced a last step of wet etch after the second descum. Moreover, we altered the duration of the wet etching when optimum roughness was

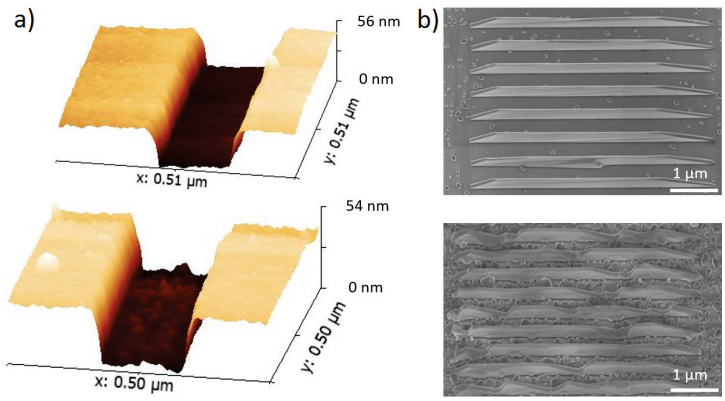

Figure 3.4 – The effect of roughness on the growth of the nanomembranes a) 500nm x 500nm AFM scan of the slits b) Corresponding SEM images of the growths performed on the slits of w/l/p of 50nm/5µm/500nm

not achieved at the end of the preparation steps. In order to make sure that we are growing on standardized substrates we have analyzed one pattern per etching batch with AFM prior to loading.

3.1.1 The effect of the roughness

In Figure 3.4, we elucidate the effect of roughness on the growth of nanoscale membranes. In Figure 3.4a, AFM scans of patterned slits of two substrates are shown. The two were fabricated with the procedure described above. Their roughness is found to be 0.7 nm (top) and 1.71 nm (bottom). In figure 3b SEM images of the respective growths illustrate the different results. The morphology of the membranes is clearly different. The growth on the smooth substrate resulted with the expected membrane structure. No significant defects or several nucleation points are observed. On the contrary, the other sample is not composed of a single elongated membrane morphology, but composed of different heterogeneous features. Additionally, parasitic growth around the membranes (GaAs crystallites on the oxide mask) is also higher. As it will be mentioned later, we have observed a similar morphology for the membranes grown with high V/III ratio and growth rate therefore such a transformation could be related to the reduced diffusion length of gallium as a result of surface roughness.

3.1.2 Dielectric Layer Optimization

We have compared the efficiency of Si_3N_4 and SiO_2 dielectric layers since they are both common selective area growth masks. Both layers are deposited with PECVD, had comparable thickness and exposed to the similar process parameters defined in the substrate preparation section. Etching conditions were slightly modified according to the nature of the dielectric layer. In Figure 3.5 results of the growths performed under identical conditions on two

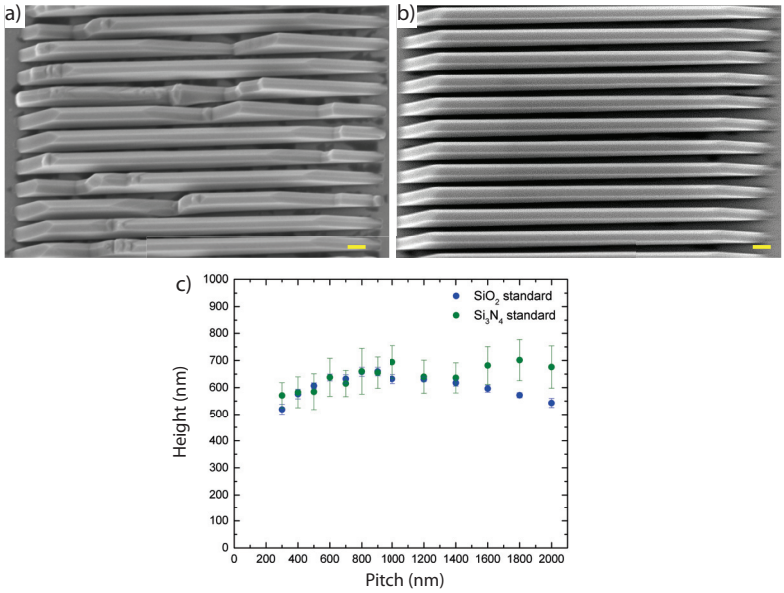

Figure 3.5 – Comparison of SiO_2 and Si_3N_4 dielectric layers as the growth mask a) Growth performed on a substrate with Si_3N_4 mask for w/l/p 100nm/5µm/500nm b) Growth performed on a substrate with SiO_2 mask for w/l/p 100nm/5µm/500nm c) Height vs pitch dependencies of both samples

different dielectric masked substrates are presented. Figure 3.5a includes a SEM image of a nanomembrane array of 100 nm width, 5 μm length and 500 nm pitch grown on the oxide layer masked substrate while Figure 3.5b shows the identical pattern fabricated on the nitride masked one. In Figure 3.5c, height vs pitch dependency of the membrane arrays are outlined. At first glance, one can see that the nanomembranes obtained with SiO_2 as a mask are more uniform and growth proceeded selectively. On contrary, nanomembranes grown on nitride mask exhibit several nodes, indicating different nucleation sites. Moreover, selectivity appears to be poor on Si_3N_4 mask compared to SiO_2. We have observed higher amount of parasitic growth outside of the growth pattern on Si_3N_4 mask compared to SiO_2. This is caused by higher sticking coefficient of Ga atoms on Si_3N_4 layer. It has been also previously reported by Plissard et al. that growth rate of GaAs nanowires grown with silicon nitride mask is observed to be smaller than the oxide masked ones and more parasitic growth is observed.[147] Another possible explanation is that our Si_3N_4 deposition conditions are not as optimized as the SiO_2 and defects are formed on the surface of the dielectric mask which provide additional binding sites to Ga adatoms hence increase the amount of parasitic growth.[148] When we have performed statistics on the pitch dependency of the membrane height on ≈ 20 structures at 2 samples we have observed that the standard deviation in the case of nitride mask is much higher compared to the oxide mask. This is caused by non-uniformity of the nanomembranes grown on the nitride mask. We had not measured the roughness of the slit bottoms for that studies but it is reasonable to assume that such non-uniformity is caused by the larger roughness of the slit bottoms. Such roughness could have been created during the deposition

of the nitride layer or etching conditions we use might not be optimal for the etching of Si_3N_4 although complete filling of the slits shows that slits are properly etched. We have not spent more time to optimize the parameters for the nitride layer since SiO_2 has proven to be a better mask candidate. Lastly, we should mention that on the nitride mask we observe triangular shapes caused by the decomposition of GaAs underneath.Such features were occasionally observed in other SAE growth we performed on GaAs substrates. An example of such triangular features can be observed in the time series Figure 3.18. They appear more often at higher temperatures and lower Arsenic flux environments. We concluded that triangular shapes within the Si_3N_4 layer show that the dielectric layer was not stable enough to protect GaAs layer underneath from decomposition. Following these initial results we have only used SiO_2 for future pattern fabrication.

3.2 Growth Condition Optimization

3.2.1 Growth temperature

As it has been mentioned above, selective area growth requires high temperature and low growth rate to optimize sticking coefficient and diffusion length of Gallium atoms. With the aim of optimizing the growth temperature and decreasing the amount of parasitic growth, we have grown a sample series with varying temperatures from 600 °C to 660 °C. In Figure 3.6 SEM images of the initial growths of varying growth temperatures are demonstrated. The respective growth conditions are given under the images. First growth performed on 600 °C is far from SAE conditions, although we observe some faceted nanostructures there is a lot of parasitic growth on the oxide layer. Increasing the temperature to 615 °C decreases the parasitic growth as shown in the middle image but selectivity is still not fully realized. Finally decreasing the growth rate to 0.3 Å/s and increasing the temperature to 630 °C enable us to restrict the GaAs growth to the longitudinal openings. Later we will show that at that growth temperature we can realize SAE growth at higher growth rates as well. So one of the two requirements of the SAE is no longer a limitation for the growth of GaAs nanomembranes. It should be noted that the orientation of the membranes had not been optimized during these experiments yet.

Overall, we found out that nanomembrane SAE can be achieved in a temperature window between 6525 and 635 °C. For temperatures below 625 °C there was significant parasitic growth dominating the region outside the pattern and the structures were not uniform. For temperatures above 635 °C, it was possible to observe a reduction of the membrane height due to the increasing decomposition rate of GaAs and we could observe GaAs decomposition induced triangular features on the dielectric layer. In addition to these, higher growth temperature causes micro faceting on the side facets of the membranes. In Figure 3.7 such steps are demonstrated. It can be argued that radial growth of GaAs nanomembranes takes place through step-flow mechanism on (110) side facets. At elevated temperatures and correspondingly lower V/III ratios ES barrier becomes more pronounced causing the step bunching on (110) surfaces. Such instabilities on the homoepitaxial growth of (110) GaAs surfaces are reported by Tejedor

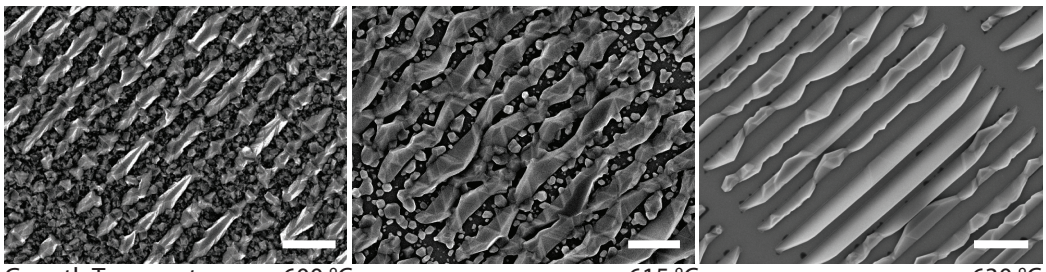

Growth Temperature	600 °C	615 °C	630 °C
Growth Rate	0.5 A/s	0.5 A/s	0.3 A/s

Figure 3.6 – Temperature series to achieve selective area growth of the membranes (The scale is 1 μm)

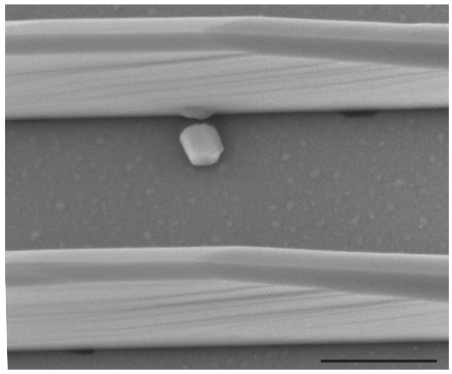

Figure 3.7 – Microfaceting at the side facets of the nanomembranes observed at high growth temperatures (Scale bar is 500 nm)

et al.[66] They have shown that the surface morphology evolution of such surfaces depend in a crucial way on the availability of As on the surface. Such instabilities are not desired since they are supposed to increase the number of surface states and deteriorate electrical and optical properties.

3.2.2 V/III Dependency

Following the optimization of the growth temperature, we investigated the dependency of the morphology of the nanoscale membranes on V/III ratio. We have varied both As_4 flux and Gallium rate by keeping the other one constant to investigate different regimes. The gallium rate was fixed initially to 0.3 Å/s, which was reported to be within the ideal growth rate window for SAE. The As_4 flux was varied between 7.3×10^{-6} and 1×10^{-6} Torr, with the expectation to obtain higher axial rates for a higher arsenic flux. The results are demonstrated in Figure 3.8. Figure 3.8a shows the height of 3 samples as a function of their pitch. For all samples height decreases as pitch increases but there is not a relation between the average height and the V/III ratio. In Figure 3.8b, SEM images of the two samples with V/III ratios of 55 and 37 are presented. As it is shown, we could not observe any trend on the morphology or the axial

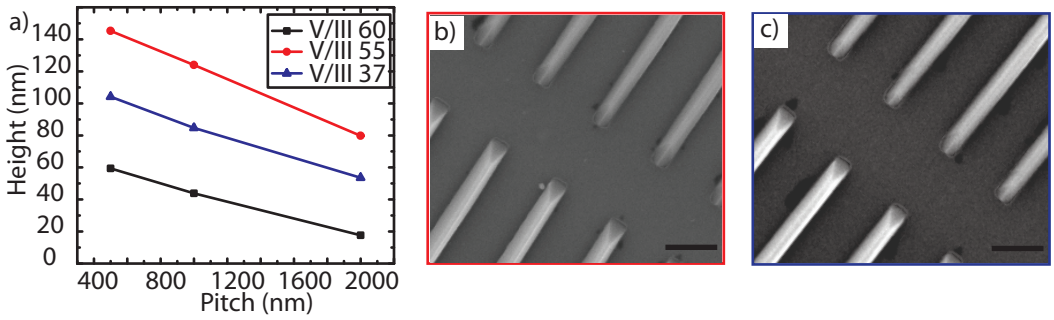

Figure 3.8 – a) Pitch Dependency of the GaAs nanomembrane height in function of V/III ratio which is controlled via changing Arsenic BEP (Beam Equivalent Pressure) by keeping Gallium (Ga) growth rate fixed at 0.3 Å/s b) SEM images of the samples grown with V/III ratio of 55 and 37 (Scale bar is 500 nm)

growth rates in the function of the As_4 flux within the covered the range. Moreover, none of the structures grown under a gallium rate of 0.3 Å/s exhibited vertical {110} sidewalls, their height was around 100 nm, almost equal to the deposited film thickness. A change in the As_4 flux did not make any significant effect on the faceting of the structures. In contrast to the work of Chi et al where they obtain identical structures with MOCVD, vertical {110} sidewalls were not achieved at low V/III ratio by only lowering the arsine flow.[110]

We increased the growth time to observe the change in the morphology of the membranes as growth continues. AFM scans of 1h, 2h and 4h grown samples are shown in Figure 3.9. Increasing the growth time does not facilitate the axial growth. We could not obtain the desired membrane geometry consisting only the large vertical (110) side facets. As growth time increases, structures expand in both directions and we observe a high degree of faceting for 4h sample. It is clear from the AFM analysis that there is a high amount of step bunching on the top facets of the nanomembranes. Next, we reduced the V/III ratio by increasing the gallium rate while keeping the As_4 flux constant. 20 degree tilted SEM images of membranes obtained with different gallium rates for the same growth duration are shown in Figure 3.11. The section of the (-1-10) facet at the edge of the membranes is signified. Vertical side facets seem to develop for gallium rates higher than 0.5 Å/s. The height of the membranes and the relative aspect ratio increases with the gallium rate. This indicates that membrane growth occurs under gallium-limited conditions as for typical planar epitaxy and opposite to catalyst-free nanowire growth.[114] It is interesting to note that the (-1-10) back facet is persistent through all growth conditions while the (1-10) and (-110) facets do not appear in gallium poor conditions. Ideally all {110} family should have the same surface energy, therefore it is not very straightforward to understand such a shape transition. If the Wulff shape of GaAs is constructed only with {110} facets as shown in Figure 3.10, we can distinguish the three

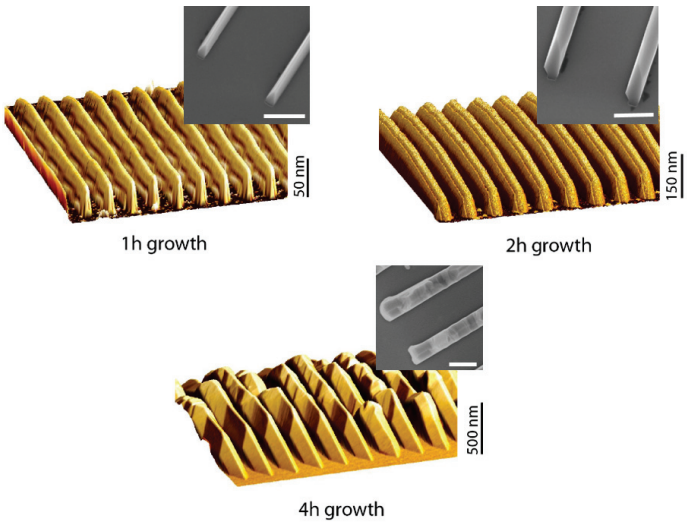

Figure 3.9 – AFM graphs of growth time series with 0.3 Å/s growth rate and corresponding (1-10) facets are shown in the insets (Scales of inset SEM images are 500nm)

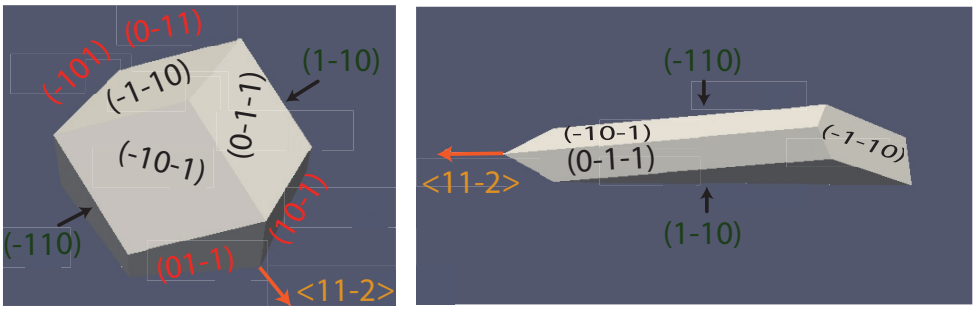

Figure 3.10 – Wulff shape of GaAs constructed by only {110} facets and experimentally obtained membrane geometry

inclined top facets on the top of the crystal. Two vertical side facets are also present. In Figure 3.10b, the nanomembrane geometry that we obtain experimentally is presented. It can be noticed that such a structure can be derived from the Wulff shape by slicing it out along (-110) and (1-10) facets. Only in that case we would need to observe red marked facets demonstrated on the Wulff Crystal as well. The fact that we do not observe those facets indicate the effect of the pattern on the shape of the nanomembranes. The same pattern induced local effect could also cause the diminishing of the vertical (-110) and (0-1-1) facets at gallium poor environment while (-1-10) can still exist.

For vertical sidewalled nanomembranes axial growth rate is almost three times higher than the nominal planar growth rate for the values above 0.5 Å/s. This means there is an increase of a factor 3 in the axial growth rate. Once the vertical {110} side facets are formed arriving gallium adatoms could diffuse to the top facet of the nanomembrane since sticking

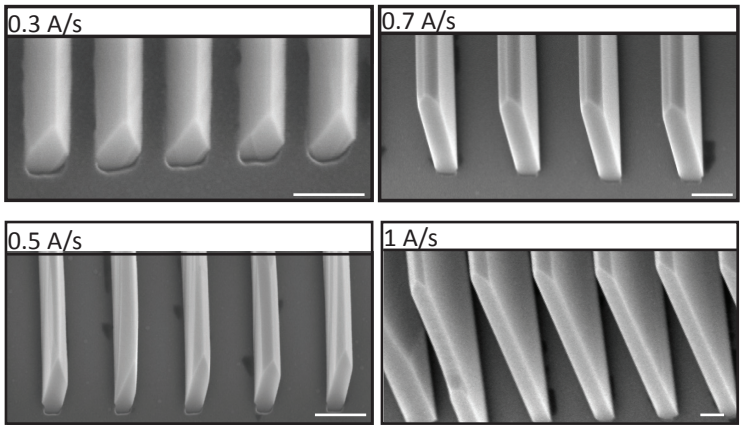

Figure 3.11 – Nanomembranes obtained with different GaAs growth rates with fixed Arsenic pressure (Scale bar is 200 nm)

coefficient of gallium on {110} surfaces are lower than the {113} and {111}B counterparts. [107][149][145]However the radial growth is non-negligible. The width of the membranes is larger than the original 100 nm opening in the mask and the extra radial growth can be also observed in the cross-section TEM analysis that will be shown in the next chapter.

Upon the achievement of vertical side walled membrane structures through optimization of the gallium rate we wanted to look into the effect of As_4 flux for 1.1 Å/s gallium rate, which is the highest gallium rate we have used. The results are depicted in Figure 3.11. SEM images of growth performed with V/III ratios of 28, 19 and 5.2 are shown. It is interesting to observe that As_4 flux window is not very large to obtain the desired membrane geometry. At the extreme of low As_4 flux, nanowires start to appear at the corner where (-1-10) back facet meets the top (113)A facets. In this region we also observe the formation of (111) facet in the absence of the droplet, which should be less stable compared to (110) facets hence more prone to form a gallium droplet in As poor environments. At the extreme of high As_4 flux, nanomembranes are much shorter than expected and we observe a high degree of faceting. The morphology is similar to the nanomembranes grown in rough slits. Therefore, we conclude that factors like roughness or high V/III ratio would limit the diffusion length of gallium and lead to several nucleation sites, like the transition from step-flow growth regime to 2D nucleation regime. As a result, we do not observe a single elongated nanomembrane structure but several isolated crystals in differing orientations.

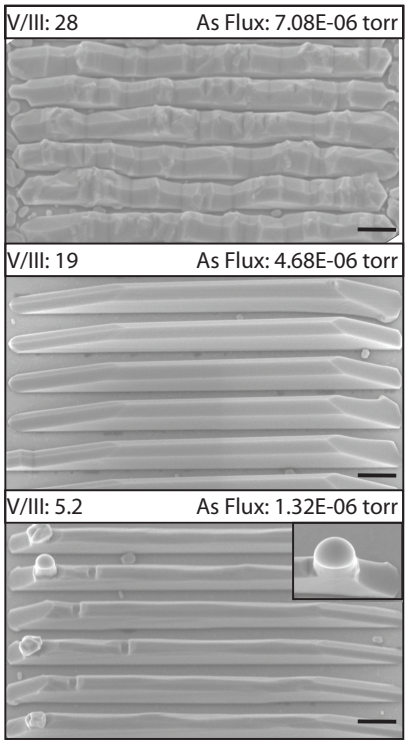

Figure 3.12 – Nanomembranes obtained with different Arsenic fluxes at fixed GaAs growth rate of 1 Å/s

3.3 Growth Dynamics

3.3.1 Pitch Dependency

In order to obtain further insights in the growth mechanisms, we looked at the growth rate of the membranes as a function of the pitch, for different gallium rates, shown in Figure 3.11. As discussed here below, the gallium rate does not only change the faceting but also the growth dynamics. We observe different pitch dependencies for different gallium fluxes. The measured height of the membranes versus the pitch for 0.3 Å/s, 0.7 Å/s and 1 Å/s growth rates are shown in Figure 3.13. The height of the membranes decreases for larger pitches for a gallium rate of 0.3 Å/s. A different trend is observed for higher gallium rates. As we increase the gallium rate, this decreasing trend evolves into two distinctive regimes. Figure 3.13b shows the example for gallium rate of 0.7 Å/s. The growth rate of the membranes increases as a function of the pitch for pitch values between 200 and 700 nm and saturates till a pitch of 1000 nm. This pitch dependence resembles what has been previously observed for InAs, GaP and GaAs nanowire arrays. [136][147][132][137]The increase of the growth rate with the pitch would be consistent with the competitive regime: the distance between the membranes is smaller than the range from which the adatoms contributing to growth are collected. For pitches larger than 1000 nm, the growth rate decreases steadily with the pitch. This seems to be inconsistent with the

competitive regime picture.

In order to understand this trend in greater detail we need to consider the different pathways of gallium adatoms and As_4 that can contribute to growth: direct flux impingement on the membranes, re-adsorption from the substrate, re-adsorption from the neighbouring membranes, surface diffusion through the mask and surface diffusion through the sidewalls. We start by discussing the trend observed at larger pitches for the Ga rate 0.7 Å/s. The decrease in the membrane height for an increasing pitch reveals the loss of adatoms contributing to growth. These can only be re-adsorption of atoms re-emitted from the neighbouring membranes. Another proof of this hypothesis is the fact that nanomembranes at the edges of the pattern are usually shorter than the ones far from the edges. It has been shown that such re-emitted atoms are mainly As_x (x=2 or 4) and not Ga. [150] We therefore argue that re-emission of As_x adatoms is a non-negligible contribution to the growth of the membranes. We turn now to the analysis of the trend observed for pitches shorter than P=700 nm for the Ga rate of 0.7 Å/s. Here, there is a loss of atoms contribution when the pitch is reduced. There could be two origins: shadowing between the membranes which would reduce the incoming flux onto and around the membrane and the distance between membranes is smaller than the Ga adatom diffusion length. It has been shown that the diffusion length of gallium on SiO_2 is around 200 nm at 630°C, shorter than half of the shortest pitch, P = 500 nm. This means that the collection area of the membranes will not overlap with each other. We consider now the effect of shadowing. Since the incoming flux arrives at an angle of 45°, each membrane shadows a distance which is equal to its height, H. This means that for the condition of $P/2 < H \leq P$ shading will be pronounced. For the lowest values of pitch where we see an increasing trend, P is smaller than 700 nm. There is significant shadowing which decreases as the distance between membranes increases. Shadowing will reduce the direct flux impingement on top or side facets depending on the distance. When $P = H$ each membrane completely masks the region with its neighbour. After 700 nm we observe a decreasing trend again because shadowing is no longer pronounced and re-adsorption from the neighbouring side facets diminish as the distance between the membranes would increase.

Surprisingly when we further increase the growth rate we no longer observe the two separate growth regimes of 0.7 Å/s growth rate. Growth rate increases as nanomembranes are more separated and seems to saturate for the largest pitches. That specific growth is performed in a higher temperature window of ±10°C due to an experimental error and higher temperature might have diminished the effect of As_4 reemission. Finally, we discuss the contribution to the growth via surface diffusion from the sidewalls. This should not depend on the distance between the membranes, but only on the length and type of facets. It has been shown that the diffusion length of gallium on GaAs is the lowest on (113)B surfaces, followed by (001),(113)A, (111)B and (111)A. It is the longest for (110) surfaces.[107][149][145]This means that when facets of the {110} are formed, diffusion of gallium adatoms along these facets should not limit the membrane growth rate.

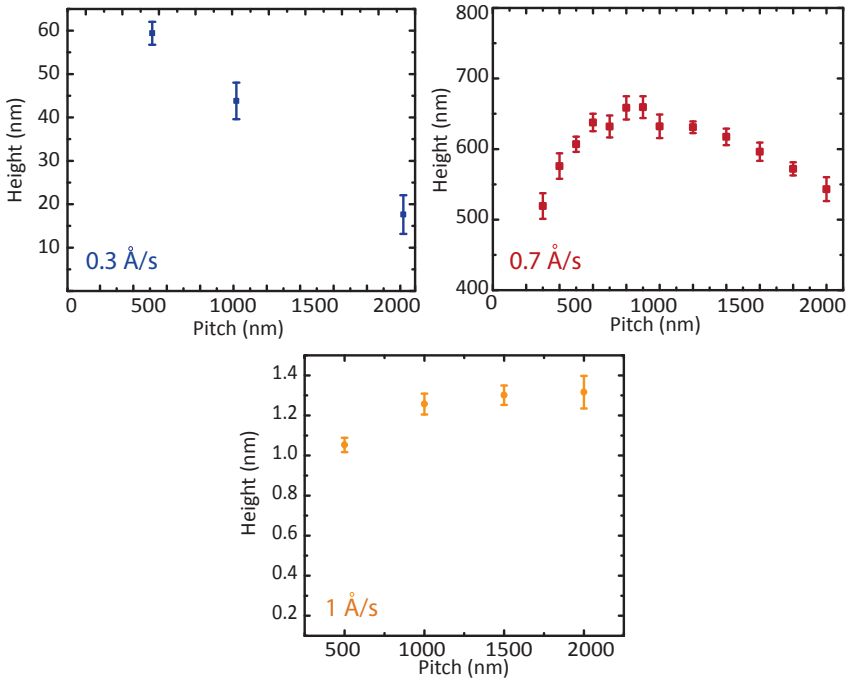

Figure 3.13 – Pitch dependency of the membrane height for different growth rates of 0.3 Å/s, 0.7 Å/s and 1.1 Å/s

3.4 Growth mechanism

Following our initial study on growth dynamics we wanted to deepen our understanding on the growth mechanism. In order to do that, we took different approaches including pattern modifications time series and nucleation experiments on miscut substrates. Pattern modifications included changing the width and the length of the stripe openings as well as realizing growth in round and hexagonal shaped openings. Growth condition modifications included growing time series to investigate the steps of the growth starting from nucleation.

Figure 3.14 presents the growths performed in the hexagon and round shaped openings. The growth conditions were identical with the conditions leading to standard membrane geometry. In order to observe the effect of the opening size and shape we have used 3 different sizes of the hole or hexagon openings ranging from 250 nm to 1 μm m. It can be seen that for 250 nm, the shapes of the crystals that grew in both hexagon and hole openings are very similar. It is a tetrahedron bounded by 3 {110} facets. An in depth analysis of the three axes of the tetrahedral revealed that these structures were either elongated in <11-2> or <2-1-1> directions, which are the directions along which we obtain defect-free GaAs nanomembranes. There is not a striking difference between the morphologies of 250 nm and 500 nm sized openings. Larger tetrahedral crystals adapt the same morphology of the smaller ones. However, we observe some changes for the crystals growing in 1 μm sized openings. Crystals that grow in hexagon openings adapt the hexagonal shape. A small (111)B top facet can be distinguished. Two

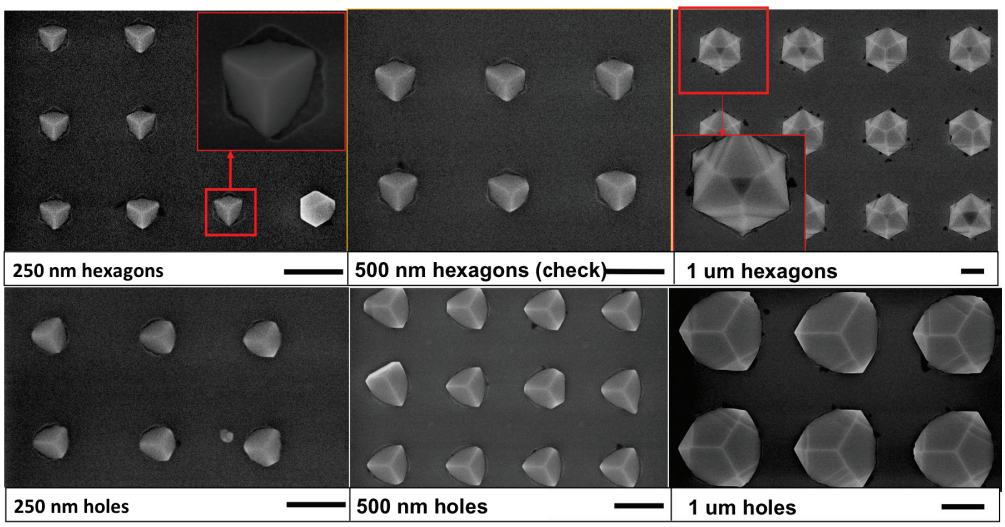

Figure 3.14 – GaAs SAE realized in holes and hexagons grown under identical growth conditions of the nanoscale membranes (Scale bar is 500 nm)

tetrahedra oriented in opposite directions can be resolved from the magnified image at the red framed inset. Therefore, we also show that GaAs SAE growth mechanism is based on rotational twins along the growth direction of (111)B as proposed by Ikejiri et al. and Chi et al. For the growth in round shaped openings we do not observe a hexagon shape but a larger tetrahedron. It seems like radial growth continued at the edges of the structure rather than rotation twin induced axial growth.[108][110] We conclude that for 1 μm m hexagons by restricting the growth on the <11-2> apexes of the tetrahedral at the corners of the hexagon mask we force the structure to form a rotational twin and to continue axial growth. In the case of round shaped openings such restriction is not present therefore growth is continued at the apexes of the tetrahedral. Several twin defects can be observed in the SEM image since <11-2> growth direction is not an energetically favored one.

It has been already observed by Ando et al. that the morphology of GaAs nanostructures grown by SAE alternate between tetrahedral and hexagon nanowires depending on the growth conditions and the size of the mask openings.[109][151] made a detailed analysis of this transition and constructed a phase diagram of such transitions. They report that higher temperatures and arsine fluxes favor the formation of tetrahedral structures while lower temperature and moderate arsine fluxes induce hexagonal nanowire growth. It can be concluded that since (111)B facets is not as stable as {110} facets under non-equilibrium conditions they quickly diminish resulting with the tetrahedral shape but in more forgiving conditions the axial nanowire growth can be continued through rotational twins in the (111)B direction.

To further elaborate on the growth of GaAs nanomembranes we have changed the length of the stripes. Due to geometrical constraints, membrane height is eventually determined by the length of the openings. The longer the stripe the higher membrane can reach if grown long enough. Changing the length of the stripes provided us with an indirect path to investigate

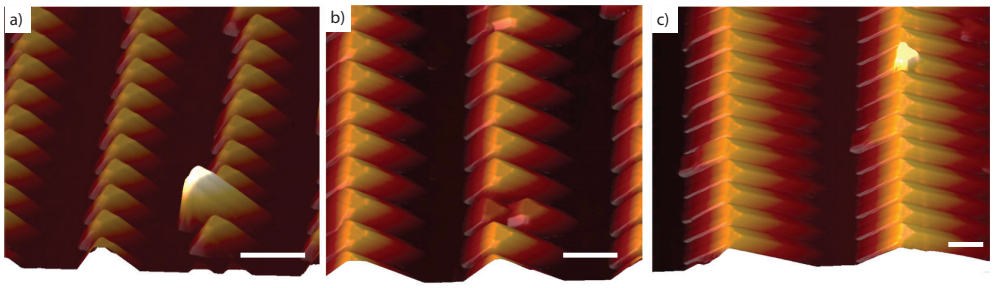

Figure 3.15 – AFM analysis of the membranes grown in different lengths of openings: 500 nm, 1 μm and 2 μm lengths (Scale bar is 500 nm)

the growth evolution. Initially, we have performed AFM on the nanomembranes of with bases of 500 nm, 1μm and 2μm lengths located in different arrays to better analyze the transition from an elongated tetrahedra with a long axis to nanomembrane structure. Results are demonstrated in Figure 3.15. The transition from the tetrahedral shape to the elongated nanomembrane morphology is obvious, while formed facets are identical. As length increases, back (1-10) facet remains in position while the two front {110} facets are elongated in <11-2> direction. In all structures a very small top (111)B facet is still present which means that growth is about to be completed by reaching to the full triangle shape.

In Figure 3.16 part of the membrane pattern is demonstrated which includes stripes of changing lengths from 100 nm to 5 μm. Our purpose with that pattern was to perform a more detailed analysis of the membrane geometry as a function of the stripe length. The growth time is reduced to half compared to the sample demonstrated in Figure 3.11 to better observe the change in the top facet. It can be noticed that membranes reach to full triangle shape only for the shorter openings for those growth conditions.

When the length of the opening is too large that the amount of deposited material is not enough to form the full triangular structure top (113)A facets can be observed. Apart from them, existing facets of the {110} family does not change significantly. Such a transition makes it possible to engineer the shape of the nanomembranes by only modifying the length of the openings. Following these analysis we have performed growth time series experiments to observe the evolution of the membrane morphology during growth. Earlier time series of the growth provided us more insight about the nucleation step of the growth. We have performed 3 min growth with low gallium rate of 0.3 Å/s and maximum gallium rate of 1.1 Å/s on identical patterns. As it is demonstrated in Figure 3.11, 1h growth with such growth rates results with very different nanomembrane morphologies. 0.3 Å/s growth rate leads to short and tilted side faceted nanomembranes while 1 Å/s leads to the complete triangular shape with vertical {110} side facets. We wanted to understand if such a change is related to the initial steps of the growth. SEM images of 3 min growths are demonstrated in Figure 3.17. It can be seen that growth performed with lower growth rate looks smooth while the growth of 1 Å/s has several nuclei in the opening. It can be said that growth is proceeded with step-flow mechanism for

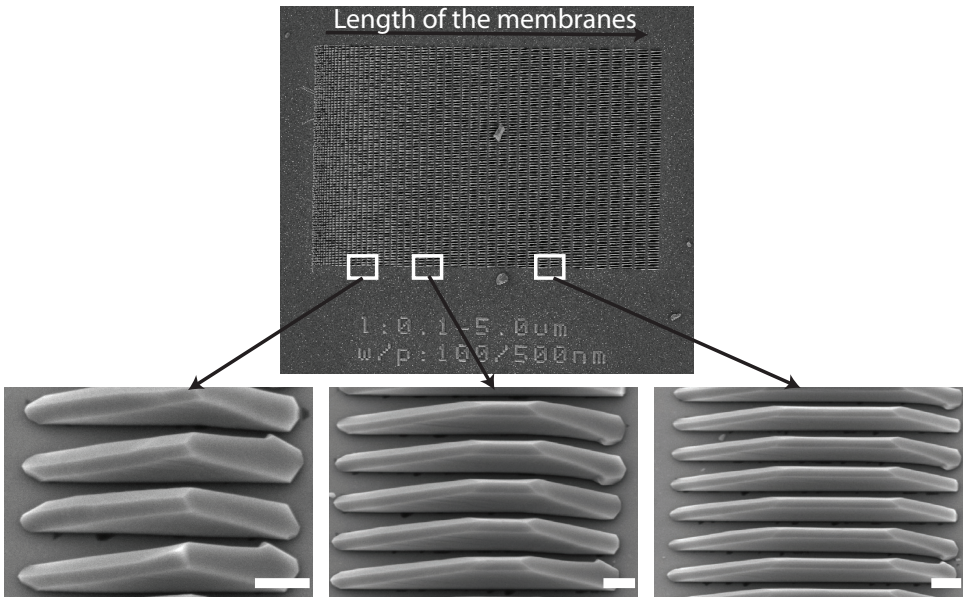

Figure 3.16 – The effect of the length of the opening on the morphology of the nanomembranes (Scale bar is 200 nm)

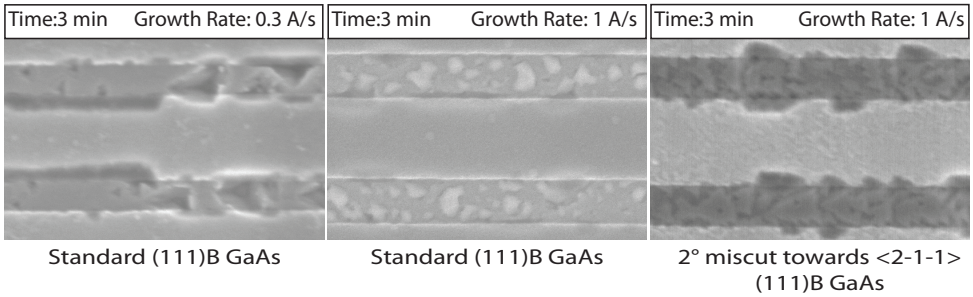

Figure 3.17 – Early time series of GaAs nanomembrane growths from different growth rates and on miscut substrate

lower growth rates while it is switching to 2D nucleation regime as growth rate increases as is mentioned in Chapter 3. If another growth is performed on a (111)B substrate 2 degrees misoriented towards <2-1-1> with identical growth conditions the nuclei can be no longer be observed. Growth resembles step flow like the case of 0.3 Å/s growth rate although the fully grown structure has the same morphology of growth realized on the non-miscut substrate with 1 Å/s growth rate. It can be concluded that once enough atomic steps are provided on the growth substrate growth can initiate in the step flow manner even at higher growth rates. In other words the decrease in the average spacing length of the steps balance the increase in the deposition rate. So Peclet number remains low enough to be in the step-flow growth regime. These findings led us believe that GaAs nanomembranes can be grown on miscut (111) Silicon substrates as well.

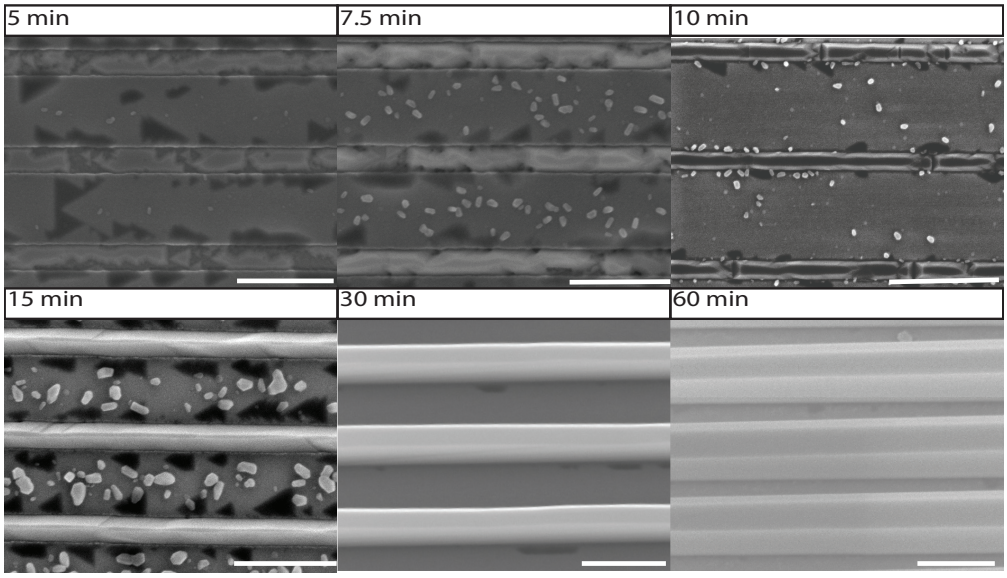

Figure 3.18 – Time series of the growth for 1 Å/s growth rate

Following these findings in order to understand how structures evolve upon leaving the openings we performed time series with growth rate of 1 Å/s. We have observed that triangular features oriented in <11-2> direction already after 5 min. It also looks like such features merge into each other to form a continuous film. Vertical {110} sidewalls do not seem to form within the first 10 min of the growth. Flat (111)B top facet is still present. The morphology does not change much once {110} sidewalls are formed. Top {113} facets appear upon diminishment of (111)B top facet and persist until nanomembrane reaches the full triangular shape. Upon formation of the {110} sidewalls energetically it must be more favorable to form the two (113)A facets instead of keeping the flat (111)B facet. More work on the relative surface energy of {113} facets should be done to better understand such transition which is beyond the scope of this thesis.

Through the experiments towards understanding the growth mechanism of GaAs nanomembranes, we have found that it is possible to modify the shape of the nanomembranes by altering the growth conditions and pattern geometry. Pattern geometry does not change the existing facets but the dimensions of the nanomembrane. Whereas the growth conditions change the relative stability of different facets under corresponding chemical environment so they determine the final shape of the nanomembrane. The nature of the initial growth steps do not seem to affect the final membrane morphology therefore the process seems to be transferable to silicon substrates. In the next chapter GaAs nanomembrane based heterostructures and their optical properties will be mentioned. Their defect-free nature and flexible geometry makes the nanomembranes a promising base for more complicated heterostructures for example self-assembled QDs or 1-D conduction channels.

4 Optical Properties of Nanoscale Membranes & Related Heterostructures

The fabrication of GaAs nanoscale membrane based heterostructures and their optical properties will be covered in this chapter. GaAs is a well-studied and promising semiconductor for optoelectronics. Yet, the efficiency of pure GaAs based devices, especially in nanostructures, is hindered by its high surface recombination velocity (SRV) and this is one of the main drawbacks for future optoelectronic applications. [123] Since GaAs does not have a stable native oxide unlike Si, surface states caused by dangling bonds cannot be saturated with a native oxide layer. Therefore, additional passivation techniques are needed in order to take advantage of the superior optical and electrical properties of GaAs.

The most well-known passivation technique is the growth of a layer of AlGaAs around GaAs. Having a larger band-gap than GaAs, AlGaAs layer confines the carriers into GaAs layer. Additionally lattice mismatch between GaAs an AlAs is on the order of 0.03% so additional strain is minimized in such a heterostructure scheme. [152] Following the interest on GaAs nanowire growth, there has been a vast literature on GaAs/AlGaAs core/shell nanowires. Although initial studies only highlight the role of the AlGaAs shell as the passivation layer, following studies broaden the function of the AlGaAs shell and further functionalize it. Heigold et al and Fontcuberta et al use the type I band alignment of GaAs and AlGaAs layers to introduce quantum wells around GaAs nanowires and create 'prismatic heterostructures'.[33][32] Recently Saxena et al and Stettner et al realized lasers from such quantum well based heterostructures. [16][19] Heiss et al reported that Al poor regions within the AlGaAs shell caused by self-segregation effects act like QDs and further studies are conducted to investigate the properties of such self-assembled QDs embedded in the shell of GaAs/AlGaAs nanowires. [153][25][154]

4.1 Growth of GaAs/AlGaAs heterostructure nanomembranes

Following the examples of nanowire based heterostructures we wanted to also employ the nanomembranes as templates for more advanced heterostructures and their functionality. We have started working on GaAs/AlGaAs heterostructure nanomembranes. The growth of AlGaAs shell is conducted in situ following the growth of the GaAs core. The GaAs nanomembranes are

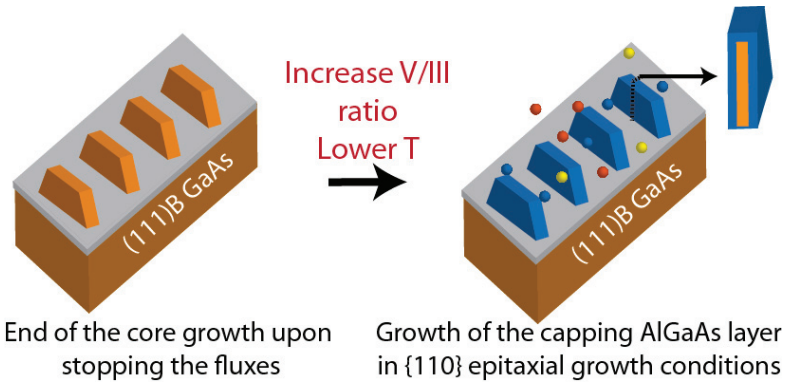

Figure 4.1 – The growth of the AlGaAs shell layer to create GaAs/AlGaAs nanomembrane based heterostructures

limited by mainly {110} facets except the two {113} top facets. Homo-epitaxial growth on (110) surfaces of GaAs has been reported to be more complicated than on (100) case. [155][66] The growth conditions were modified to achieve high quality epitaxial layers on (110) surfaces. For MBE, the best conditions for the growth of AlGaAs shells on the {110} facets of GaAs nanowires are reported as following: reduced growth temperature (630 °C to 450 °C) and increased V/III ratio by maximizing the As_4 flux. [33] Since both VLS grown Ga-catalyzed GaAs nanowires and nanomembranes also exhibit {110} side facets, we have adapted the shell growth conditions of core/shell nanowires to the nanomembranes. The procedure is summarized in Figure 4.1. Following the growth of the GaAs core, growth temperature is reduced to a range of 460 - 550 °C under continuous As_4 flux to prevent desorption of GaAs. The shell growth temperature is found to have a strong impact on the alloy fluctuations in the shell. Once the temperature is stabilized, As_4 flux is maximized to the range of 10^{-5} torr and Gallium and Aluminum shutters are opened simultaneously. The resulting $Al_xGa_{1-x}As$ layer is grown until desired shell thickness is obtained and growth is finalized with a nominal 10 nm thick GaAs layer to avoid the oxidization of the AlGaAs layer.

A typical SEM image of the resulting core/shell nanomembrane array and the corresponding 3D model of an individual membrane is shown in Figure 4.2. The SEM image corresponds to an array with 500 nm pitch. The membranes expand in both directions during the shell growth. If a full triangular shape is reached before the end of the growth, additional triangular features can be observed on the apex of the structures as it can be noted in Figure 4.2a. Such triangular features are formed as a result of rotational twinning once the full triangular shape is reached. This observation has been reported elsewhere.[110][109] Our TEM studies revealed that (1-10) back facet of GaAs membrane transforms into a (-2-2-1) facet during shell growth. The corresponding 3D model of the structure is provided in Figure 4.2b.

Figure 4.3 depicts HAADF-STEM general view of a membrane cross-section. This sample was grown with a shell temperature of 550 °C, 1 Å/s $Al_{0.3}Ga_{0.7}As$ growth rate and 7.6×10^{-6} torrAs_4 flux. It can be seen that the bottom part of the membrane is slightly thinner compared to the

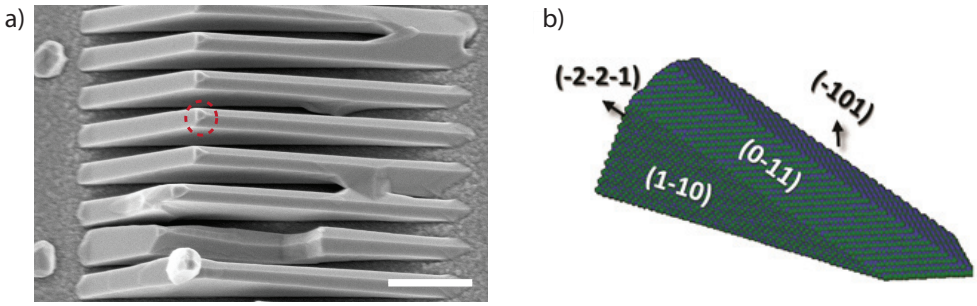

Figure 4.2 – a) SEM image of a GaAs/AlGaAs nanomembrane array b) Morphology of an individual membrane (scale bar is 1 μm) (adapted from [26])

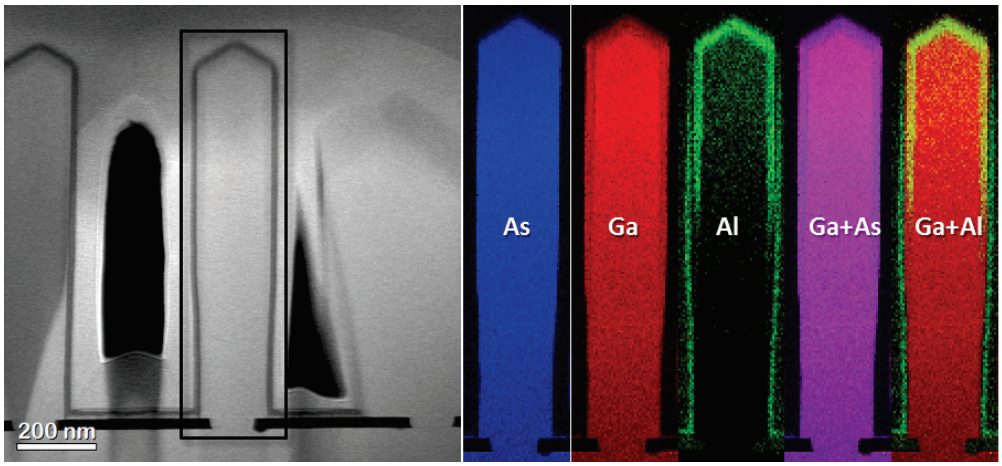

Figure 4.3 – a) HAADF image of a vertical membrane cross-section b) Ga, Al and As EELS maps of the sample

top part and there is radial growth expanding to outside of the pattern opening. We explain the change along the height of the nanomembrane with the pitch induced shadowing effect. Since the pitch is defined as the distance from the start of one membrane to its neighbor, in an array of 500 nm the distance between two membranes opposite side facets would be 400 nm. By taking into account the radial growth, the distance between neighboring facets can be estimated to be around 300 nm. Part of the membrane should be exposed to shadowing effects once the height of the membrane exceeds 300 nm. The neighboring membrane prevents atoms to be directly impinged on the bottom part of the nanomembranes which would lead to thinner AlGaAs shells at the bottom. Such an effect is not expected to be observed for larger pitches. However, we did not observe a change on the passivation of the membranes grown in different pitches during our optical characterization experiments.

A closer look at the HAADF image and the compositional maps of the AlGaAs shell revealed that there are local Al segregation lines within the shell. In Figure 4.4 another HAADF image of an individual membrane and respective EELS mapping is demonstrated. In that analysis the

maps are extracted from a smaller section. Local concentration fluctuations can be visualized very clearly. There are spontaneous Al segregation planes parallel to {110} facets. Such Al segregation creates unintentional QW lines along the facets of the membranes. Similar features have been reported in the literature for AlGaAs shells grown at elevated temperatures due to increasing diffusivity of Aluminum at higher temperatures. [156] We have also grown a GaAs QW sandwiched between to $Al_{0.3}Ga_{0.7}As$ layers we have reduced the growth temperature to 460 °C which is the typical shell growth temperature we use for core/shell GaAs/AlGaAs nanowires on which we can observe self-assembled QDs. We will analyze quantum heterostructures in detail in the next section. Here we only want to investigate the segregation phenomena. We present the dark field HAADF image of a vertical nanomembrane cross-section and relative EDX maps of these samples in Figure 4.5. The GaAs QW can be distinguished with its lower contrast. It is interesting to note that in this case we no longer observe segregation lines in parallel to (110) top facets but only the Al-rich segment in <11-2> direction as commonly observed in ternary nanowire shells. [33] [157]

The Al segregation within the shells of GaAs/AlGaAs core/shell nanowires is an intriguing phenomena. It can be perceived as an imperfection inherent to AlGaAs 3D epitaxial growth or it can be further functionalized to obtain quantum heterostructures such as self-assembled QDs. Local alloy fluctuations within the shells of AlGaAs shells of GaAs nanowires are shown to exhibit QD characteristics. Such fluctuations are strongly correlated with the growth temperature since it is a diffusion process. Recently Francaviglia et al and Loitsch et al demonstrated that the temperature of the shell growth has a great effect on the distribution of the Al on the shell.[158][159] Only by modulating the temperature the level of the quantum confinement can be engineered. Atom probe tomography and TEM studies reveal that at elevated temperatures of 500-600 °C Al segregates in planes parallel to {110} facets. The lowest growth temperature reported that minimizes the segregation is 360 °C.[159] Between those values growth temperature can be used to change the range and the characteristics of the QD emissions originating from Al-poor regions encapsulated within Al segregated envelopes. Our findings are in agreement with these results.

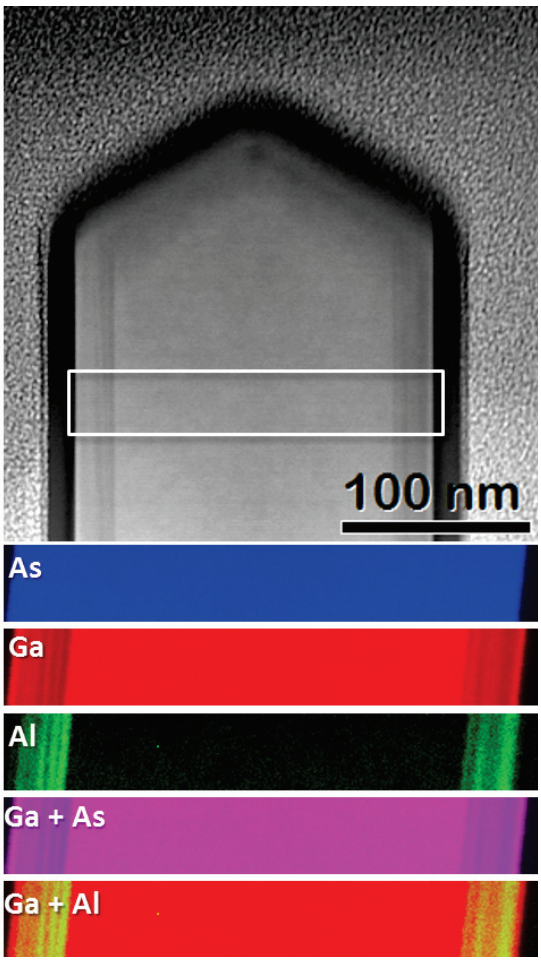

Figure 4.4 – HAADF image of a vertical membrane cross-section and closer EELS maps from the depicted region

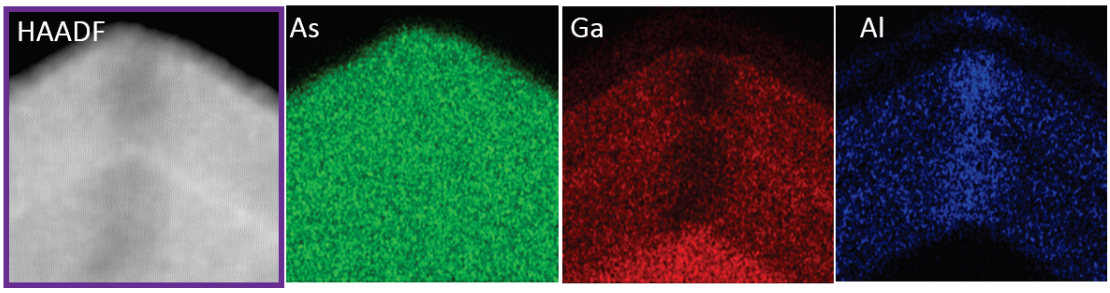

Figure 4.5 – HAADF image of the membrane apex and EDX maps for As, Ga and Al

4.2 Optical Characterization of the core/shell GaAs/AlGaAs nanomembranes

We have characterized the optical properties of the heterostructures by low temperature micro-PL and CL. We start with a nominally 50 nm thick $Al_{0.3}Ga_{0.7}As$ capping GaAs nanomembranes. We have performed low-T micro-PL measurements in our optical setup where samples are excited with a circularly polarized 633 nm red He-Ne laser in a closed loop Helium cryostat, with base temperature of 4K. In Figure 4.6 a representative PL spectrum of a GaAs/$Al_{0.3}Ga_{0.7}As$ structure is presented. In the inset a SEM image of the measured nanomembrane array with 500 nm pitch is given. Considering that the diameter spot of the laser is in the range of 500 nm, we can consider that 2-3 membranes would contribute to the PL signal. We can observe that the spectrum is dominated by excitonic emissions as it has been generally observed for low temperature (<20K) highly crystalline GaAs PL spectra. The sharp peak at 1.5148 eV is the signature of the free exciton emission. Being the strongest emission with such a narrow linewidth of 6 meV demonstrates the high crystalline quality of the nanomembranes. We can also distinguish some features at lower energies. The broader weak peak at 1.4861 eV is the emission characteristic of the free electron carbon acceptor/donor transition. [160] The peak between the carbon related emission peaks and the free exciton is attributed to defect induced bound excitons. Next we have looked at the temperature dependence of the free

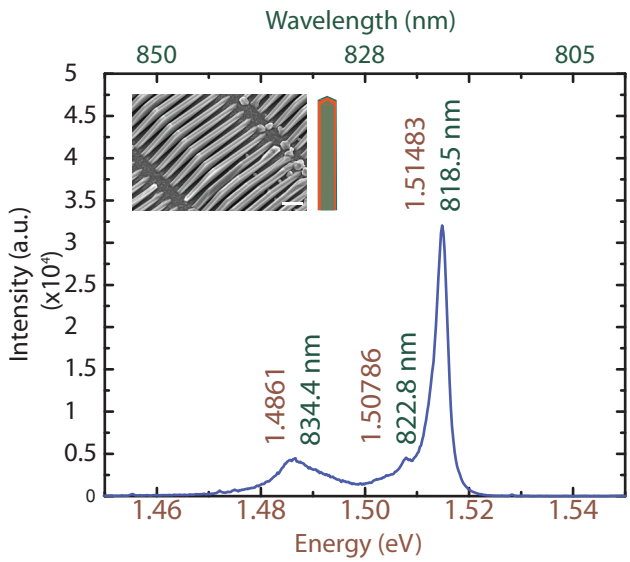

Figure 4.6 – PL spectrum of GaAs/AlGaAs core/shell nanomembrane array

exciton emission. It is known that band gap energy of the semiconductors change significantly as a function of the temperature due to temperature dependent change in the lattice constant (lattice dilation) and electron – phonon interactions. (Varshni, 1967) We have performed the analysis on another GaAs/$Al_{0.33}Ga_{0.67}As$ nanomembrane array in our cathodoluminescence setup. On that sample shell growth conditions were engineered to avoid Aluminum

Eg0 (eV)	$\alpha(10^{-4}eV/K)$	$\beta(K)$	Reference
1.512	5.1	190±182	[162]
1.517	5.5	225±174	[163]
1.522	5.8	300	[164]
1.518	5.4	12	Figure 4.7 (CL-capped)
1.515	6.91	368	Figure 4.7 (PL-capped)
1.517	4.63	164	Figure 4.8 (PL-uncapped)

Table 4.1 – Varshni parameters from the literature in comparison with our experimental data

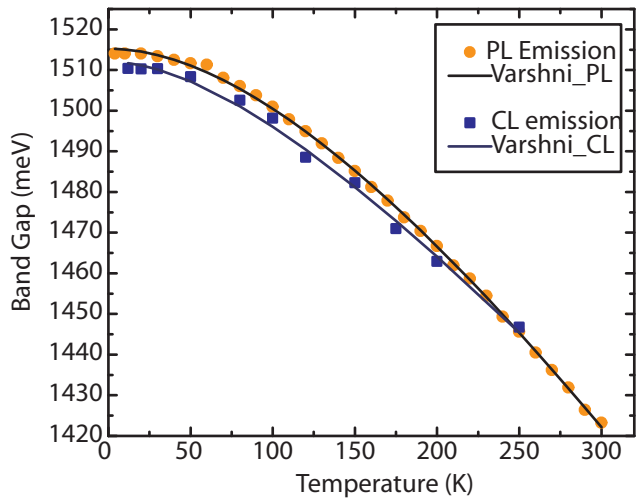

Figure 4.7 – The comparison of temperature dependent PL and CL measurements

segregation along {110} planes. We have fitted the results with Varshni equation ;

$$E_g = E_{g0} - (\alpha T^2)/(\beta + T) \tag{4.1}$$

where E_{g0} is the band gap at 0K, α and β are the material dependent fitting parameters. α is related to phonon interactions and β is related to thermal dilation. [161] Depending on the temperature range and the material the term α effects the behavior quadratically at low and linearly at high temperature. Representative experimental values of the parameters reported in the literature in comparison to our results are summarized in Table I.

Temperature dependent CL spectrum is plotted along with Varshni's equation in Figure 4.7 . Fitting parameters we have obtained were $\alpha = 5.405 \times 10^{-4}$eV/K, $\beta = 12K$ and $E_g(0) = 1.518$eV. At low temperatures the fitting is poor. The Varshni equation is indeed reported to be more accurate at higher temperatures. However, in any case β parameter seems to be inconsistent with the reported values in the literature. The difference might originate from different excitation techniques of cathodoluminescence and photoluminescence, more parallel studies

should be performed in the future. We observed the redshift of the emission as temperature increases as a result of increasing electron phonon interaction. Above 25K, the broadening of the exciton emission is significant. It is reported that above 22K, band to band transitions dominate over the excitonic features in GaAs spectrum. [160]

In parallel to our CL analysis the group of Dr. Paulina Plochocka in CNRS, Toulouse performed temperature dependent PL measurements on capped and uncapped nanomembranes. In Figure 4.7, we compare the temperature dependent CL and PL measurements of the capped samples. We could not present the same comparison for the uncapped samples because it was not possible to extract signal from the uncapped substrate in our CL setup due to known depletion effects and Fermi level pinning on the surface. Varshni fitting parameters for the temperature dependent PL measurement is $Eg(0) = 1,515.24$ eV, $\alpha = 6.91 * 10^{-4}$ eV/K and $\beta = 368K$ being closer to the aforementioned literature values. It is remarkable that CL emission is red shifted compared to the PL emission. while CL data seem to deviate more from the fitting line at elevated temperatures. It is important to note that while PL data is collected from the single spot, CL data here represents the average spectrum of ≈ 10 nanomembranes. Due to band filling effects caused by the higher amount of generated e-h pairs, a blue shift is expected in the CL spectra. However, within the CL measurement parameters we used (up to 5 kV) more electrons are shown to backscatter from the apex of the nanomembrane compared to the bulk of the structure through Casino simulations. Our TEM analysis shows a higher concentration of Aluminum in the apex, so we might observe a more pronounced effect of the AlGaAs shell in CL. More studies are needed to compare the relative shift between CL and PL spectra.

In order to investigate the effect of the AlGaAs shell on the emission of the GaAs nanomembrane in detail, in Figure 4.8 we compare the temperature dependent PL measurements of capped and uncapped samples. GaAs emission is slightly red shifted $\approx 1meV$ in the spectrum of AlGaAs capped sample. They additionally follow slightly different trends as temperature varies. These initial findings point out to the effect of AlGaAs shell on the e-h pair population generated in the GaAs core. It is important to note that for the temperature dependence behavior of the uncapped sample only free exciton peak is taken as a reference. As it will be mentioned next, uncapped GaAs nanomembranes present 3 different types of excitonic transitions as a sign of their superior crystalline quality. For the case of AlGaAs capped nanomembranes a single exciton peak is distinguishable. Temperature dependence of the uncapped nanomembrane spectrum agrees better with the Varshni equation. The deviation of the capped nanomembrane from Varshni at low T points out to the presence of a shell dependent weak localization mechanism. Hocevar et al performed a similar analysis and found a difference of up to 20 meV between uncapped and 35% AlGaAs shell capped nanowires. The difference in our case is 1.5 meV indicating a weaker effect.[165]

Following our initial observation we have performed more in detail studies on uncapped and capped GaAs nanomembranes in collaboration with Zhuo Yang and Dr. Plochocka CNRS, Toulouse. We have analyzed the spectra of individual membranes and the array of mem-

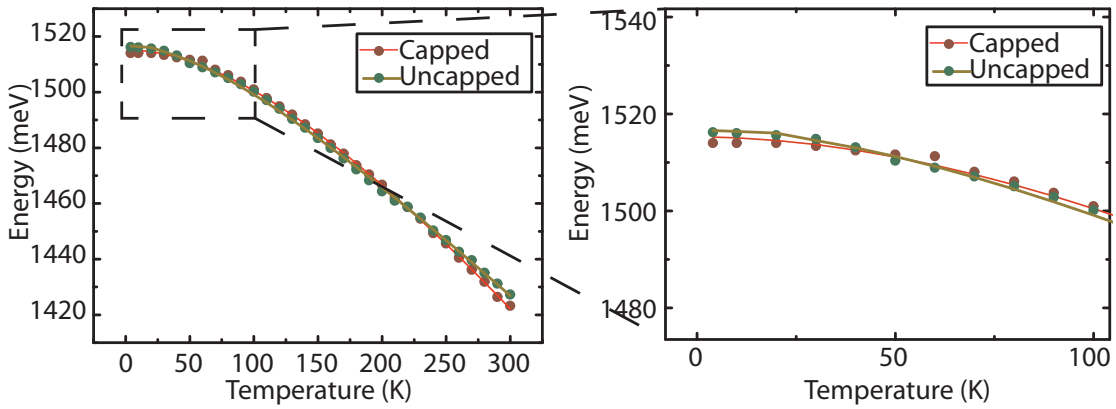

Figure 4.8 – a) Temperature dependent PL spectra of capped and uncapped nanomembrane arrays b) Magnified part of the low temperature (<100K) spectrum

branes capped with AlGaAs shells of different Aluminum concentrations. Figure 4.9 depicts the spectra of uncapped and capped GaAs nanomembranes and the excitonic features they exhibit. First spectra corresponds to the spectra of uncapped and capped nanomembranes with Aluminum concentrations of 15,33 and 50%. The relative intensity of carbon impurity originated emissions is higher in the uncapped sample, while this peak is dominated by the excitonic emissions as a result of the AlGaAs capping samples. A closer look at the exciton peak reveals that they exhibit a more distinctive spectrum, including the peaks of free exciton emission, neutral donor bound exciton emission ($D^0 - X$) and acceptor bound exciton emission ($A^0 - X$). [44] Such excitonic features can be observed only in substrates of extreme crystalline quality.[166][167][168] D0-X and A0-X emissions diminish when nanomembranes are capped with a layer of AlGaAs and only a single exciton peak can be observed. Moreover, its energy red shifts and broadens with increasing Al shell content which points out to an interface effect. Al is reported to induce traps at GaAs/AlGaAs interfaces.[166] Our SIMS analysis of 2D growths also revealed that the concentration of carbon is higher at AlGaAs/GaAs interfaces compared to the rest of the bulk. In order to investigate that effect in detail, nextnano simulations are performed by F. Amaduzzi. We have calculated the band diagrams of GaAs and AlGaAs interfaces by solving the Poisson and Schrodinger equations using nextnano. Results are presented in Figure 4.10. We have introduced carbon induced p-type defects in the interface between AlGaAs and GaAs layers and looked into their effect on the band alignment. Since Aluminum is known to be richer with carbon contamination we have increased the defect density as concentration of Aluminum is increased. The concentration of interface states are $2x10^9, 6x10^9$ and $8x10^9 cm^{-2}$ for an Al concentration of 15%, 30% and 50%. The traps at the interface introduces a triangular potential at the interface where holes can be trapped. Increasing the Al ratio is shifting up the potential. The recombination of the electrons in the conduction bad gap GaAs with the holes trapped at the interface would cause the red shift of the luminescence compared to the free exciton emission of GaAs. We have observed richer excitonic features in another sample set in addition to the uncapped GaAs nanomem-

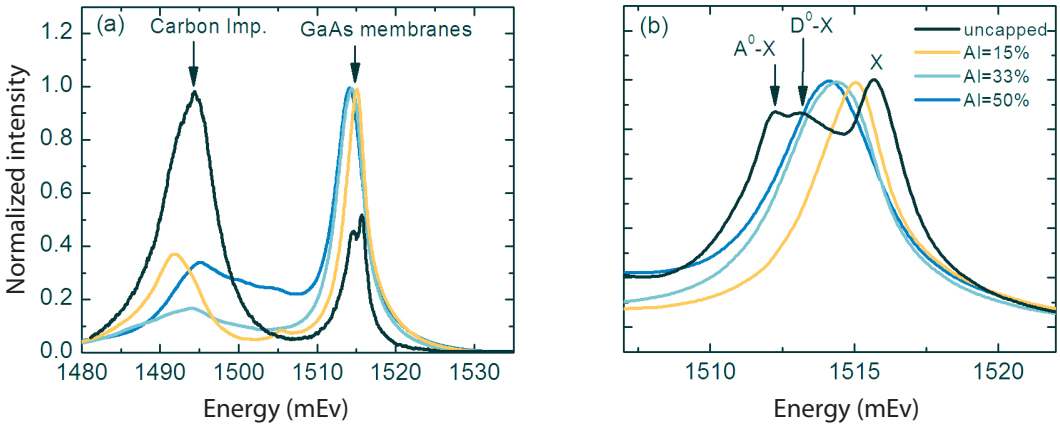

Figure 4.9 – PL spectra of uncapped and capped GaAs nanomembranes with different concentrations of Aluminum (manuscript in preparation by Yang et al.)

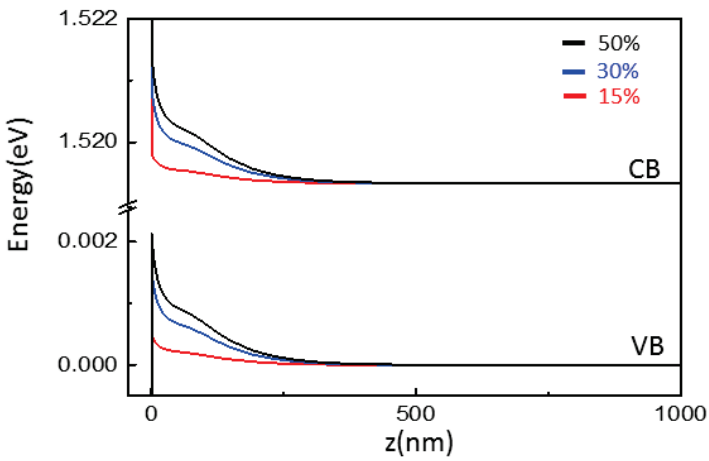

Figure 4.10 – GaAs/AlGaAs interface band alignment calculated through NextNano simulations done by F. Amaduzzi. One would expect quantized levels of the interface enery of $\approx 1 meV$

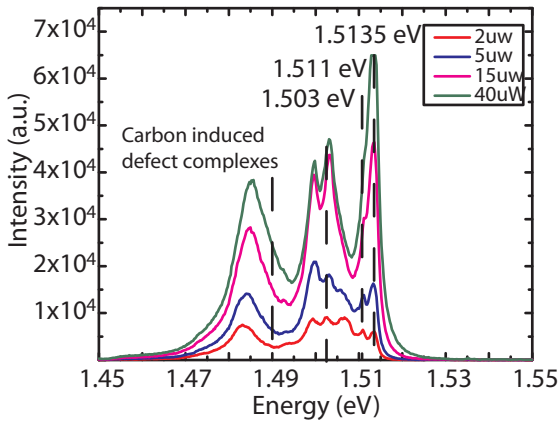

Figure 4.11 – Power dependent PL measurements on AlGaAs/GaAs/AlGaAs 20/5/20 nm nanomembranes and linear fitting of excitonic emissions

branes. These samples had the following configuration of 20 nm $Al_{0.3}Ga_{0.7}As$/5 nm GaAs/20 nm $Al_{0.3}Ga_{0.7}As$. To our surprise we have not observed the fingerprint of QWs at higher energy range of the such spectra. Instead we have observed several peaks between 1.46-1.52 eV energy band. Peaks below 1.49 eV have been shown to be defect-complex $e - A^0$ recombinations at the shallow acceptor level of Carbon. [167] We observe them almost in all GaAs MBE growths since carbon is known to be the dominant shallow acceptor. The existence of the peaks between the free-exciton emission and carbon related impurity peaks are are interesting. High quality bulk GaAs epitaxial layers are reported to exhibit rich excitonic features between 1.49 eV and 1.515 eV due to defect-bound and donor/acceptor exciton emissions. We performed power dependent measurements and noticed that the intensity of the peaks exhibit different behaviour as power increases.

The peak positioned just below free exciton emission is attributed to neutral donor exciton emission. As we increase the power, it is getting broader and finally joins the free exciton emission. It can be proposed that increasing number of generated e-h pairs screen the electric field of the donor exciton and dominate the spectrum as we increase the power. Two other distinctive features at 1.503 eV and 1.5 eV saturates at 40 μW. They do not diminish as power increases and remain distinguishable within the investigated range. We attribute them to the twinning defects formed at the edges of the mask openings due to imperfections of the lithography and the following etching step.

Rich excitonic features of the the membranes open new avenues in the investigation of bound excitons in nanostructures. We will perform more in depth studies on that issue in collaboration with the group of Dr. Plochocka using magneto-PL technique.

The investigation of the structural and optical properties of the core/shell nanomembranes reveal the superior crystalline quality of such nanostructures. Following those studies we have worked on more sophisticated heterostructures as will be mentioned in the next section.

4.3 Quantum heterostructures

Quantum Wells

Following our studies on AlGaAs capped nanomembranes, we have further functionalized these structures and embedded GaAs QWs in AlGaAs shells. In order to do so, we have used very similar growth conditions to core/shell nanomembranes. We have decreased the growth temperature to 460 °C and maximized the V/III ratio by opening the As valve 100%. The only difference was the interruption of Aluminum flux during AlGaAs shell growth in order to create a layer of only GaAs. QWs of different thicknesses have been grown by changing the growth time accordingly.

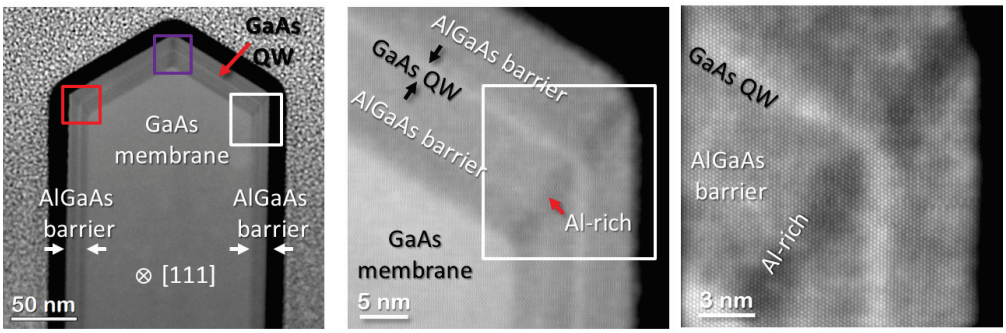

Figure 4.12 – HAADF/TEM imaging of the QW embedded nanomembrane heterostructure a) Low magnification to demonstrate conformality of the $Al_{0.3}Ga_{0.7}As$ shell b) A closer look at the corner of the nanomembrane c) Detailed investigation of the Aluminum segregation line in <11-2>

Cross-section TEM measurements are performed to examine GaAs QW layer. In Figure 4.12 a vertical cross section of the QW embedded GaAs/AlGaAs nanomembrane is demonstrated. In Figure 4.12a membrane geometry and continuity of the QW along top and side facets is revealed. In Figure 4.12b magnified section of the right part of the membrane tip is given. GaAs QW and Al segregation along <11-2> direction can be distinguished. On Figure 4.12c, we present a zoom-out of the segregated region and the quantum well.

We observe that the thickness of the AlGaAs layer is not homogeneous at the top and side facets. The same applies to GaAs QW as well, although it is not directly observable due to extremely small dimensions of the QW. For MBE growths the directionality of the flux and orientation of the nanostructure can yield to different amount of deposition on different facets. Moreover due to different sticking coefficients of adatoms on different crystalline orientations, growth rate can change significantly depending on the orientation of the facet. So all the facets would receive an amount of flux that is proportional with the dot product of incoming Ga flux vector and their substrate normal. In Figure 4.13, the directionality of the incoming flux is schematized with the membrane geometry. Since we grow in As-rich conditions and growth rate is limited by the amount of Gallium, only the Gallium cell position is presented.

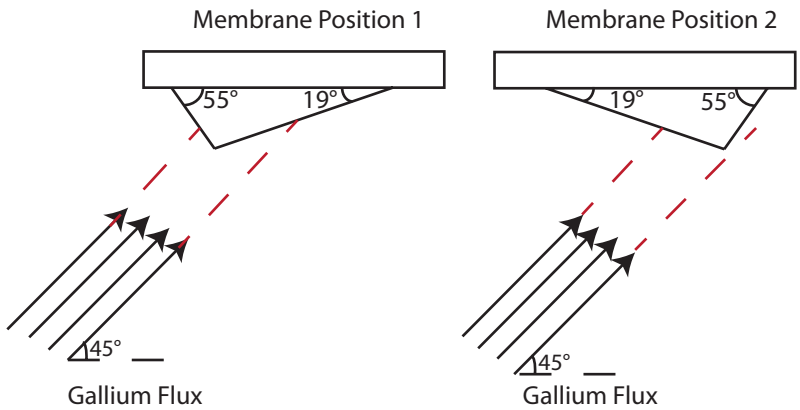

Figure 4.13 – The illustration to demonstrate the directionality of Ga flux and two extreme positions of the substrate vs the flux

As it is depicted in the image, in the configuration of our MBE machine, all effusion cells are positioned with 45 degrees to the substrate normal. We need to take this into account when we are calculating the amount of deposition each facet received. In addition to that we have shadowing effects caused by the special membrane geometry. Our TEM analysis revealed that two end facets of the nanomembranes are positioned with 19° and 55° to the growth substrate. Two conditions where those facets face to the incoming flux as position 1 and position 2 are presented in Figure 4.13. In position 2, steeper facet of (-2-2-1) is masked with the inclined {110} front lateral facets hence does not receive the incoming Ga flux. So we need to build a model that also considers the rotation of the substrate holder. We have tried to create a model to calculate the relative amount of deposition in every facet as following. Initially we considered that 2D growth rate on different facets is mainly proportional to the impingement of group III adatoms. This means the growth rate is proportional to the scalar product of surface normal vector and the unit vector of the flux as following.

$$d \propto \int_0^{2\pi} \vec{n_{Ga}} \cdot \vec{n}_f(\alpha) d\alpha \tag{4.2}$$

One needs to integrate the scalar product in the full rotation range since sample is rotating during the growth process. We have chosen the growth axis of (111)B as the rotation center and wrote the rotation matrix for (-1-1-1) vector, $\vec{R}$, as following.

$$\begin{pmatrix} 1/3(1+2\cos\theta) & 1/3(1-2\cos\theta+\sqrt{3}\sin\theta) & 1/3(-1+\cos\theta+\sqrt{3}) \\ 1/3(1-\cos\theta-\sqrt{3}\sin\theta) & 1/3(1+2\cos\theta) & 1/3(-1+\cos\theta-\sqrt{3}\sin\theta) \\ 1/3(-1+\cos\theta-\sqrt{3}\sin\theta) & 1/3(-1+\cos\theta-\sqrt{3}\sin\theta) & 1/3(1+2\cos\theta) \end{pmatrix} \tag{4.3}$$

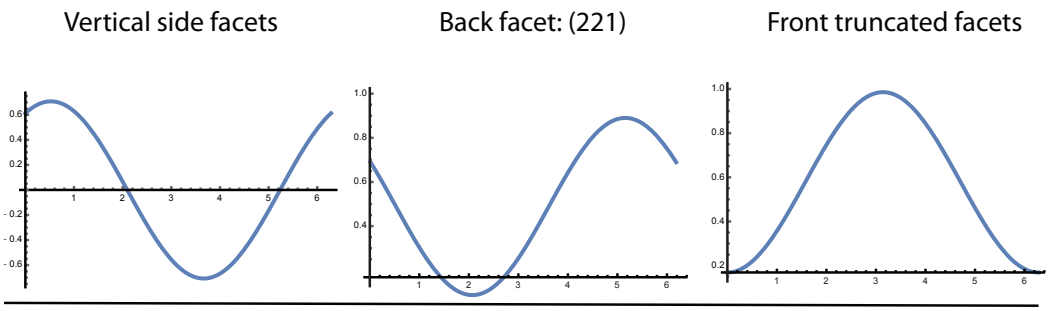

Figure 4.14 – Plot of the scalar products of the facet normal and flux vector from 0 to 2π for different facets

Next we have redefined the surface normal vector of the facet according to the rotation matrix by taking the dot product of the two vectors. In that particular example we are using the side facet of (1-10).

$$\vec{n}_{(1-10)} = \vec{R} \cdot \begin{pmatrix} 1 \\ -1 \\ 0 \end{pmatrix} \tag{4.4}$$

$$\vec{n}_{(Ga)} = \begin{pmatrix} \sin 45° \\ 0 \\ \cos 45° \end{pmatrix} \qquad \vec{n}_{(Ga)} = \begin{pmatrix} -1 \\ (-4-\sqrt{18}) \\ -1 \end{pmatrix} \tag{4.5}$$

Since rotation axis is defined as [-1-1-1], flux vector needs to be redefined in the basis of [-1-1-1] as well. Simplified version of the flux vector $\{\sin 45°, 0, \cos 45°\}$ does not coincide with the (-1-1-1) plane with an angle of 45°. Therefore we have chosen another vector which is inclined 45° to the substrate normal: $\{-1, (-4-\sqrt{18}), -1\}$. Both vectors are presented Equation 4.5 In Figure 4.14, scalar products of the new flux vector and facet normals are plotted from 0 to 2π for representative facets. Negative parts of the curves represent the duration when facet is not facing the effusion cell. We can observe that front truncated facets always receive the incoming flux while back facet is masked for a short period of rotation as predicted and presented in Figure 4.14. Finally the integration of the product of these two vectors from 0 to 2π gives the proportion of the growth rate on that specific facet.

$$d \propto \int_0^{2\pi} \vec{n_{Ga}} \cdot \vec{n}_{(1-10)}(\theta)\, d\theta \tag{4.6}$$

Facet	Growth Rate	Position of the Facet
(-1-1-1)	4.44	Substrate/Top Facet
(1-10)	1.414	Vertical side facet
(-110)	1.414	Vertical side facet
(-101)	1.414	Lateral Front (alternative)
(0-11)	1.414	Lateral Front (alternative)
(-10-1)	3.6276	Lateral Front (real)
(0-1-1)	3.6276	Lateral Front (real)
(-2-2-1)	2.7381	Back facet (high-index)

Table 4.2 – Calculated relative deposition rates for different facets

We have used the Heaviside step function in order to rule out the parts where the result is negative. Calculated deposition rates are given in Table 4.2.

Table 4.2, where deposited amount of material is presented, enables us to estimate the thickness of each layer on the respective facets. In addition to the geometry of the membranes and direction of the incoming flux, diffusion between the facets and the shadowing factor would change the thickness of the QWs at each facet. Figure4.15a) and b) represent the lateral and vertical cross-sections of the nanomembranes. One would expect to grow the thinnest layers on the vertical sidewalls of the nanomembranes and thickest ones on the frontal facets as depicted in the sketches.

Figure 4.15 – Lateral and vertical cross-section representations of QW heterostructures

CL mapping of a full membrane would help us to detect emission energies of specific facets. In Figure 4.16, CL mapping and spectra of a membrane array with heterostructures of the AlGaAs/GaAs/AlGaAs (20nm/8nm/20nm - nominal) layers are shown. In the CL mapping, each colour is assigned to a different detected energy. In the inset, a secondary electron SEM image of the membrane array is presented. As expected, we observe emission at different energies depending on the excited facet. Red corresponds to the emission at 780 nm (1.587 eV), green indicates the emission at 809 nm (1.533 eV) and blue for 813.7 nm (1.524 eV). In Figure 4.16b, we plot the four spectra collected in the points assigned with each of the colours in the map. In the map, the truncated facets of the membranes in 19° with respect to the substrate appear in blue. As our model predicted 55° inclined (-2-2-1) facet receives less amount of

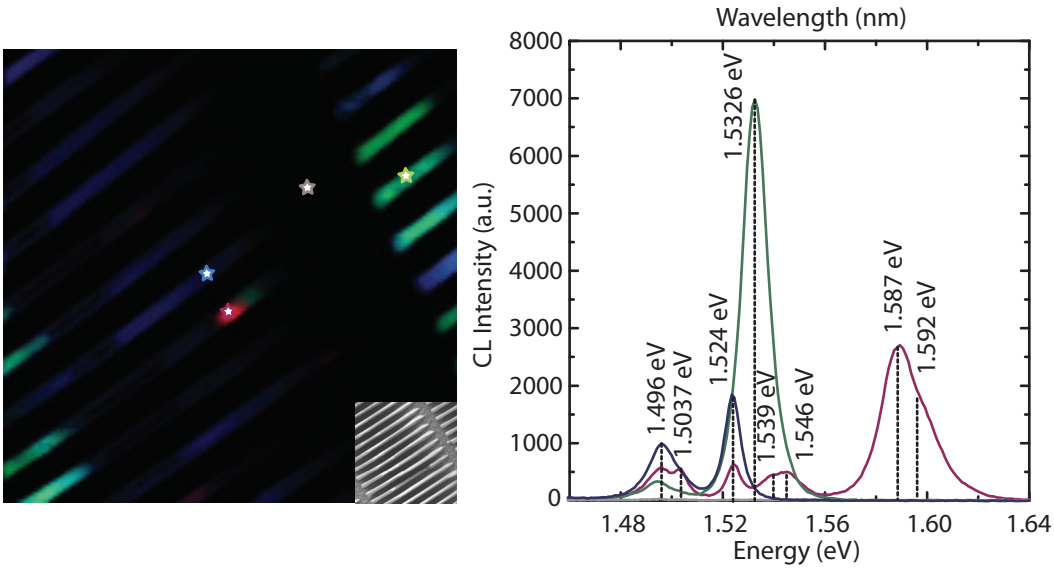

Figure 4.16 – a) CL HYP of the membrane array b) Extracted spectra from pointed regions

flux to compared to other lateral truncated facets of the membranes with 19° inclination. Consequently QWs on (-2-2-1) facets are thinner at emit at higher energies. It is more difficult to resolve the emission coming from the side facets due to overlapping of the signal with the top facet QWs. Membrane geometry would hinder the excitation of the side wall QWs compared to top facet QWs. Although our cross-section TEM analysis point out to thinner sidewall QWs, we do not observe their fingerprint on the spectra. The spectrum colour coded in grey is taken from a region between the membranes in order to check the contribution of the substrate to CL signal. Although the spectrum looks flat when plotted with the same scale of the membrane spectra, it exhibits a very small peak at 828 nm with an intensity 200 times lower, compared to the emission coming from the membrane. As a consequence, in this case we do not have an important contribution from the substrate. Following CL studies of QWs we have proceeded with micro-photoluminescence to access higher spectral resolution and assess the quality of the emission coming from QWs. In Figure 4.17 we present the full spectrum of a membrane array with heterostructures of the AlGaAs/GaAs/AlGaAs (20nm/8nm/20nm - nominal) layers. The range below 1.52 eV is the emission coming from the GaAs core while blue shifted region is the quantum well part. We observe several distinctive peaks at different energies. We have fitted those peaks with Gaussian and found out that we have a FWHM range from 8 meV to 500 μeV. Figure 4.17 presents some examples of the peaks. These findings mean we have a range of QWs on the nanomembranes with different quality. Our TEM analysis shows that the thickness of the QWs grown around the vertical sidewalls of the nanomembranes are smaller than 5 nm. Shi et al. reports that for GaAs QWs below 5 nm they observe localized emissions along the nanowire in the range of 1.7-1.9 eV. Such emissions are very narrow and act like 0D states. They claim such states result from well-width or alloy fluctuations within the QWs. However our CL analysis shows that QWs are delocalized along

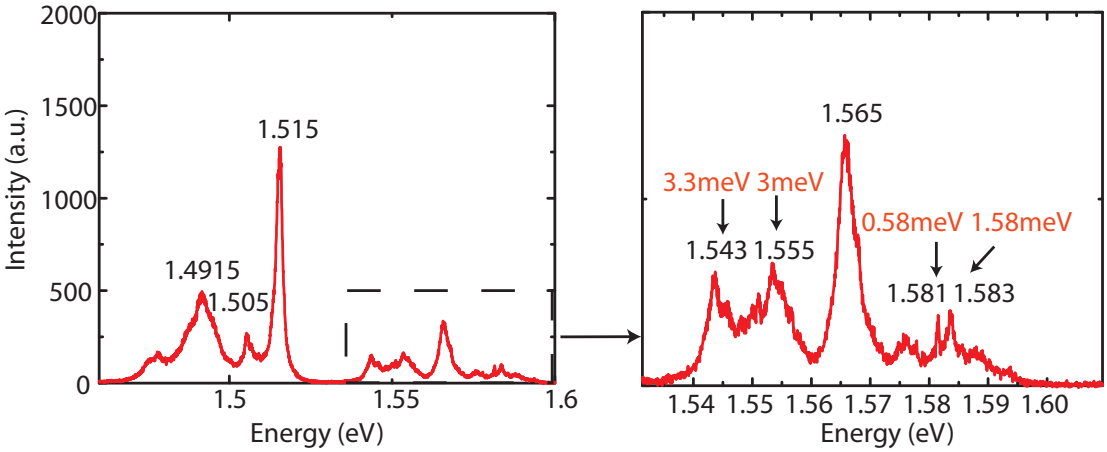

Figure 4.17 – PL spectrum of the 8 nm QW sample a) 1.45-1.6 eV range b) 1.54-1.6 eV range

the facets and the emission ranges do not match pointing out to the high quality QWs.[169] FWHMs we report are comparable to the nanowire QWs reported in the literature and present lower values below meV range indicating the presence of very high quality QWs.

QD like emitters

During our analysis of QW embedded samples, we have observed localized emissions at different parts of the membranes i.e. the emission plotted in red in Figure 4.16, which is localized at the membrane tips. Its emission energy is higher than any level of the quantum wells mentioned before. It is also in the range of quantum dots which we previously observed in core/shell GaAs/AlGaAs nanowires.[25] Although in this particular mapping we observe this emission at the corner of the membrane, we have observed it in other locations of the membranes as well as in other samples, i.e. the tips. In the next figure we present the CL mapping of the core/shell nanomembrane array with nominal 50 nm of $Al_{0.3}Ga_{0.7}As$ shell grown at 550 °C. We have two dominant emissions originating from the membranes. Blue mapping is attributed to 1.497 eV which is the carbon induced donor acceptor transitions, green mapping is attributed to 1.522 eV which is higher than the expected 1.515 eV free exciton emission. Finally red color is used to indicate the higher energy region between 1.6 and 2 eV which is too high to be affiliated with only GaAs quantum confinement. Emission originating from the substrate is dominated by carbon related impurities as expected. The emission coming from the nanomembranes is 70 meV blue shifted compared to the free exciton emission. Free exciton emission of 1.515 eV is marked with the yellow dashed line on the figure. Such a shift is too large to be explained by band filling effects caused by the creation of electron hole pairs above the band gap due to large multiplication effect between electrons and e-h pairs. It can be caused by a quantum confinement induced at quantum wells surrounding the nanomembranes or carrier confinement located in the core. Delocalized nature of the emission is ruling out the possibility of the quantum wells at different facets.

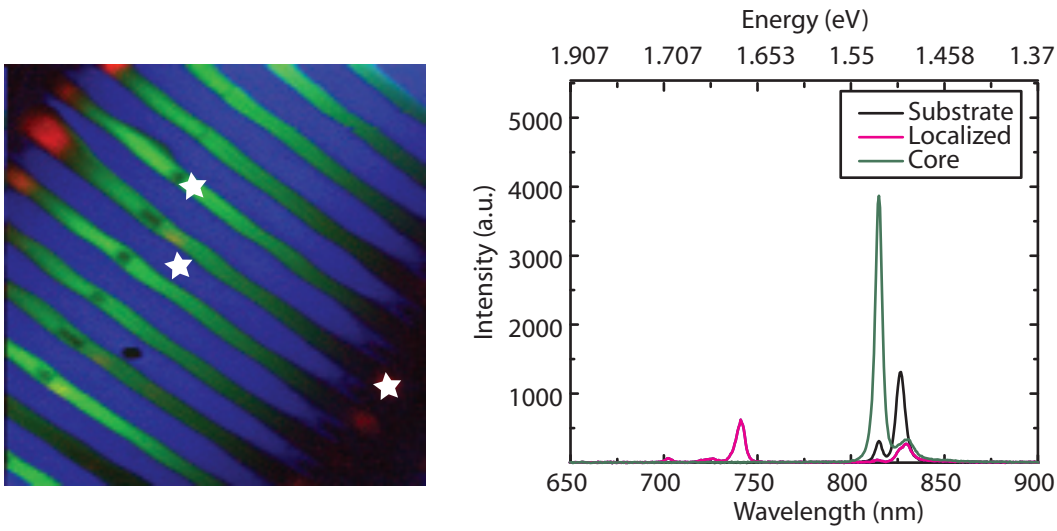

Figure 4.18 – CL mapping of the GaAs/AlGaAs core/shell nanomembrane array with localized emissions at the tips

In that case we suspect a level of confinement induced by unintentional doping in the shell caused by GaAs QWs as observed in the Figure 4.12. Such an effect is previously observed for GaAs nanowires capped with AlAs shells equipped with multi QWs of GaAs.[166] We would like to point out the localized emissions originating from the tips of the membranes where usually we have non-uniform deposition of material due to boundary effects. The position and energy range of the emissions resemble the self-assembled QDs previously observed in core/shell GaAs/AlGaAs nanowires. Francaviglia et al reported that the number of QDs increases with the shell thickness and there seems to be a threshold of 30 nm to induce QD formation. [158] Using that information we have grown a series of samples with 150 nm of nominal AlGaAs shell thickness. We have performed CL mappings on these samples. In Figure 4.19 the CL mapping of an individual membrane on such an array is demonstrated. On the left 3D plotted SE image of the section is demonstrated and at each row characteristic localized emissions on these sections are presented. Localized emissions are in the window of 700(1.77 eV) to 750 nm (1.65eV). They usually originate from the apexes and the corners of the nanomembranes which point out to an effect of the curvature. In addition to round features, we also observe more elongated shapes which might hint to the formation of other quantum features such as QWs and Qwires in addition to the QDs.

In Figure 4.20 we present the average spectra collected from different parts of the membranes. QD like emitters are highly populated in the ends of the nanomembranes compared to the middle section of the nanomembrane. Moreover their emission is stronger in the 19° frontal truncated facets which are defined as tail section of the nanomembrane. The emission range is approximately the same for all the regions.

Next we have analyzed three samples with different Aluminum concentrations of 21%, 33%

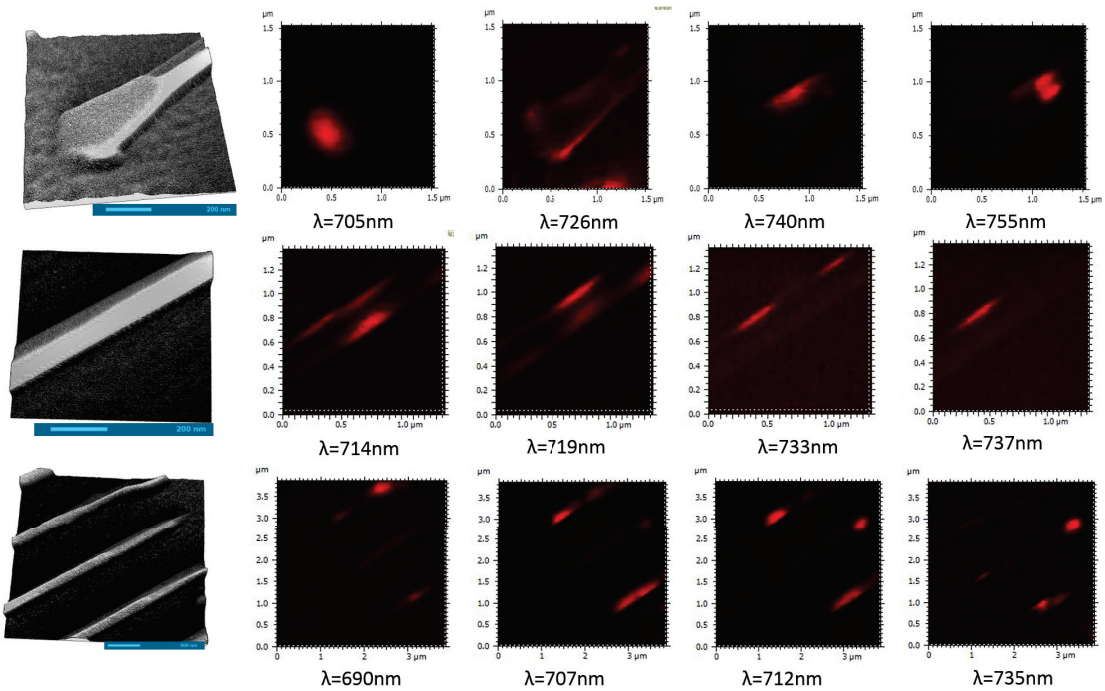

Figure 4.19 – CL mapping of the localized emissions in the different parts of the individual membranes

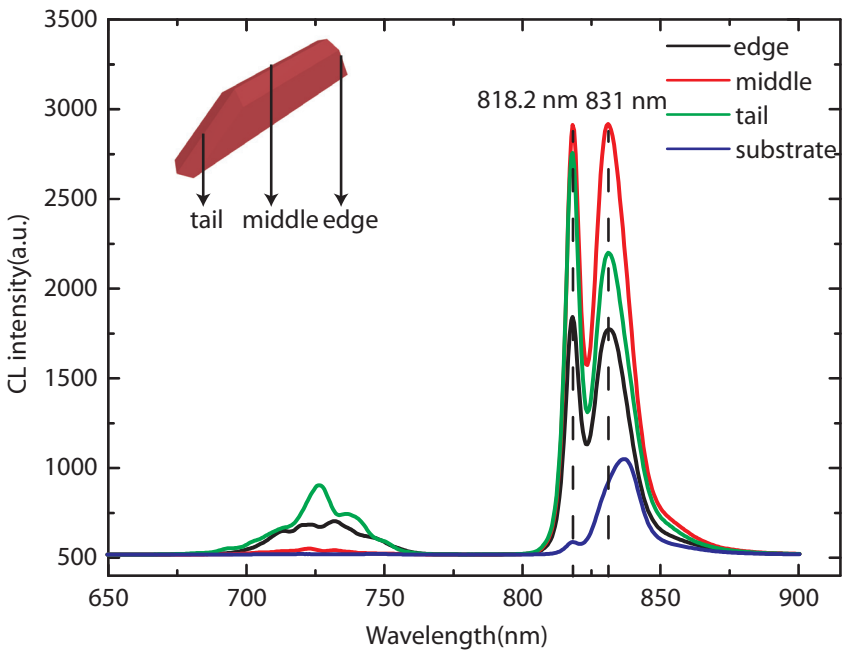

Figure 4.20 – Average CL spectra collected from the different regions of the nanomembranes

and 51%. We have extracted the HYP maps from $5\mu m x 5\mu m$ regions of the each sample. We have masked the substrate and collected the spectrum of the each pixel. We have analyzed the spectra from 620 nm to 770 nm where we observe emission coming from localized emitters and extracted the histograms of the emission energies. We have accounted the presence of the peaks at relative wavelengths rather than the emission intensities. Results are presented in the Figure 4.21. 21% Al sample exhibit a broad range from 660 nm to the 770 nm with a weak tail at the lower energy part. Maximum number of emitters are populated in 670-700 nm range. 33% Al sample presents a more Gaussian distribution while being shifted to higher energies. Emission density seems to be more uniform for a wider region compared to the 21% sample. Lastly 51% sample is positioned at the highest energy range with a tail resembling the 21%. Emission window is the narrowest compared to other 2 samples. This is the result of larger energy shift of the eigenenergies of the QDs. Such a shift could be the result of either stronger localization caused by the fact that wavefunctions of the QDs will be more tightly confined in Al richer envelops or local Al concentration of Ga-rich clusters is higher. Since the growth mechanism we propose is based on the formation of Ga-rich AlGaAs clusters embedded within Al rich AlGaAs envelops, it is expected for the band gap energy of QDs to increase as aluminum ratio of Ga-rich clusters increases. However same effect could also cause the overall number of QDs to decrease as aluminum concentration increases.

Another interesting feature of the histograms is the fact that emission range is getting narrower as we increase the concentration of Aluminum. The spread in the energy range of QDs is the consequence of the nucleation and diffusion dynamics that effect the formation of Ga-rich AlGaAs clusters. When the local Al concentration is higher in the shell, Al segregation effects might become more pronounced and QD formation process got faster resulting with smaller and higher amount of QDs with a narrow size distribution.

Finally we have analyzed the samples with 100 nm and 150 nm thick AlGaAs shells with photoluminescence in order to asses more detailed spectral information about QDs. We have observed sharp and distinctive features in the same range of CL emissions. FWHM of the peaks in this range was between $100\mu eV$ and $800\mu eV$ which indicates a high level of quantum confinement. Two of the spectra demonstrating sharp and distinctive emissions are presented Figure 4.22 a) and b). When we have performed power series on the sharpest peaks we have observed free exciton and charged exciton behavior as demonstrated in Figure 4.22 c) and d). We are currently investigating the single photo emitter nature of such emissions.

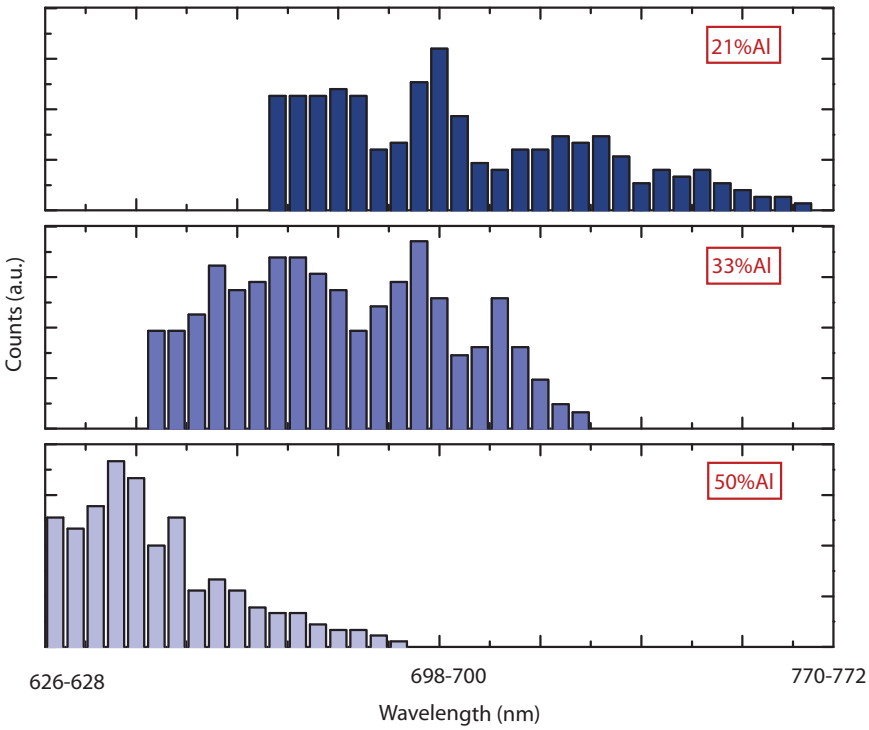

Figure 4.21 – Histograms of the emission centers in high energy range for different concentrations of Aluminum

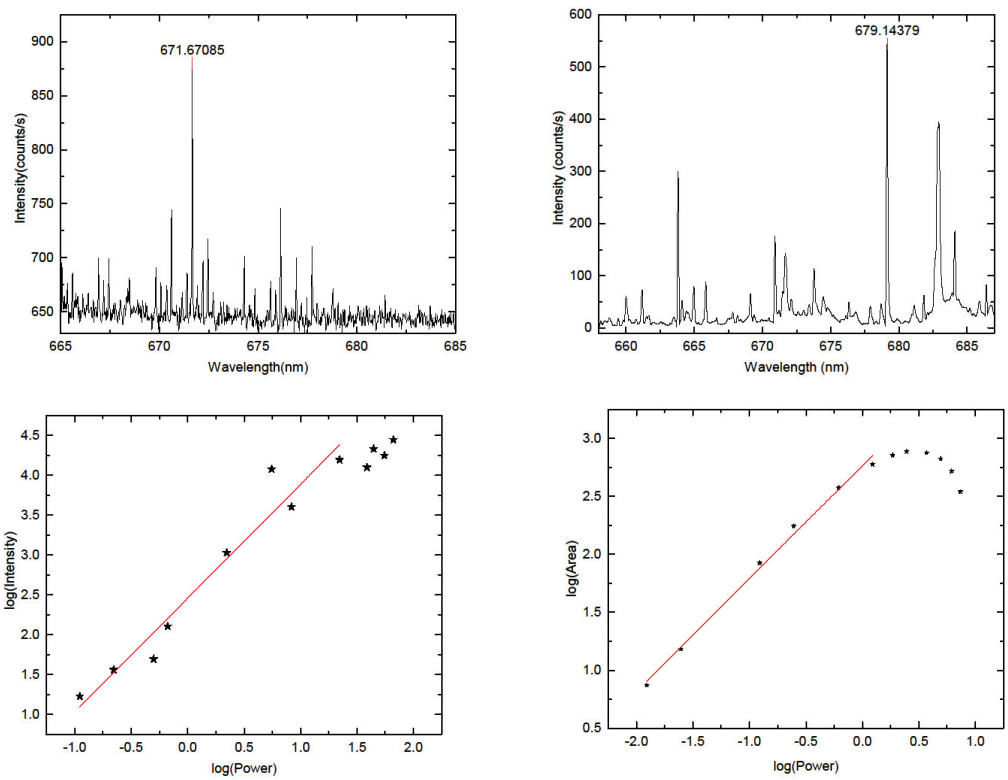

Figure 4.22 – PL spectra of excitonic features and their power dependence

5 Conclusion & Outlook

In this thesis we investigated the growth and characterization of the optoelectronic properties of III-V semiconductor nanostructures, namely nanowires and nanoscale membranes. Nanostructures allow us to study new and exciting physical properties while enabling the exploitation and further functionalization of the inherent III-V semiconductor properties. In the first part of the thesis, we explored the parameter space for the growth of GaAs nanowires on GaAs substrates. We now master their dimensions, tapering and density. These nanowires were engineered and used for applications in optomechanics and optoelectronics. In the most recent work, they are employed as sensors in vectorial scanning force microscopy. In addition to that, we have optimized the dimensions of the GaAs nanowires and capped them with AlGaAs shells to passivate their surface and achieve lasing. Next, we have also optimize the growth of GaAs nanowires on (111) Silicon substrates, both in a self-assembled and organized fashion. The work we performed on the growth of GaAs nanowires on Silicon substrates was motivated by the integration of III-V materials with Silicon technology. For the case of self-assembly, the nature of the native Silicon oxide was found to be of great importance. Depending on the thickness of the native oxide GaAs growth changed drastically from 2D polycrystalline layer to the vertical nanowires with 100% yield. A detailed study of the initial steps of the growth was necessary to understand the relation between the nature of the oxide layer and the nanowire growth. We showed that the surface energy of Silicon oxide layer and the dimensions of the formed pinholes change the initial pinning of Gallium droplets on the surface. The contact angle of Gallium droplets was the key to obtain vertical GaAs nanowires on (111) Silicon. For the organized growth of GaAs nanowires on (111) Silicon, we highlighted the factors that hinder the growth of GaAs nanowire arrays with reproducible yield. In particular, we revealed that the pinning of Gallium droplet on the surface with optimum contact angle was essential in that case as well. We proposed different methods to achieve the optimum pinning of Ga droplets at the initial stages of the growth.

The rest of the thesis was dedicated to the growth of defect-free structures. We tackled the issue of polytypism and stacking faults which are inherent problems of the growth of nanostructures. We took two different approaches to create defect-free pure zinc-blende GaAs

nanostructures. The first proposal consisted in modifying the polarity of GaAs nanowires from B to A, inspired by recent results from the Jagadish group at the Australian National University. By growing on (100) GaAs substrates, the A and B polarities could be identified by the growth direction without any microscopic analysis. In this way we optimized the growth parameters to obtain a high yield of (111)A nanowires on (100) GaAs. Indeed, GaAs nanowires grown in (111)A direction exhibited a defect-free structure in contrast to the nanowires grown in (111)B direction. We then related the polarity with their crystalline structure in detail with aberration-corrected transmission electron microscopy and performed CL studies to characterize the optical properties. Our second approach was to 'lock out' the defects by growing elongated nanostructures along certain directions in the form of nanoscale membranes. We showed that the morphology of the GaAs nanoscale membranes presented a strong dependence on the direction. Only when they are oriented in <11-2> and <2-1-1> directions they exhibited pure zinc-blende crystalline structure, as shown with HRTEM. We studied their growth mechanism and determined the parameter window to obtain high aspect-ratio nanoscale membranes. Next, we used them as templates to grow quantum heterostructures. We investigated their optical properties with photoluminescence and cathodoluminescence. We grew an AlGaAs shell around GaAs nanoscale membranes and functionalized it with quantum wells. Quantum wells were found to exhibit bright luminescence with narrow linewidth. Additionally, we investigated the local alloy fluctuations in the AlGaAs shell. They exhibited sharp and localized luminescence characteristics like self-assembled quantum dots. We believe our work has made a significant contribution to crystal phase engineering literature and leads the way to understand the exact formation mechanism of the quantum dots formed by local alloy fluctuations. In conclusion, we realized the growth and optical characterization of several nanostructure systems for different applications. We believe we contributed to the fundamental understanding of different growth systems and discovered how to tailor the characteristics of such nanostructures for specific applications. In the future it would be very interesting to further study initial growth phases of (111)A GaAs nanowires and to create more sophisticated heterostructures using them as templates. The optical properties of GaAs nanoscale membranes deserve a deeper understanding as well. Being defect free, GaAs nanoscale membranes exhibit superior optical properties which are met only in high quality bulk epitaxial growths so far.

6 Publication List

Self-catalyzed GaAs nanowire growth on (111)B GaAs substrates

Nanomechanics:

Nonlinear motion and mechanical mixing in as-grown GaAs nanowires APL 105, 17, 173111 (2014) FR Braakman, D Cadeddu, G Tütüncüoglu et al. [120]

Time-Resolved Nonlinear Coupling between Orthogonal Flexural Modes of a Pristine GaAs Nanowire Nano Letters 16(2) (2016) D Cadeddu, FR Braakman, G Tütüncüoglu et al. [122]

Vectorial scanning force microscopy using a nanowire sensor Nature Nanotechnology asap. N. Rossi, F. R. Braakman, D. Cadeddu, D. Vasyukov, G. Tütüncüoglu, A. Fontcuberta i Morral, M. Poggio [121]

Nanowire lasers:
Plasmonic waveguide-integrated nanowire laser Esteban Bermúdez-Ureña1, Gozde Tutuncuoglu, Javier Cuerda, Cameron C. L. Smith, Jorge Bravo-Abad, Sergey I. Bozhevolnyi, Anna Fontcuberta i Morral, Francisco J. García-Vidal, and Romain Quidant, Nanoletters (2017) asap

GaAs nanowire growth on (111) Silicon substrates

Position controlled nanowire growth on (111) Silicon
III–V nanowire arrays: growth and light interaction Nanotechnology 25,1,14015 (2014) M Heiss*, E Russo-Averchi*, A Dalmau-Mallorqui*, G Tütüncüoglu* et al. *Equal contribution [126]

High yield of GaAs nanowire arrays on Si mediated by the pinning and contact angle of Ga Nano letters (2015) E Russo-Averchi*, J Vukajlovic Plestina*, G Tütüncüoglu* et al. *Equal contribution [141]

Self-assisted nanowire growth on (111) Silicon
Ga-assisted growth of GaAs nanowires on silicon, comparison of surface SiOx of different

nature Journal of Crystal Growth 404, 246-255 (2014) F Matteini, G Tütüncüoglu, D Rüffer, E Alarcon-Llado, AF i Morral [93]

Tailoring the diameter and density of self-catalyzed GaAs nanowires on silicon Nanotechnology 26,10,105603 (2015) F Matteini, VG Dubrovskii, D Rüffer, G Tütüncüoglu et al. [133]

Wetting of Ga on SiOx and Its Impact on GaAs Nanowire Growth Crystal Growth & Design · May 2015 F. Matteini, G. Tutuncuoglu, H. Potts, F. Jabeen, AF i Morral [133]

Impact of the Ga droplet wetting, morphology, and pinholes on the orientation of GaAs nanowires * Crystal Growth & Design · (Just accepted) F. Matteini, G. Tutuncuoglu, H. Potts, C. Carter, AF i Morral

GaAs nanowire growth on (100) GaAs substrates: The role of polarity on the crystal quality

(111)A GaAs nanowires on (100) GaAs substrates Mahdi Zamani, Gozde Tutuncuoglu et al. (in preparation)

GaAs Nanoscale Membranes

Tutuncuoglu, G., Mata, M. de la, Deiana, D., Potts, H., Matteini, F., Arbiol, J., Morral, A.F. i, 2015. Towards defect-free 1-D GaAs/AlGaAs heterostructures based on GaAs nanomembranes. Nanoscale 7, 19453–19460.

Bibliography

[1] Intel. Advancing Moore's Law —The Road to 14 nm.

[2] PWC. Faster, greener, smarter – reaching beyond the horizon in the world of semiconductors.

[3] Jon Cartwright. Intel enters the third dimension. *Nature*, May 2011.

[4] Heike Riel, Lars-Erik Wernersson, Minghwei Hong, and Jesús A. del Alamo. III–V compound semiconductor transistors—from planar to nanowire structures. *MRS Bulletin*, 39(8):668–677, August 2014.

[5] Jesús A. del Alamo. Nanometre-scale electronics with III-V compound semiconductors. *Nature*, 479(7373):317–323, November 2011.

[6] Adrian M. Ionescu and Heike Riel. Tunnel field-effect transistors as energy-efficient electronic switches. *Nature*, 479(7373):329–337, November 2011.

[7] K. E. Moselund, D. Cutaia, H. Schmid, H. Riel, S. Sant, and A. Schenk. Complementary III #x2013;V heterostructure tunnel FETs. In *2016 46th European Solid-State Device Research Conference (ESSDERC)*, pages 403–407, September 2016.

[8] Yang Zeng, Qinghao Ye, and Wenzhong Shen. Design principles for single standing nanowire solar cells: going beyond the planar efficiency limits. *Scientific Reports*, 4, May 2014.

[9] Peter Krogstrup, Henrik Ingerslev Jørgensen, Martin Heiss, Olivier Demichel, Jeppe V. Holm, Martin Aagesen, Jesper Nygard, and Anna Fontcuberta i Morral. Single-nanowire solar cells beyond the Shockley-Queisser limit. *Nature Photonics*, 7(4):306–310, April 2013.

[10] Jesper Wallentin, Nicklas Anttu, Damir Asoli, Maria Huffman, Ingvar Åberg, Martin H. Magnusson, Gerald Siefer, Peter Fuss-Kailuweit, Frank Dimroth, Bernd Witzigmann, H. Q. Xu, Lars Samuelson, Knut Deppert, and Magnus T. Borgström. InP Nanowire Array Solar Cells Achieving 13.8% Efficiency by Exceeding the Ray Optics Limit. *Science*, 339(6123):1057–1060, March 2013.

[11] Thomas J. Kempa, Bozhi Tian, Dong Rip Kim, Jinsong Hu, Xiaolin Zheng, and Charles M. Lieber. Single and Tandem Axial p-i-n Nanowire Photovoltaic Devices. *Nano Letters*, 8(10):3456–3460, October 2008.

[12] Albert Polman and Harry A. Atwater. Photonic design principles for ultrahigh-efficiency photovoltaics. *Nature Materials*, 11(3):174–177, March 2012.

[13] Michael D. Kelzenberg, Shannon W. Boettcher, Jan A. Petykiewicz, Daniel B. Turner-Evans, Morgan C. Putnam, Emily L. Warren, Joshua M. Spurgeon, Ryan M. Briggs, Nathan S. Lewis, and Harry A. Atwater. Enhanced absorption and carrier collection in Si wire arrays for photovoltaic applications. *Nature Materials*, 9(4):368–368, April 2010.

[14] Maoqing Yao, Sen Cong, Shermin Arab, Ningfeng Huang, Michelle L. Povinelli, Stephen B. Cronin, P. Daniel Dapkus, and Chongwu Zhou. Tandem Solar Cells Using GaAs Nanowires on Si: Design, Fabrication, and Observation of Voltage Addition. *Nano Letters*, 15(11):7217–7224, November 2015.

[15] Tim Burgess, Dhruv Saxena, Sudha Mokkapati, Zhe Li, Christopher R. Hall, Jeffrey A. Davis, Yuda Wang, Leigh M. Smith, Lan Fu, Philippe Caroff, Hark Hoe Tan, and Chennupati Jagadish. Doping-enhanced radiative efficiency enables lasing in unpassivated GaAs nanowires. *Nature Communications*, 7:11927, June 2016.

[16] Dhruv Saxena, Nian Jiang, Xiaoming Yuan, Sudha Mokkapati, Yanan Guo, Hark Hoe Tan, and Chennupati Jagadish. Design and Room-Temperature Operation of GaAs/AlGaAs Multiple Quantum Well Nanowire Lasers. *Nano Letters*, 16(8):5080–5086, August 2016.

[17] Dhruv Saxena, Fan Wang, Qian Gao, Sudha Mokkapati, Hark Hoe Tan, and Chennupati Jagadish. Mode Profiling of Semiconductor Nanowire Lasers. *Nano Letters*, 15(8):5342–5348, August 2015.

[18] Dhruv Saxena, Sudha Mokkapati, Patrick Parkinson, Nian Jiang, Qiang Gao, Hark Hoe Tan, and Chennupati Jagadish. Optically pumped room-temperature GaAs nanowire lasers. *Nature Photonics*, 7(12):963–968, December 2013.

[19] T. Stettner, P. Zimmermann, B. Loitsch, M. Döblinger, A. Regler, B. Mayer, J. Winnerl, S. Matich, H. Riedl, M. Kaniber, G. Abstreiter, G. Koblmüller, and J. J. Finley. Coaxial GaAs-AlGaAs core-multishell nanowire lasers with epitaxial gain control. *Applied Physics Letters*, 108(1):011108, January 2016.

[20] B. Mayer, L. Janker, D. Rudolph, B. Loitsch, T. Kostenbader, G. Abstreiter, G. Koblmüller, and J. J. Finley. Continuous wave lasing from individual GaAs-AlGaAs core-shell nanowires. *Applied Physics Letters*, 108(7):071107, February 2016.

[21] B. Mayer, L. Janker, B. Loitsch, J. Treu, T. Kostenbader, S. Lichtmannecker, T. Reichert, S. Morkötter, M. Kaniber, G. Abstreiter, C. Gies, G. Koblmüller, and J. J. Finley. Monolithically Integrated High-β Nanowire Lasers on Silicon. *Nano Letters*, 16(1):152–156, January 2016.

[22] Fan Fan, Sunay Turkdogan, Zhicheng Liu, David Shelhammer, and C. Z. Ning. A monolithic white laser. *Nature Nanotechnology*, 10(9):796–803, September 2015.

[23] V. Mourik, K. Zuo, S. M. Frolov, S. R. Plissard, E. P. a. M. Bakkers, and L. P. Kouwenhoven. Signatures of Majorana Fermions in Hybrid Superconductor-Semiconductor Nanowire Devices. *Science*, 336(6084):1003–1007, May 2012.

[24] Katsuhiro Tomioka, Masatoshi Yoshimura, and Takashi Fukui. A III-V nanowire channel on silicon for high-performance vertical transistors. *Nature*, 488(7410):189–192, August 2012.

[25] M. Heiss, Y. Fontana, A. Gustafsson, G. Wüst, C. Magen, D. D. O'Regan, J. W. Luo, B. Ketterer, S. Conesa-Boj, A. V. Kuhlmann, J. Houel, E. Russo-Averchi, J. R. Morante, M. Cantoni, N. Marzari, J. Arbiol, A. Zunger, R. J. Warburton, and A. Fontcuberta i Morral. Self-assembled quantum dots in a nanowire system for quantum photonics. *Nature Materials*, 12(5):439–444, May 2013.

[26] G. Tutuncuoglu, M. de la Mata, D. Deiana, H. Potts, F. Matteini, J. Arbiol, and A. Fontcuberta i Morral. Towards defect-free 1-D GaAs/AlGaAs heterostructures based on GaAs nanomembranes. *Nanoscale*, 7(46):19453–19460, November 2015.

[27] Moïra Hocevar, George Immink, Marcel Verheijen, Nika Akopian, Val Zwiller, Leo Kouwenhoven, and Erik Bakkers. Growth and optical properties of axial hybrid III–V/silicon nanowires. *Nature Communications*, 3:1266, December 2012.

[28] Neimantas Vainorius, Sebastian Lehmann, Daniel Jacobsson, Lars Samuelson, Kimberly A. Dick, and Mats-Erik Pistol. Confinement in Thickness-Controlled GaAs Polytype Nanodots. *Nano Letters*, 15(4):2652–2656, April 2015.

[29] Bruce A. Joyce, Pantelis C. Kelires, and Anton G. Naumovets. *Quantum Dots: Fundamentals, Applications, and Frontiers: Proceedings of the NATO ARW on Quantum Dots: Fundamentals, Applications and Frontiers, Crete, Greece 20 - 24 July 2003*. Springer Science & Business Media, June 2005.

[30] Ting-Wei Yeh, P.Daniel Dapkus, Yen-Ting Lin, L. Stewart, Byungmin Ahn, and S. Nutt. InGaN/GaN nanorod and nanosheet arrays for InGaN-based LEDs. In *2011 IEEE Photonics Conference (PHO)*, pages 385–386, October 2011.

[31] Ting-Wei Yeh, Yen-Ting Lin, Byungmin Ahn, Lawrence S. Stewart, P. Daniel Dapkus, and Steven R. Nutt. Vertical nonpolar growth templates for light emitting diodes formed with GaN nanosheets. *Applied Physics Letters*, 100(3):033119, January 2012.

[32] Matthias Heigoldt, Jordi Arbiol, Danče Spirkoska, Josep M. Rebled, Sònia Conesa-Boj, Gerhard Abstreiter, Francesca Peiró, Joan R. Morante, and Anna Fontcuberta i Morral. Long range epitaxial growth of prismatic heterostructures on the facets of catalyst-free GaAs nanowires. *Journal of Materials Chemistry*, 19(7):840, 2009.

[33] Anna Fontcuberta i Morral, Danče Spirkoska, Jordi Arbiol, Matthias Heigoldt, Joan Ramon Morante, and Gerhard Abstreiter. Prismatic Quantum Heterostructures Synthesized on Molecular-Beam Epitaxy GaAs Nanowires. *Small*, 4(7):899–903, 2008.

[34] Neimantas Vainorius, Sebastian Lehmann, Anders Gustafsson, Lars Samuelson, Kimberly A. Dick, and Mats-Erik Pistol. Wurtzite GaAs Quantum Wires: One-Dimensional Subband Formation. *Nano Letters*, 16(4):2774–2780, April 2016.

[35] Bernhard Loitsch, Daniel Rudolph, Stefanie Morkötter, Markus Döblinger, Gianluca Grimaldi, Lukas Hanschke, Sonja Matich, Eric Parzinger, Ursula Wurstbauer, Gerhard Abstreiter, Jonathan J. Finley, and Gregor Koblmüller. Tunable Quantum Confinement in Ultrathin, Optically Active Semiconductor Nanowires Via Reverse-Reaction Growth. *Advanced Materials*, 27(13):2195–2202, April 2015.

[36] Jessica L. Boland, Sonia Conesa-Boj, Patrick Parkinson, Gözde Tütüncüoglu, Federico Matteini, Daniel Rüffer, Alberto Casadei, Francesca Amaduzzi, Fauzia Jabeen, Christopher L. Davies, Hannah. J. Joyce, Laura M. Herz, Anna Fontcuberta i Morral, and Michael B. Johnston. Modulation Doping of GaAs/AlGaAs Core–Shell Nanowires With Effective Defect Passivation and High Electron Mobility. *Nano Letters*, 15(2):1336–1342, February 2015.

[37] S. Morkötter, N. Jeon, D. Rudolph, B. Loitsch, D. Spirkoska, E. Hoffmann, M. Döblinger, S. Matich, J. J. Finley, L. J. Lauhon, G. Abstreiter, and G. Koblmüller. Demonstration of Confined Electron Gas and Steep-Slope Behavior in Delta-Doped GaAs-AlGaAs Core–Shell Nanowire Transistors. *Nano Letters*, 15(5):3295–3302, May 2015.

[38] Alexander Dorodnyy, Esther Alarcon-Lladó, Valery Shklover, Christian Hafner, Anna Fontcuberta i Morral, and Juerg Leuthold. Efficient Multiterminal Spectrum Splitting via a Nanowire Array Solar Cell. *ACS Photonics*, 2(9):1284–1288, September 2015.

[39] Tom Picraux. Epitaxy.

[40] John Orton and Tom Foxon. *Molecular Beam Epitaxy: A Short History*. Oxford University Press, 2015.

[41] Mohamed Henini. Molecular beam epitaxy from research to mass-production — Part 1. *III-Vs Review*, 9(3):32–34, June 1996.

[42] A. Y. Cho. Growth of III–V semiconductors by molecular beam epitaxy and their properties. *Thin Solid Films*, 100(4):291–317, February 1983.

[43] Peter Yu and Manuel Cardona. *Fundamentals of Semiconductors - Physics and Materials Properties*.

[44] E. Hal Bogardus and H. Barry Bebb. Bound-Exciton, Free-Exciton, Band-Acceptor, Donor-Acceptor, and Auger Recombination in GaAs. *Physical Review*, 176(3):993–1002, December 1968.

[45] Josiah Willard Gibbs. *The collected works / of J. W. Gibbs,...* Green, New-York, 1928. ark:/12148/bpt6k95192s.

[46] W. K. Burton, N. Cabrera, and F. C. Frank. The Growth of Crystals and the Equilibrium Structure of their Surfaces. *Philosophical Transactions of the Royal Society of London A: Mathematical, Physical and Engineering Sciences*, 243(866):299–358, June 1951.

[47] K. Jacobi, L. Geelhaar, J. Márquez, J. Platen, and C. Setzer. The morphology of high-index GaAs surfaces. *Applied Surface Science*, 166(1–4):173–178, October 2000.

[48] Ivan V. Markov. *Crystal Growth for Beginners: Fundamentals of Nucleation, Crystal Growth and Epitaxy (2nd Edition)*. World Scientific, 2003.

[49] Jeffrey Y. Tsao. *Materials Fundamentals of Molecular Beam Epitaxy*. Academic Press, 1993.

[50] A. Y. Cho. Advances in molecular beam epitaxy (MBE). *Journal of Crystal Growth*, 111(1):1–13, May 1991.

[51] Ernst Bauer. Phänomenologische Theorie der Kristallabscheidung an Oberflächen. I. *Zeitschrift für Kristallographie*, 110(1-6):372–394, 1958.

[52] J. X. Chen, A. Markus, A. Fiore, U. Oesterle, R. P. Stanley, J. F. Carlin, R. Houdre, M. Ilegems, L. Lazzarini, L. Nasi, M. T. Todaro, E. Piscopiello, R. Cingolani, M. Catalano, J. Katcki, and J. Ratajczak. Tuning InAs/GaAs quantum dot properties under Stranski-Krastanov growth mode for 1.3 mu m applications. *Journal of Applied Physics*, 91(10):6710–6716, May 2002. WOS:000175572500070.

[53] D. Leonard, K. Pond, and P. M. Petroff. Critical layer thickness for self-assembled InAs islands on GaAs. *Physical Review B*, 50(16):11687–11692, October 1994.

[54] T. Walther, A. G. Cullis, D. J. Norris, and M. Hopkinson. Nature of the Stranski-Krastanow Transition during Epitaxy of InGaAs on GaAs. *Physical Review Letters*, 86(11):2381–2384, March 2001.

[55] P. Michler, A. Kiraz, C. Becher, W. V. Schoenfeld, P. M. Petroff, Lidong Zhang, E. Hu, and A. Imamoglu. A Quantum Dot Single-Photon Turnstile Device. *Science*, 290(5500):2282–2285, December 2000.

[56] M. Mehta, D. Reuter, A. D. Wieck, S. Michaelis de Vasconcellos, A. Zrenner, and C. Meier. An intentionally positioned (In,Ga)As quantum dot in a micron sized light emitting diode. *Applied Physics Letters*, 97(14):143101, October 2010.

[57] Y. Sugiyama, Y. Nakata, K. Imamura, S. Muto, and N. Yokoyama. Stacked InAs self-assembled quantum dots on (001)GaAs grown by molecular beam epitaxy. *Japanese Journal of Applied Physics Part 1-Regular Papers Short Notes & Review Papers*, 35(2B):1320–1324, February 1996. WOS:A1996UD94100110.

[58] Zusing Yang, Chia-Ying Chen, Prathik Roy, and Huan-Tsung Chang. Quantum dot-sensitized solar cells incorporating nanomaterials. *Chemical Communications*, 47(34):9561–9571, 2011. WOS:000293858700002.

[59] G. Wulff. Zur frage der geschwindigkeit des wachstums und der auflosung der krystalflachen. *Z. Krystallogr. Mineral.*, 34:499, 1901.

[60] Craig Rottman and Michael Wortis. Statistical mechanics of equilibrium crystal shapes: Interfacial phase diagrams and phase transitions. *Physics Reports*, 103(1):59–79, January 1984.

[61] Conyers Herring. Some Theorems on the Free Energies of Crystal Surfaces. *Physical Review*, 82(1):87–93, April 1951.

[62] Rachel V. Zucker, Dominique Chatain, Ulrich Dahmen, Serge Hagège, and W. Craig Carter. New software tools for the calculation and display of isolated and attached interfacial-energy minimizing particle shapes. *Journal of Materials Science*, 47(24):8290–8302, December 2012.

[63] Paolo Politi, Geneviève Grenet, Alain Marty, Anne Ponchet, and Jacques Villain. Instabilities in crystal growth by atomic or molecular beams. *Physics Reports*, 324(5–6):271–404, February 2000.

[64] Gert Ehrlich and F. G. Hudda. Atomic View of Surface Self-Diffusion: Tungsten on Tungsten. *The Journal of Chemical Physics*, 44(3):1039–1049, February 1966.

[65] Richard L. Schwoebel and Edward J. Shipsey. Step Motion on Crystal Surfaces. *Journal of Applied Physics*, 37(10):3682–3686, September 1966.

[66] P. Tejedor, P. Šmilauer, C. Roberts, and B. A. Joyce. Surface-morphology evolution during unstable homoepitaxial growth of GaAs(110). *Physical Review B*, 59(3):2341–2345, January 1999.

[67] R. S. Wagner and W. C. Ellis. VAPOR-LIQUID-SOLID MECHANISM OF SINGLE CRYSTAL GROWTH. *Applied Physics Letters*, 4(5):89–90, March 1964.

[68] Frank Glas, Jean-Christophe Harmand, and Gilles Patriarche. Nucleation Antibunching in Catalyst-Assisted Nanowire Growth. *Physical Review Letters*, 104(13):135501, March 2010.

[69] V. G. Dubrovskii. Self-regulated pulsed nucleation in catalyzed nanowire growth. *Physical Review B*, 87(19):195426, May 2013.

[70] Vladimir Dubrovskii. Fundamentals of Nucleation Theory. In *Nucleation Theory and Growth of Nanostructures*, NanoScience and Technology, pages 1–73. Springer Berlin Heidelberg, 2014. DOI: 10.1007/978-3-642-39660-1_1.

[71] V. G. Dubrovskii and M. V. Nazarenko. Surface energy of monolayer formation during nanowire growth by vapor-liquid-solid mechanism. *Technical Physics Letters*, 37(5):427–430, May 2011.

[72] Frank Glas, Mohammed Reda Ramdani, Gilles Patriarche, and Jean-Christophe Harmand. Predictive modeling of self-catalyzed III-V nanowire growth. *Physical Review B*, 88(19):195304, November 2013.

[73] Frank Glas. Statistics of sub-Poissonian nucleation in a nanophase. *Physical Review B*, 90(12):125406, September 2014.

[74] Frank Glas, Jean-Christophe Harmand, and Gilles Patriarche. Why Does Wurtzite Form in Nanowires of III-V Zinc Blende Semiconductors? *Physical Review Letters*, 99(14):146101, October 2007.

[75] Wei Lu and Charles M. Lieber. Semiconductor nanowires. *Journal of Physics D: Applied Physics*, 39(21):R387, 2006.

[76] Hemant Adhikari, Ann F. Marshall, Christopher E. D. Chidsey, and Paul C. McIntyre. Germanium Nanowire Epitaxy: Shape and Orientation Control. *Nano Letters*, 6(2):318–323, February 2006.

[77] S. Kodambaka, J. Tersoff, M. C. Reuter, and F. M. Ross. Germanium Nanowire Growth Below the Eutectic Temperature. *Science*, 316(5825):729–732, May 2007.

[78] Amanda L. Giermann and Carl V. Thompson. Solid-state dewetting for ordered arrays of crystallographically oriented metal particles. *Applied Physics Letters*, 86(12):121903–121903–3, March 2005.

[79] Kimberly A. Dick, Claes Thelander, Lars Samuelson, and Philippe Caroff. Crystal Phase Engineering in Single InAs Nanowires. *Nano Letters*, 10(9):3494–3499, September 2010.

[80] Faustino Martelli, Silvia Rubini, Matteo Piccin, Giorgio Bais, Fauzia Jabeen, Silvano De Franceschi, Vincenzo Grillo, Elvio Carlino, Francesco D'Acapito, Federico Boscherini, Stefano Cabrini, Marco Lazzarino, Luca Businaro, Filippo Romanato, and Alfonso Franciosi. Manganese-Induced Growth of GaAs Nanowires. *Nano Letters*, 6(9):2130–2134, September 2006.

[81] Yewu Wang, Volker Schmidt, Stephan Senz, and Ulrich Gösele. Epitaxial growth of silicon nanowires using an aluminium catalyst. *Nature Nanotechnology*, 1(3):186–189, December 2006.

[82] Rong Sun, Neimantas Vainorius, Daniel Jacobsson, Mats-Erik Pistol, Sebastian Lehmann, and Kimberly A. Dick. Sn-seeded GaAs nanowires grown by MOVPE. *Nanotechnology*, 27(21):215603, 2016.

[83] Kimberly A. Dick and Philippe Caroff. Metal-seeded growth of III–V semiconductor nanowires: towards gold-free synthesis. *Nanoscale*, 6(6):3006–3021, February 2014.

[84] Caroline Lindberg, Alexander Whiticar, Kimberly A. Dick, Niklas Sköld, Jesper Nygård, and Jessica Bolinsson. Silver as Seed-Particle Material for GaAs Nanowires—Dictating Crystal Phase and Growth Direction by Substrate Orientation. *Nano Letters*, 16(4):2181–2188, April 2016.

[85] Hong Jin Fan, Peter Werner, and Margit Zacharias. Semiconductor Nanowires: From Self-Organization to Patterned Growth. *Small*, 2(6):700–717, June 2006.

[86] Sokrates T. Pantelides. *Deep centers in semiconductors*. CRC Press, 1992.

[87] Sang Ho Oh, Klaus van Benthem, Sergio I. Molina, Albina Y. Borisevich, Weidong Luo, Peter Werner, Nikolai D. Zakharov, Dhananjay Kumar, Sokrates T. Pantelides, and Stephen J. Pennycook. Point Defect Configurations of Supersaturated Au Atoms Inside Si Nanowires. *Nano Letters*, 8(4):1016–1019, April 2008.

[88] A. Bailly, O. Renault, N. Barrett, L. F. Zagonel, P. Gentile, N. Pauc, F. Dhalluin, T. Baron, A. Chabli, J. C. Cezar, and N. B. Brookes. Direct Quantification of Gold along a Single Si Nanowire. *Nano Letters*, 8(11):3709–3714, November 2008.

[89] E. Koren, G. Elias, A. Boag, E. R. Hemesath, L. J. Lauhon, and Y. Rosenwaks. Direct Measurement of Individual Deep Traps in Single Silicon Nanowires. *Nano Letters*, 11(6):2499–2502, June 2011.

[90] Giulia Venturi, Antonio Castaldini, Alexander Schleusener, Vladimir Sivakov, and Anna Cavallini. Electronic levels in silicon MaWCE nanowires: evidence of a limited diffusion of Ag. *Nanotechnology*, 26(42):425702, 2015.

[91] A. Fontcuberta i Morral, C. Colombo, G. Abstreiter, J. Arbiol, and J. R. Morante. Nucleation mechanism of gallium-assisted molecular beam epitaxy growth of gallium arsenide nanowires. *Applied Physics Letters*, 92(6):063112–063112–3, February 2008.

[92] Christian Chatillon and Dominique Chatain. Congruent vaporization of GaAs(s) and stability of Ga(l) droplets at the GaAs(s) surface. *Journal of Crystal Growth*, 151(1):91–101, May 1995.

[93] Federico Matteini, Goezde Tuetuencueoglu, Daniel Rueffer, Esther Alarcon-Llado, and Anna Fontcuberta i Morral. Ga-assisted growth of GaAs nanowires on silicon, comparison of surface SiOx of different nature. *Journal of Crystal Growth*, 404:246–255, October 2014. WOS:000341414600040.

[94] Chin-Yu Yeh, Z. W. Lu, S. Froyen, and Alex Zunger. Zinc-blende\char21{}wurtzite polytypism in semiconductors. *Physical Review B*, 46(16):10086–10097, October 1992.

[95] P. Caroff, J. Bolinsson, and J. Johansson. Crystal Phases in III–V Nanowires: From Random Toward Engineered Polytypism. *IEEE Journal of Selected Topics in Quantum Electronics*, 17(4):829–846, July 2011.

[96] Bernt Ketterer, Martin Heiss, Marie J. Livrozet, Andreas Rudolph, Elisabeth Reiger, and Anna Fontcuberta i Morral. Determination of the band gap and the split-off band in wurtzite GaAs using Raman and photoluminescence excitation spectroscopy. *Physical Review B*, 83(12):125307, March 2011.

[97] Bernt Ketterer, Martin Heiss, Emanuele Uccelli, Jordi Arbiol, and Anna Fontcuberta i Morral. Untangling the Electronic Band Structure of Wurtzite GaAs Nanowires by Resonant Raman Spectroscopy. *ACS Nano*, 5(9):7585–7592, September 2011.

[98] Martin Heiss, Sonia Conesa-Boj, Jun Ren, Hsiang-Han Tseng, Adam Gali, Andreas Rudolph, Emanuele Uccelli, Francesca Peiró, Joan Ramon Morante, Dieter Schuh, Elisabeth Reiger, Efthimios Kaxiras, Jordi Arbiol, and Anna Fontcuberta i Morral. Direct correlation of crystal structure and optical properties in wurtzite/zinc-blende GaAs nanowire heterostructures. *Physical Review B*, 83(4):045303, January 2011.

[99] Neimantas Vainorius, Daniel Jacobsson, Sebastian Lehmann, Anders Gustafsson, Kimberly A. Dick, Lars Samuelson, and Mats-Erik Pistol. Observation of type-II recombination in single wurtzite/zinc-blende GaAs heterojunction nanowires. *Physical Review B*, 89(16):165423, April 2014.

[100] S. Raychaudhuri and E. T. Yu. Calculation of critical dimensions for wurtzite and cubic zinc blende coaxial nanowire heterostructures. volume 24, pages 2053–2059. AVS, 2006.

[101] Daniel Jacobsson, Federico Panciera, Jerry Tersoff, Mark C. Reuter, Sebastian Lehmann, Stephan Hofmann, Kimberly A. Dick, and Frances M. Ross. Interface dynamics and crystal phase switching in GaAs nanowires. *Nature*, 531(7594):317–322, March 2016.

[102] Peter Krogstrup, Stefano Curiotto, Erik Johnson, Martin Aagesen, Jesper Nygård, and Dominique Chatain. Impact of the liquid phase shape on the structure of III-V nanowires. *Physical Review Letters*, 106(12):125505, March 2011.

[103] Xuezhe Yu, Hailong Wang, Jun Lu, Jianhua Zhao, Jennifer Misuraca, Peng Xiong, and Stephan von Molnár. Evidence for Structural Phase Transitions Induced by the Triple Phase Line Shift in Self-Catalyzed GaAs Nanowires. *Nano Letters*, 12(10):5436–5442, October 2012.

[104] D. Spirkoska, J. Arbiol, A. Gustafsson, S. Conesa-Boj, F. Glas, I. Zardo, M. Heigoldt, M. H. Gass, A. L. Bleloch, S. Estrade, M. Kaniber, J. Rossler, F. Peiro, J. R. Morante, G. Abstreiter, L. Samuelson, and A. Fontcuberta i Morral. Structural and optical properties of high quality zinc-blende/wurtzite GaAs nanowire heterostructures. *Physical Review B*, 80(24):245325, December 2009.

[105] Hannah J. Joyce, Jennifer Wong-Leung, Qiang Gao, H. Hoe Tan, and Chennupati Jagadish. Phase perfection in zinc Blende and Wurtzite III-V nanowires using basic growth parameters. *Nano Letters*, 10(3):908–915, March 2010.

[106] F. Allegretti, M. Inoue, and T. Nishinaga. In-situ observation of GaAs selective epitaxy on GaAs (111)B substrates. *Journal of Crystal Growth*, 146(1–4):354–358, January 1995.

[107] Martin Heiß, Eva Riedlberger, Dančе Spirkoska, Max Bichler, Gerhard Abstreiter, and Anna Fontcuberta i Morral. Growth mechanisms and optical properties of GaAs-based semiconductor microstructures by selective area epitaxy. *Journal of Crystal Growth*, 310(6):1049–1056, March 2008.

[108] Keitaro Ikejiri, Takuya Sato, Hiroatsu Yoshida, Kenji Hiruma, Junichi Motohisa, Shinjiroh Hara, and Takashi Fukui. Growth characteristics of GaAs nanowires obtained by selective area metal–organic vapour-phase epitaxy. *Nanotechnology*, 19(26):265604, July 2008.

[109] Hiroatsu Yoshida, Keitaro Ikejiri, Takuya Sato, Shinjiroh Hara, Kenji Hiruma, Junichi Motohisa, and Takashi Fukui. Analysis of twin defects in GaAs nanowires and tetrahedra and their correlation to GaAs(1 1 1)B surface reconstructions in selective-area metal organic vapour-phase epitaxy. *Journal of Crystal Growth*, 312(1):52–57, December 2009.

[110] Chun-Yung Chi, Chia-Chi Chang, Shu Hu, Ting-Wei Yeh, Stephen B. Cronin, and P. Daniel Dapkus. Twin-Free GaAs Nanosheets by Selective Area Growth: Implications for Defect-Free Nanostructures. *Nano Letters*, 13(6):2506–2515, June 2013.

[111] N. Moll, A. Kley, E. Pehlke, and M. Scheffler. GaAs equilibrium crystal shape from first principles. *Physical Review B*, 54(12):8844–8855, September 1996.

[112] N. V. Sibirev, M. A. Timofeeva, A. D. Bol'shakov, M. V. Nazarenko, and V. G. Dubrovskiĭ. Surface energy and crystal structure of nanowhiskers of III–V semiconductor compounds. *Physics of the Solid State*, 52(7):1531–1538, July 2010.

[113] Federico Matteini. Growth of GaAs nanowires on Si (111) for photovoltaic applications. 2016.

[114] C. Colombo, D. Spirkoska, M. Frimmer, G. Abstreiter, and A. Fontcuberta i Morral. Ga-assisted catalyst-free growth mechanism of GaAs nanowires by molecular beam epitaxy. *Physical Review B*, 77(15):155326, April 2008.

[115] Regine A. Loberternos, Oliver D. Semblante, Rogelio G. Dizon, Claude R. Ceniza, Jasher John A. Ibanes, Arnel A. Salvador, and Armando S. Somintac. Optimization of anodized aluminum oxide pore morphology for GaAs nanowire growth. *Science Diliman*, 22(1), February 2011.

[116] Y. K. Siew, G. Sarkar, X. Hu, J. Hui, A. See, and C. T. Chua. Thermal Curing of Hydrogen Silsesquioxane. *Journal of The Electrochemical Society*, 147(1):335–339, January 2000.

[117] Chang-Chung Yang and Wen-Chang Chen. The structures and properties of hydrogen silsesquioxane (HSQ) films produced by thermal curing. *Journal of Materials Chemistry*, 12(4):1138–1141, March 2002.

[118] Torsten Rieger, Sonja Heiderich, Steffi Lenk, Mihail Ion Lepsa, and Detlev Grützmacher. Ga-assisted MBE growth of GaAs nanowires using thin HSQ layer. *Journal of Crystal Growth*, 353(1):39–46, August 2012.

[119] Sebastian Lehmann, Daniel Jacobsson, and Kimberly A. Dick. Crystal phase control in GaAs nanowires: opposing trends in the Ga- and As-limited growth regimes. *Nanotechnology*, 26(30):301001, 2015.

[120] F. R. Braakman, D. Cadeddu, G. Tütüncüoglu, F. Matteini, D. Rüffer, A. Fontcuberta i Morral, and M. Poggio. Nonlinear motion and mechanical mixing in as-grown GaAs nanowires. *Applied Physics Letters*, 105(17):173111, October 2014.

[121] Nicola Rossi, Floris R. Braakman, Davide Cadeddu, Denis Vasyukov, Gözde Tütüncüoglu, Anna Fontcuberta i Morral, and Martino Poggio. Vectorial scanning force microscopy using a nanowire sensor. *Nature Nanotechnology*, advance online publication, October 2016.

[122] D. Cadeddu, F. R. Braakman, G. Tütüncüoglu, F. Matteini, D. Rüffer, A. Fontcuberta i Morral, and M. Poggio. Time-Resolved Nonlinear Coupling between Orthogonal Flexural Modes of a Pristine GaAs Nanowire. *Nano Letters*, 16(2):926–931, February 2016.

[123] O. Demichel, M. Heiss, J. Bleuse, H. Mariette, and A. Fontcuberta i Morral. Impact of surfaces on the optical properties of GaAs nanowires. *Applied Physics Letters*, 97(20):201907, November 2010.

[124] Mariano A. Zimmler, Federico Capasso, Sven Müller, and Carsten Ronning. Optically pumped nanowire lasers: invited review. *Semiconductor Science and Technology*, 25(2):024001, 2010.

[125] Emanuele Uccelli, Jordi Arbiol, Cesar Magen, Peter Krogstrup, Eleonora Russo-Averchi, Martin Heiss, Gabriel Mugny, François Morier-Genoud, Jesper Nygård, Joan Ramon Morante, and Anna Fontcuberta i Morral. Three-Dimensional Multiple-Order Twinning of Self-Catalyzed GaAs Nanowires on Si Substrates. *Nano Letters*, 11(9):3827–3832, September 2011.

[126] M. Heiss, E. Russo-Averchi, A. Dalmau-Mallorqui, G. Tuetuencueoglu, F. Matteini, D. Rueffer, S. Conesa-Boj, O. Demichel, E. Alarcon-Llado, and A. Fontcuberta i Morral. III-V nanowire arrays: growth and light interaction. *Nanotechnology*, 25(1):014015, January 2014. WOS:000328641200017.

[127] Steffen Breuer, Carsten Pfüller, Timur Flissikowski, Oliver Brandt, Holger T. Grahn, Lutz Geelhaar, and Henning Riechert. Suitability of Au- and Self-Assisted GaAs Nanowires for Optoelectronic Applications. *Nano Letters*, 11(3):1276–1279, March 2011.

[128] G. E. Cirlin, V. G. Dubrovskii, Yu. B. Samsonenko, A. D. Bouravleuv, K. Durose, Y. Y. Proskuryakov, Budhikar Mendes, L. Bowen, M. A. Kaliteevski, R. A. Abram, and Dagou

Zeze. Self-catalyzed, pure zincblende GaAs nanowires grown on Si(111) by molecular beam epitaxy. *Physical Review B*, 82(3):035302, July 2010.

[129] Fauzia Jabeen, Vincenzo Grillo, Silvia Rubini, and Faustino Martelli. Self-catalyzed growth of GaAs nanowires on cleaved Si by molecular beam epitaxy. *Nanotechnology*, 19(27):275711, July 2008.

[130] Bernhard Mandl, Julian Stangl, Emelie Hilner, Alexei A. Zakharov, Karla Hillerich, Anil W. Dey, Lars Samuelson, Gu?nther Bauer, Knut Deppert, and Anders Mikkelsen. Growth Mechanism of Self-Catalyzed Group III-V Nanowires. *Nano Letters*, 10(11):4443–4449, November 2010.

[131] J. H. Paek, T. Nishiwaki, M. Yamaguchi, and N. Sawaki. Catalyst free MBE-VLS growth of GaAs nanowires on (111)Si substrate. *physica status solidi (c)*, 6(6):1436–1440, 2009.

[132] Daniel Rudolph, Simon Hertenberger, Stefanie Bolte, Watcharapong Paosangthong, Danc?e Spirkoska, Markus Do?blinger, Max Bichler, Jonathan J. Finley, Gerhard Abstreiter, and Gregor Koblmu?ller. Direct Observation of a Noncatalytic Growth Regime for GaAs Nanowires. *Nano Letters*, 11(9):3848–3854, September 2011.

[133] Federico Matteini, Gözde Tütüncüoglu, Heidi Potts, Fauzia Jabeen, and Anna Fontcuberta i Morral. Wetting of Ga on SiOx and Its Impact on GaAs Nanowire Growth. *Crystal Growth & Design*, 15(7):3105–3109, July 2015.

[134] Federico Matteini, Gözde Tütüncüoglu, Dmitry Mikulik, Jelena Vukajlovic-Plestina, Heidi Potts, Jean-Baptiste Leran, W. Craig Carter, and Anna Fontcuberta i Morral. Impact of the Ga droplet wetting, morphology, and pinholes on the orientation of GaAs nanowires. *Crystal Growth & Design*, 2016.

[135] S. Hertenberger, D. Rudolph, M. Bichler, J. J. Finley, G. Abstreiter, and G. Koblmüller. Growth kinetics in position-controlled and catalyst-free InAs nanowire arrays on Si(111) grown by selective area molecular beam epitaxy. *Journal of Applied Physics*, 108(11):114316–114316–7, December 2010.

[136] Magnus T. Borgström, George Immink, Bas Ketelaars, Rienk Algra, and Erik P. A. M. Bakkers. Synergetic nanowire growth. *Nature Nanotechnology*, 2(9):541–544, September 2007.

[137] D. Rudolph, L. Schweickert, S. Morkötter, B. Loitsch, S. Hertenberger, J. Becker, M. Bichler, G. Abstreiter, J. J. Finley, and G. Koblmüller. Effect of interwire separation on growth kinetics and properties of site-selective GaAs nanowires. *Applied Physics Letters*, 105(3):033111, July 2014.

[138] S Plissard, G Larrieu, X Wallart, and P Caroff. High yield of self-catalyzed GaAs nanowire arrays grown on silicon via gallium droplet positioning. *Nanotechnology*, 22(27):275602, July 2011.

[139] Miltiadis K. Hatalis and David W. Greve. Large grain polycrystalline silicon by low-temperature annealing of low-pressure chemical vapor deposited amorphous silicon films. *Journal of Applied Physics*, 63(7):2260–2266, April 1988.

[140] G. L. Olson and J. A. Roth. Kinetics of solid phase crystallization in amorphous silicon. *Materials Science Reports*, 3(1):1–77, January 1988.

[141] Eleonora Russo-Averchi, Jelena Vukajlovic Plestina, Gözde Tütüncüoglu, Federico Matteini, Anna Dalmau-Mallorquí, Maria de la Mata, Daniel Rüffer, Heidi A. Potts, Jordi Arbiol, Sonia Conesa-Boj, and Anna Fontcuberta i Morral. High Yield of GaAs Nanowire Arrays on Si Mediated by the Pinning and Contact Angle of Ga. *Nano Letters*, April 2015.

[142] Xiaoming Yuan, Philippe Caroff, Jennifer Wong-Leung, Lan Fu, Hark Hoe Tan, and Chennupati Jagadish. Tunable Polarity in a III–V Nanowire by Droplet Wetting and Surface Energy Engineering. *Advanced Materials*, 27(40):6096–6103, October 2015.

[143] A. Okamoto. Selective epitaxial growth by molecular beam epitaxy. *Semiconductor Science and Technology*, 8(6):1011, 1993.

[144] F. E. Allegretti, C. Roberts, and J. H. Neave. Morphological study of GaAs grown by periodic supply epitaxy on (111) B substrates. *Journal of Vacuum Science & Technology A*, 15(3):954–957, May 1997.

[145] Seung-Chang Lee, Kevin J. Malloy, and S. R. J. Brueck. Nanoscale selective growth of GaAs by molecular beam epitaxy. *Journal of Applied Physics*, 90(8):4163–4168, October 2001.

[146] Maoqing Yao, Chunyang Sheng, Mingyuan Ge, Chun-Yung Chi, Sen Cong, Aiichiro Nakano, P. Daniel Dapkus, and Chongwu Zhou. Facile Five-Step Heteroepitaxial Growth of GaAs Nanowires on Silicon Substrates and the Twin Formation Mechanism. *ACS Nano*, 10(2):2424–2435, February 2016.

[147] Sébastien Plissard, Kimberly A. Dick, Guilhem Larrieu, Sylvie Godey, Ahmed Addad, Xavier Wallart, and Philippe Caroff. Gold-free growth of GaAs nanowires on silicon: arrays and polytypism. *Nanotechnology*, 21(38):385602, September 2010.

[148] H. Schlötterer, M. Quillec, P. D. Greene, and M. Bertolotti. *Materials for Optoelectronic Devices, OEICs and Photonics*. Elsevier, October 1991. Google-Books-ID: ei3XRTv3d3AC.

[149] T. Takebe, M. Fujii, T. Yamamoto, K. Fujita, and T. Watanabe. Orientation-dependent Ga surface diffusion in molecular beam epitaxy of GaAs on GaAs patterned substrates. *Journal of Applied Physics*, 81(11):7273–7281, June 1997.

[150] Mohammed Reda Ramdani, Jean Christophe Harmand, Frank Glas, Gilles Patriarche, and Laurent Travers. Arsenic Pathways in Self-Catalyzed Growth of GaAs Nanowires. *Crystal Growth & Design*, 13(1):91–96, January 2013.

[151] S. Ando, N. Kobayashi, and H. Ando. Selective area metalorganic chemical vapor deposition growth for hexagonal-facet lasers. *Journal of Crystal Growth*, 145(1):302–307, December 1994.

[152] C. Bocchi, C. Ferrari, P. Franzosi, A. Bosacchi, and S. Franchi. Accurate determination of lattice mismatch in the epitaxial AlAs/GaAs system by high-resolution X-ray diffraction. *Journal of Crystal Growth*, 132(3):427–434, September 1993.

[153] Yannik Fontana, Pierre Corfdir, Barbara Van Hattem, Eleonora Russo-Averchi, Martin Heiss, Samuel Sonderegger, Cesar Magen, Jordi Arbiol, Richard T. Phillips, and Anna Fontcuberta i Morral. Exciton footprint of self-assembled AlGaAs quantum dots in core-shell nanowires. *Physical Review B*, 90(7):075307, August 2014. WOS:000341257800003.

[154] Nari Jeon, Bernhard Loitsch, Stefanie Morkoetter, Gerhard Abstreiter, Jonathan Finley, Hubert J. Krenner, Gregor Koblmueller, and Lincoln J. Lauhon. Alloy Fluctuations Act as Quantum Dot-like Emitters in GaAs-AlGaAs Core–Shell Nanowires. *ACS Nano*, 9(8):8335–8343, August 2015.

[155] D.M. Holmes, J.G. Belk, J.L. Sudijono, J.H. Neave, T.S. Jones, and B.A. Joyce. The nature of island formation in the homoepitaxial growth of GaAs(110). *Surface Science*, 341(1–2):133–141, November 1995.

[156] R. Songmuang, Le Thuy Thanh Giang, J. Bleuse, M. Den Hertog, Y. M. Niquet, Le Si Dang, and H. Mariette. Determination of the Optimal Shell Thickness for Self-Catalyzed GaAs/AlGaAs Core–Shell Nanowires on Silicon. *Nano Letters*, 16(6):3426–3433, June 2016.

[157] Niklas Sköld, Jakob B. Wagner, Gunnel Karlsson, Tania Hernán, Werner Seifert, Mats-Erik Pistol, and Lars Samuelson. Phase Segregation in AlInP Shells on GaAs Nanowires. *Nano Letters*, 6(12):2743–2747, December 2006.

[158] Luca Francaviglia, Yannik Fontana, Sonia Conesa-Boj, Gözde Tütüncüoglu, Léo Duchêne, Mihaela B. Tanasescu, Federico Matteini, and Anna Fontcuberta i Morral. Quantum dots in the GaAs/AlxGa1-xAs core-shell nanowires: Statistical occurrence as a function of the shell thickness. *Applied Physics Letters*, 107(3):033106, July 2015.

[159] Bernhard Loitsch, Nari Jeon, Markus Döblinger, Julia Winnerl, Eric Parzinger, Sonja Matich, Ursula Wurstbauer, Hubert Riedl, Gerhard Abstreiter, Jonathan J. Finley, Lincoln J. Lauhon, and Gregor Koblmüller. Suppression of alloy fluctuations in GaAs-AlGaAs core-shell nanowires. *Applied Physics Letters*, 109(9):093105, August 2016.

[160] E. Grilli, M. Guzzi, R. Zamboni, and L. Pavesi. High-precision determination of the temperature dependence of the fundamental energy gap in gallium arsenide. *Physical Review B*, 45(4):1638–1644, January 1992.

[161] Y. P. Varshni. Temperature dependence of the energy gap in semiconductors. *Physica*, 34(1):149–154, January 1967.

[162] H. Shen, S. H. Pan, Z. Hang, Jing Leng, Fred H. Pollak, J. M. Woodall, and R. N. Sacks. Photoreflectance of GaAs and Ga0.82al0.18as at elevated temperatures up to 600 °C. *Applied Physics Letters*, 53(12):1080–1082, September 1988.

[163] P. Lautenschlager, M. Garriga, S. Logothetidis, and M. Cardona. Interband critical points of GaAs and their temperature dependence. *Physical Review B*, 35(17):9174–9189, June 1987.

[164] M. B. Panish and H. C. Casey Jr. Temperature Dependence of the Energy Gap in GaAs and GaP. *Journal of Applied Physics*, 40(1):163–167, January 1969.

[165] Moïra Hocevar, Le Thuy Thanh Giang, Rudeesun Songmuang, Martien den Hertog, Lucien Besombes, Joël Bleuse, Yann-Michel Niquet, and Nikos T. Pelekanos. Residual strain and piezoelectric effects in passivated GaAs/AlGaAs core-shell nanowires. *Applied Physics Letters*, 102(19):191103, May 2013.

[166] J. Jadczak, P. Plochocka, A. Mitioglu, I. Breslavetz, M. Royo, A. Bertoni, G. Goldoni, T. Smolenski, P. Kossacki, A. Kretinin, Hadas Shtrikman, and D. K. Maude. Unintentional High-Density p-Type Modulation Doping of a GaAs/AlAs Core–Multishell Nanowire. *Nano Letters*, 14(5):2807–2814, May 2014.

[167] M. S. Skolnick, C. W. Tu, and T. D. Harris. High-resolution spectroscopy of defect-bound excitons and acceptors in GaAs grown by molecular-beam epitaxy. *Physical Review B*, 33(12):8468–8474, June 1986.

[168] M. S. Skolnick, D. P. Halliday, and C. W. Tu. Zeeman spectroscopy of the defect-induced bound-exciton lines in GaAs grown by molecular-beam epitaxy. *Physical Review B*, 38(6):4165–4179, August 1988.

[169] Teng Shi, Howard E. Jackson, Leigh M. Smith, Nian Jiang, H. Hoe Tan, and Chennupati Jagadish. Thermal Delocalization of Excitons in GaAs/AlGaAs Quantum Well Tube Nanowires. *Nano Letters*, 16(2):1392–1397, February 2016.

GOZDE TUTUNCUOGLU

PhD Student at École Polytechnique Féderale de Lausanne (EPFL), Switzerland

Address: Rue des Echelettes, 10 1004 Lausanne, Switzerland

Citizenship: Turkish **Date of birth:** 13/12/1987

gozdeetu@gmail.com **Tel: +41762515989** Google Linked in

RESEARCH SKILLS

- General operation and maintenance of ultrahigh vacuum (UHV) equipment including molecular beam epitaxy (MBE) reactor
- MBE growth of i) III-V thin films, ii) III-V nanostructures such as GaAs and InAs nanoscale membranes, Ga-assisted nanowire growth, and related radial and axial heterostructures
- Four years of Class-10 clean room microfabrication experience; e-beam lithography, photolithography, wet and dry etching experience, Reactive Ion Etching (RIE), Plasma Enhanced Chemical Vapor Deposition (PECVD)
- Characterization experience in Scanning Electron Microscopy (SEM), Atomic Force Microscopy (AFM), Transmission Electron Microscopy (TEM) Talos F200S
- Optical Characterization: Photoluminescence (PL), Cathodoluminescence (CL)
- Authored and coauthored 25 publications about the growth and applications of III-V nanostructures.

PROFESSIONAL EXPERIENCE

04/12 – Present — **Doctoral Research Assistant, in EPFL Lausanne, Switzerland**
Optoelectronic Properties of III-V Nanostructures Grown by Molecular Beam Epitaxy (MBE)

- Growth and optical characterization of GaAs & AlGaAs nanostructures.
- Preparation of scientific publications
- Supervising master & bachelor students

08/11 – 02/12 — **Master Research Assistant, in EPFL, Lausanne, Switzerland**
Doping and Characterization of GaAs nanowires with Sulphur monolayer doping

11/10 – 04/11 — **Research Assistant, in EPFL, Switzerland**
Characterization of Self-Assembling Monolayers (SAM) of thiol molecules on Gold (Au) substrates with Scanning Tunneling Microscopy

10/09 – 06/2010 — **Research Assistant, in Sabanci University, Istanbul, Turkey**
Hybrid Photovoltaics : Synthesis of colloidal PbSe & PbS semiconductor nanocrystals and characterization of nanocrystals with UV-Vis spectroscopy and AFM

09/09 — **Research Intern, in Paderborn University, Paderborn, Germany**
Growth mechanism of ZnO nanorods on different substrates

07/09-09/09 — **Research Intern, in Ludwig Maximilians University, Munich, Germany**

Synthesis and inkjet printing of CdSe & CdTe semiconductor nanocrystals with office printers

06/07 – 01/09 **Undergraduate Research Assistant, in Sabanci University, Istanbul, Turkey**
Sol-gel synthesis and XRD analysis of Phosphorescent Strontium Aluminate Powders

TEACHING EXPERIENCE

02/13 - Present **Project Co-supervisor** in EPFL Lausanne, Switzerland
Bachelor and Master Project Co-Supervisor (4 Students)
Master Thesis Co-Supervisor (3 Students)

01/15 – 06/15 **English Teacher** for immigrants in L'Espace Mozaïk d'Appartenances Lausanne, Switzerland (Voluntary)

01/08 - 06/2010 **Coordinator of Moderator Education Program** in Academic Support Program (ASP), Sabanci University, Turkey

10/09 - 06/2010 **Teaching Assistant** of Thermodynamics course in Sabanci University, Istanbul, Turkey

10/06 – 06/08 **Calculus and Natural Sciences 101 & 102 Tutor** in Academic Support Program (ASP), Sabanci University, Istanbul, Turkey

EDUCATION

05/12 – 09/16 Expected **Ph.D., EPFL,** Lausanne, Switzerland - Materials Science and Engineering
Dissertation topic: Optoelectronic Properties of III-V Nanostructures Grown by Molecular Beam Epitaxy (MBE)
Thesis supervisor: Anna Fontcuberta i Morral

09/10 – 02/12 **M.Sc., EPFL**, Lausanne, Switzerland - Materials Science and Engineering
Date of Grad: February 2012

07/09 – 09/09 **International Summer Research Program**, Munich, Germany
Hosted by Nanosystems Initiative Munich (NIM)

2006 – 2010 **B.Sc., Sabancı University**, Istanbul, Turkey
Junior in Faculty of Engineering and Natural Sciences (FENS)
Materials Science and Engineering Minor: Physics
Date of Graduation: June 2010

MAJOR PUBLICATIONS (Full list can be accessed at google scholar page)

- Towards defect-free 1-D GaAs/AlGaAs heterostructures based on GaAs nanomembranes, Nanoscale, Tutuncuoglu G. et al., **7**, 19453-19460, (2015)

- Wetting of Ga on SiOx and its impact on GaAs nanowire growth on silicon, F Matteini, G Tütüncüoglu et al., Crystal Growth & Design, 15 (7), 3105-3109 (2015)

- Bottom-up engineering of InAs at the nanoscale: From V-shaped nanomembranes to nanowires E Russo-Averchi, G Tütüncüoglu et al., Journal of Crystal Growth 420, 47-56 (2015)

- High yield of GaAs nanowire arrays on Si mediated by the pinning and contact angle of Ga, E Russo-Averchi*, J Vukajlovic Plestina*, G Tütüncüoglu* et al., Nano letters 15 (5), 2869-2874 (2015)

- Time-Resolved Nonlinear Coupling between Orthogonal Flexural Modes of a Pristine GaAs Nanowire, D. Cadeddu, F. R. Braakman, G. Tütüncüoglu et al., Nano Lett. (2016) ASAP

- Photonic–Plasmonic Coupling of GaAs Single Nanowires to Optical Nanoantennas, A Casadei, EF Pecora, J Trevino et al., Nano letters 14,5, 2271-2278 (2014)

- III–V nanowire arrays: growth and light interaction, Nanotechnology, M Heiss*, E Russo-Averchi*, A Dalmau-Mallorquí*, G Tütüncüoğlu* et al. 25,1,14015 (2014)

*Equal contribution

PRESENTATIONS

Jun 2016	CIMTEC 2016 Perugia, Italy
	Invited Talk: III-V nanowires, growth challenges and applications in next generation photovoltaics * on behalf of Anna Fontcuberta i Morral
Nov 2015	Sabanci University, Istanbul, Turkey
	Invited Seminar: III-V Nanostructures grown by Molecular Beam Epitaxy (MBE) and Research in the Fontcuberta Research Group at EPFL
Sep 2015	Pulse Summer School – Epitaxy Updates and Promises (Poster and Talk) Porquerolles, France
	Invited Talk: Optical Properties of Nanowires (Raman and PL Spectroscopy) * on behalf of Anna Fontcuberta i Morral
Sep 2015	Nanowire Growth Workshop (NWG2015), Barcelona, Spain (Poster)
	Poster award
Jun 2014	NanoTR-10 Istanbul, Turkey
	Talk: III-V Nanowire-Based Heterostructures Grown with Molecular Beam Epitaxy (MBE)
Aug 2014	Nanowire Growth Workshop (NWG2014), Eindhoven, Netherlands (Poster)
Sep 2014	Molecular Beam Epitaxy Conference (MBE2015), Flagstaff, USA; (Poster)

SCHOOL PARTICIPATIONS

Jul 2016	Lindau Nobel Laureate Meetings Lindau, Germany
Feb 2014	AFM School EMPA, Dubendorf, Switzerland
Sep 2015	Pulse Summer School – Epitaxy Updates and Promises, Porquerolles, France

AWARDS & HONORS

Jul 2016	Selected to be chosen as the participant of Turkey in Lindau Nobel Laureate Meetings Lindau, Germany
Jul 2015	2nd Best Poster Award at the Nanowire Growth Workshop 2015, Barcelona
06/09 - 08/09	Nanosystems Initiative Munich (NIM) - Student Research Award which covers the full tuition fee, the cost for accommodation and excursions as well as for travel and living expenses.
2006 – 2010	Sabanci University-Awarded for Honor Scholarship by annual Central Nationwide University Entrance Exam
2006 – 06/2010	Sabanci University -FENS Dean's Honor and High Honor List for eight terms

OTHER SKILLS AND EXTRA-CURRICULAR ACTIVITIES

Computer Skills: Ms Office, Latex, Matlab, Origin Lab, Python

Languages: Turkish (Native), English (Fluent), French (Pre-intermediate), German (Basic)

Hobbies: Volunteering with immigrants, handicapped children, sci-fi novels, skiing

References are available upon request